

MICROFLUIDIC MIXING AND ITS USE IN LAB-ON-A-CHIP DEVICES

By

ZHENG XIA

A DISSERTATION PRESENTED TO THE GRADUATE SCHOOL
OF THE UNIVERSITY OF FLORIDA IN PARTIAL FULFILLMENT
OF THE REQUIREMENTS FOR THE DEGREE OF
DOCTOR OF PHILOSOPHY

UNIVERSITY OF FLORIDA

2008

© 2008 Zheng Xia

To my parents

To Xinyi and our lovely son Chase

ACKNOWLEDGMENTS

My utmost gratitude goes to my PhD advisor, Dr. Hugh Fan for allowing me to join his lab, for his expertise, guidance, and most of all, for his patience. Without his support and his guidance, I wouldn't perform and finish this dissertation work. I am also greatly indebted to my committee members, Dr. Mark Sheplak, Dr. Renwei Mei, Dr. Lou Cattafesta and Dr. Ranganathan Narayanan for their valuable suggestions on my dissertation.

My thanks and appreciation goes to my former lab colleagues, Dr. Qian Mei for her continuous presence whenever a discussion is needed, Carl Fredrickson for his readiness to help on device fabrication, Dr. Champak Das for his continual encouragement in all these years of my PhD work. I also want to express my gratitude to the fellow graduate students Ruba Khnouf, Karthik Pitchaimani, Jacqueline Viren, Cesar Moreira, Pan Gu, undergraduate students Fernando Tavares, Corey Walker, Andrew Simon, Austin Gispanski, and post-doc colleagues Dr. Alexander Stoyanov, Dr. Jiyou Zhang, Dr. Hong Chen for the wonderful time I spent with them in the lab. Their help made my work much smoother.

And then there are other people who have made Gainesville a very special place over these years. They are Chao Cao, Liqun Xu, Jun Liu, Xiaomin Lu and Heshan Lin, Kun Chen and Zhenzhen Zhang, Mingzhen Bao, Yingyan Lou, Lu Ma, Jianlin Li, Jiejun Zhang, Lezhou Zhan and Anna Leung, Yingling Huang and Wenqiang Tian, Hong Wang, Qi Song, and Yawei Li.

Finally, I would like to thank my parents whose love is boundless, for traveling across the Pacific and be on my side in this most glorious moment of my life. I thank my wife, Xinyi who has stood beside me and encouraged me constantly. My most special thanks go to my newborn baby, Chase for giving me happiness and joy every day and night. To my precious family, I dedicate this dissertation.

TABLE OF CONTENTS

| | <u>page</u> |
|---|-------------|
| ACKNOWLEDGMENTS | 4 |
| LIST OF TABLES | 8 |
| LIST OF FIGURES | 9 |
| LIST OF SYMBOLS | 12 |
| ABSTRACT..... | 14 |
| CHAPTER | |
| 1 INTRODUCTION | 16 |
| 1.1 Lab-on-a-chip and MEMS..... | 16 |
| 1.2 Microfluidics and Electroosmosis | 18 |
| 1.2.1 Electric Double Layer..... | 19 |
| 1.2.2 Electroosmosis..... | 21 |
| 1.3 Microfluidic Mixing | 24 |
| 1.4 Objectives and Study Overview | 28 |
| 2 DEVICE DESIGN AND FABRICATION | 33 |
| 2.1 Ridged Channel | 33 |
| 2.1.1 Design..... | 34 |
| 2.1.2 Photolithography | 35 |
| 2.1.3 Electroplating | 35 |
| 2.1.4 Hot Embossing | 36 |
| 2.1.5 Bonding | 36 |
| 2.2 Wavy Channel | 36 |
| 2.2.1 Design..... | 37 |
| 2.2.2 Soft Lithography..... | 38 |
| 2.2.3 Bonding | 39 |
| 2.3 Micro Mixer..... | 39 |
| 2.3.1 Device Design | 39 |
| 2.3.2 Fabrication of Plastic Substrates | 39 |
| 2.3.3 Electrode Printing..... | 40 |
| 2.4 Characterization of Fabrication Process | 40 |
| 2.4.1 Comparison between Glass Master and E-Form..... | 41 |
| 2.4.2 Comparison between E-Form and Plastic Chip..... | 41 |
| 2.4.3 Comparison of Plastic Chip and Glass Master | 42 |

| | | |
|-------|---|-----|
| 3 | DECONVOLUTION MICROSCOPY FOR FLOW VISUALIZATION | 51 |
| 3.1 | Introduction..... | 51 |
| 3.2 | Theoretical Background..... | 52 |
| 3.2.1 | Optical Sectioning | 53 |
| 3.2.2 | Convolution | 53 |
| 3.2.3 | Deconvolution | 55 |
| 3.3 | Experimental Methodology | 55 |
| 3.3.1 | Experimental Setup | 55 |
| 3.3.2 | Optical Sectioning and Image Reconstruction | 56 |
| 3.4 | Results and Discussion | 56 |
| 3.4.1 | Optical Sectioning | 56 |
| 3.4.2 | Deconvolution | 57 |
| 3.4.3 | Mixing in Ridged Channel | 58 |
| 3.5 | Summary..... | 60 |
| 4 | ELECTROOSMOTIC FLOW IN WAVY CHANNELS | 65 |
| 4.1 | Introduction..... | 65 |
| 4.2 | Governing Equations | 67 |
| 4.3 | Formulation of Solutions | 70 |
| 4.3.1 | Electric Potential | 70 |
| 4.3.2 | Stream Function..... | 72 |
| 4.4 | Results and Discussion | 76 |
| 4.4.1 | Electric Potential | 76 |
| 4.4.2 | Flow Velocity | 77 |
| 4.4.3 | Similarity between Flow Velocity and Electric Field | 79 |
| 4.4.4 | Vorticity in Electroosmotic Flow | 80 |
| 4.4.5 | Electroosmotic Flow with Pressure Gradients | 81 |
| 4.4.6 | Onset of Recirculation..... | 83 |
| 4.4.7 | Recirculation Pattern and Size..... | 86 |
| 4.5 | Summary..... | 87 |
| 5 | PULSED RECIRCULATION MIXER | 101 |
| 5.1 | Introduction..... | 101 |
| 5.2 | Recirculation in Ridged Channels | 102 |
| 5.2.1 | Validation of CFD-ACE+..... | 102 |
| 5.2.2 | Modeling of Ridged Channels..... | 103 |
| 5.2.3 | Poiseuille Flow in Ridged Channels..... | 104 |
| 5.2.4 | Flow Recirculation Intensity | 106 |
| 5.2.5 | Experiment Validation..... | 107 |
| 5.3 | Mixing by Recirculation | 108 |
| 5.3.1 | Formulation of Unsteady EOF | 109 |
| 5.3.2 | Pulsed Recirculation | 110 |
| 5.4 | Simulation of Pulsed Recirculation Mixer | 111 |
| 5.5 | Experiment Validation of Pulsed Recirculation Mixer | 114 |

| | |
|--|-----|
| 5.5.1 Experiment Setup | 114 |
| 5.5.2 Experiment Results and Analysis | 114 |
| 5.6 Summary | 116 |
| 6 CONCLUSIONS AND FUTURE DIRECTIONS | 131 |
| 6.1 Conclusions..... | 131 |
| 6.2 Future Directions | 132 |
| 6.2.1 Deconvolution Algorithm..... | 132 |
| 6.2.2 Optical Sectioning for Periodic Flow | 133 |
| 6.2.3 Optimization of Pulsed Recirculation Mixer..... | 134 |
| 6.2.4 Analytical Solution of EOF in Irregular Channel..... | 134 |
| APPENDIX | |
| A POINT SPREAD FUNCTION | 138 |
| B DECONVOLUTION ALGORITHMS..... | 141 |
| B.1 Inverse Filter | 141 |
| B.2 Constrained Iterative Deconvolution | 141 |
| B.3 Blind Deconvolution | 142 |
| C SOLUTION TO ELECTRIC POTENTIAL AND STREAM FUNCTION..... | 143 |
| C.1 Electric Potential Solution | 143 |
| C.2 Stream Function Solution..... | 143 |
| LIST OF REFERENCES | 147 |
| BIOGRAPHICAL SKETCH | 153 |

LIST OF TABLES

| <u>Table</u> | | <u>page</u> |
|--------------|--|-------------|
| 3-1 | Comparison of deconvolution algorithms..... | 61 |
| 5-1 | Summary of boundary conditions for CFD simulation..... | 118 |

LIST OF FIGURES

| <u>Figure</u> | <u>page</u> |
|---|-------------|
| 1-1 Electric double layer (EDL) and electric potential profile in EDL..... | 30 |
| 1-2 Electroosmotic flow between two parallel infinite glass plates with thin EDL..... | 31 |
| 1-3 Velocity profile of an electroosmotic flow in the region close to the glass surface | 31 |
| 1-4 Schematic of bioluminescence detection in a T-microchannel..... | 32 |
| 2-1 Creation of ridged channels through isotropic etching..... | 43 |
| 2-2 Photomask layout of a T-channel | 43 |
| 2-3 Fabrication process of plastic LOC devices..... | 44 |
| 2-4 Plastic device with 6 channels | 44 |
| 2-5 The 3D ridged channels and 2D simplified form of ridged channels..... | 45 |
| 2-6 Photomask layout of wavy channels..... | 46 |
| 2-7 Wavy channels fabricated on PDMS substrates | 46 |
| 2-8 Photomask layout of a pulsed recirculation mixer..... | 47 |
| 2-9 Layout and microscopic image of electrodes..... | 47 |
| 2-10 Plastic device with a pulsed recirculation mixer..... | 48 |
| 2-11 Glass master, the E-form and a plastic chip used in the work. | 48 |
| 2-12 Histogram of the differences between the ridge heights on the E-form and the channel depths on the glass master | 49 |
| 2-13 Histogram of the differences between the channel depths in the plastic chip and the ridge heights on the E-form | 49 |
| 2-14 Histogram of the differences between the channel depths on the plastic chip and the channel depths on the glass master | 50 |
| 3-1 Optical sectioning process for visualization of a microfluidic flow | 62 |
| 3-2 Three-dimensional view of fluorescein in a channel by stacking raw images acquired by optical sectioning..... | 63 |
| 3-3 Cross-sectional image of a fluorescein flow in ridged channels..... | 63 |

| | | |
|------|--|-----|
| 3-4 | Top view and cross section views of a Poiseuille flow in ridged channels | 64 |
| 4-1 | Two-dimensional wavy channel between a flat plate at the top and a sinusoidal plate at the bottom | 89 |
| 4-2 | Boundary conditions and contour path used in the analytical solution | 89 |
| 4-3 | Effect of the scaled wave amplitude on the electric potential distribution in a wavy channel | 90 |
| 4-4 | Effect of the channel width on the electrical potential distribution in a wavy channel | 91 |
| 4-5 | Effect of the scaled wave amplitude on the velocity field in a wavy channel | 92 |
| 4-6 | Effect of the scaled channel width on the velocity field in a wavy channel | 93 |
| 4-7 | Flow rate as a function of the ratio of wave amplitude to channel width | 94 |
| 4-8 | Similarity between the electric field and the velocity field of an EOF | 94 |
| 4-9 | Combined flow driven by electroosmosis and pressure | 95 |
| 4-10 | Images of microbead flow in a wavy channel in a microfabricated PDMS device | 96 |
| 4-11 | Streamline patterns of fluid flows in wavy channels | 97 |
| 4-12 | Velocity profiles at the neck as a function of K | 98 |
| 4-13 | Flow recirculation diagram for various scaled wave amplitude (α), scaled channel width (h), and the ratio of pressure force to electrokinetic force (K) | 98 |
| 4-14 | Size of recirculation region as a function of K | 99 |
| 4-15 | Size of recirculation region as a function of α and h | 100 |
| 5-1 | Microscopic image of microbead traces in a flow in ridged channels | 119 |
| 5-2 | Plot of streamline and velocity profile of flows in the wavy channel by CFD-ACE+ simulation and the analytical solution | 119 |
| 5-3 | Comparison of electric potential and stream function data in flows in wavy channels by CFD-ACE+ simulation and the analytical solution. | 120 |
| 5-4 | Simulation model used for simulating flows in ridged channel | 120 |
| 5-5 | Simulation of fluid mixing in ridged channels by CFD-ACE+ | 121 |
| 5-6 | Simulated mixing performance of pulsed recirculation mixer | 122 |

| | | |
|------|--|-----|
| 5-7 | Top views of streaklines of massless particles convected by flows in ridged channels.. | 122 |
| 5-8 | Streaklines of massless particles convected by flow in ridged channels at different K ... | 123 |
| 5-9 | Flow patterns in a ridged channel made on plastic substrates | 124 |
| 5-10 | Pulsed electric signal applied in PRM for induction of periodic recirculation..... | 124 |
| 5-11 | Simulation model for pulse recirculation mixer | 125 |
| 5-12 | Temporal variation of Rhodamine-B distribution at a cross section of the periodic recirculation mixer over one period..... | 126 |
| 5-13 | Evolution of the Rhodamine-B concentration variation in the fluid in a PRM | 126 |
| 5-14 | Experiment setup for the fluid mixing of Rhodamine-B solution and DI water in a prototype PRM..... | 127 |
| 5-15 | Comparison between the flow in the inactive mixer and the flow in the active mixer.... | 128 |
| 5-16 | Temporal variation of fluid mixing in PRM during one cycle | 129 |
| 5-17 | Temporal evolution of intensity histogram profile in the ridge channel in one cycle | 129 |
| 5-18 | Effect of parameter K on mixing performance of pulsed recirculation mixer | 130 |
| 6-1 | Roadmap of research work on the development of the pulsed recirculation mixer..... | 136 |
| 6-2 | Microscopic images of fluid flow in periodic channels of different profiles | 137 |
| A-1 | Plot of point spread function in an octant of 3D space..... | 139 |
| A-2 | Airy disk, plot of PFS at the plane of $z = 0$ | 139 |
| A-3 | Plot of PSF on a 2D plane along z axis..... | 140 |

LIST OF SYMBOLS

| | |
|-----------|---|
| A | Wave amplitude of wavy channel |
| c | specimen concentration |
| D | Hydraulic diameter of ridged channel |
| E | Electric field |
| F | Faraday constant |
| h | Scaled channel width, $2\pi H/L$ |
| H | Average Width of wavy channel |
| I | Pixel intensity |
| \Im | Imaginary part of a complex value |
| K | Dimensionless parameter represents ratio of pressure force to electrokinetic body force |
| Kn | Knudson number |
| L | Characteristic length scale of microchannel (wavelength for wavy channel, periodic distance for ridged channel) |
| n | Refractive index of media |
| \hat{n} | Unit vectors normal to microchannel walls |
| NA | Numerical aperture of objective lens |
| p | Pressure |
| P_0 | Characteristic applied pressure |
| Pe | Peclet number |
| R | Universal gas constant |
| \Re | Real part of a complex value |
| Re | Reynolds number |
| St | Strouhal number |
| t | Time |

| | |
|---------------|---|
| \hat{t} | Unit vectors tangential to microchannel walls |
| T | Temperature |
| \bar{V} | Velocity vector |
| z | valence number |
| α | Scaled wave amplitude, $2\pi A/L$ |
| δ | Variance of specimen concentration at a cross section |
| ε | Electric permittivity |
| ζ | Complex variable |
| ζ_{pot} | Zeta potential, electric potential at Stern plane |
| η | Electroosmotic mobility |
| λ_d | Debye length |
| λ | Light wavelength |
| ν | Kinematic viscosity |
| ξ | Complex variables |
| ϕ | Electric potential |
| ρ | Density |
| ρ_e | Electric charge density |
| τ | Characteristic time scale of pulsed electric field |
| Φ_0 | Characteristic applied electric potential |
| ψ | Stream function |
| ω | Vorticity |

Abstract of Dissertation Presented to the Graduate School
of the University of Florida in Partial Fulfillment of the
Requirements for the Degree of Doctor of Philosophy

MICROFLUIDIC MIXING AND ITS USE IN LAB-ON-A-CHIP DEVICES

By

Zheng Xia

August, 2008

Chair: Z. Hugh Fan
Cochair: M. Sheplak
Major: Mechanical Engineering

Because of the difficulty to achieve convective mixing in laminar flows, microfluidic mixers have been developed in this work to rapidly homogenized fluids in lab-on-a-chip devices. To evaluate the efficiency of fluid mixing in a mixer, direct visualization of microflows is needed. Hence a technique of coupling a conventional optical microscope with a computational deconvolution algorithm is explored to produce images of three-dimensional flows in plastic microfluidic channels. The approach, called deconvolution microscopy, is achieved by (1) optically sectioning the flow in the microchannel by collecting a series of fluorescence images at different focal planes along the optical axis, and (2) removing the out-of-focus fluorescence signal by the deconvolution method to reconstruct a corrected three-dimensional concentration image. Different convolution algorithms for a uniform concentration test case are compared, and then deconvolution microscopy is demonstrated in flow visualization in microfluidic channels. Deconvolution microscopy has been demonstrated in evaluating the fluid mixing by the flow twisting in ridged channels. An agreement has been found between the theoretic results and experimental results.

A fluid phenomenon, flow recirculation, is explored for microfluidic mixing in lab-on-a-chip devices. Flow recirculation is induced when electroosmotic flow and Poiseuille flow are present in ridged channels. To understand flow recirculation, electroosmotic flow (EOF), a phenomenon resulting from the interaction of an external electric field and surface free charges in the electric double layer, is studied. The channel geometry variation represented by a wavy channel between a plane wall and a sinusoidal wall is investigated. An analytical solution to the EOF in the wavy channel using complex function theory is presented. Flow recirculation regions are predicted when an adverse pressure gradient is added to an EOF in the wavy channel. The onset condition of flow recirculation and the size of the recirculation region are determined. It is found that they are dependent on dimensionless parameters related to forces and the channel geometry. Experimental results are presented to validate the theoretical prediction and the analytical solution.

After investigating flow twisting and flow recirculation, a novel microfluidic mixer is developed. It consists of a portion of ridged channels and two integrated electrodes. With the application of a pulsed electric field, periodic flow recirculation is induced, and served as the secondary mixing mechanism in the mixer in addition to the flow twisting effect. To facilitate the mixer design, CFD software is employed to simulate the recirculation in the ridged channel and optimize the operation parameters for the mixer. An effective and efficient mixing performance from the proposed mixer is predicted by CFD simulation. Mixing experiments are also carried out on a prototype mixer to validate the mixing performance. The experimental results agree qualitatively with the CFD numerical results.

CHAPTER 1 INTRODUCTION

Inspired by the famous talk on miniaturization by Richard Feynman,¹ scientists and engineers have developed technologies to allow mechanical devices, chemical and biological sensors and actuators to be integrated onto a small-sized platform over the past 50 years.² Lab-on-a-chip (LOC) devices are such a miniaturized system that can perform multiple functions for an analytical operation, such as chemical synthesis, extraction, separation, detection and so on.³ The major objective of this thesis is to characterize micro-scale flow recirculation and explore its use in fluid mixing in a LOC device. Before I present the theory, design, and fabrication of the LOC device, the concept and basic knowledge of microelectromechanical systems (MEMS) and lab-on-a-chip, and microfluidics are provided in this introduction.

1.1 Lab-on-a-chip and MEMS

MEMS are miniaturized integrated systems that combine electrical and mechanical components with at least one of their dimensions in the micrometer scale. The term MEMS (microsystems technology in Europe, or micromachines in Japan) was defined in 1987,⁴ when the integrated fabrication of mechanism on silicon was made possible. Ever since then, it has advanced due to the rapid advancement of the integrated circuit (IC) technology, since MEMS uses the modified IC processing techniques that developed in semiconductor industry.⁵

Originally, MEMS was applied exclusively to silicon-based mechanical applications, which is exemplified by the fact that mechanical applications have dominated the MEMS field in the earlier years. Examples of MEMS device applications include inkjet-printer cartridges, accelerometers, miniature robots, microengines, gyroscopes, micromirrors, fluid pumps, and pressure sensors.⁶ However, as more realized the coming century would be the age of biotechnology and information technology, MEMS has shift its focus towards new applications

either information related or chemical and biological in nature. As a consequence, more specified terms has emerged in the research field, such as BioMEMS, mechanical MEMS, optical MEMS (or MOEMS), radio frequency MEMS (or RF-MEMS). BioMEMS is an equivalent term to LOC, and has been widely used by researchers from engineering world to emphasize the micro-fabrication techniques. While micro total analysis system (MicroTAS or μ TAS), preferred by chemists, is another equivalent term indicating that multiple analytical functional components are integrated onto a single platform to perform a well-defined analysis task. Generally, these terms are interchangeable. In the dissertation, LOC is the term that primarily used.

MEMS inherits from integrated circuit (IC) manufacturing technology. The major techniques used in MEMS fabrication include film growth, doping, lithography, etching, dicing, packaging, wet bulk micro-machining, surface micro-machining, and micro-molding.^{5,6} While the last three are extensions of IC technology tailored to MEMS fabrication, the others are completely compatible to IC fabrication. Some of the MEMS fabrication techniques are demonstrated in the fabrication of the LOC devices, and will be discussed in details in Chapter 2.

Comparing to its macro-scale counterparts, a MEMS device has merits in many aspects due to its small size, such as portability, cost/performance, energy and material consumption, selectivity and sensitivity, redundancy and reproducibility. As to the lab-on-a-chip applications, miniaturization of devices brings additional benefits, including low reagent usage, fast analysis and high throughput.

In the past decade, MEMS has proven its success by the rapid expansion of the market size. It has been regarded as one of the fastest growing technology area by market analysts. According to Databeans, a Nevada-based market research firm, the global market for MEMS

devices and production equipment was worth an estimated \$5 billion in 2005, \$6.3 billion in 2006, and will be doubled in next five years with an average annual growth rate of more than 20%.⁷ Among all the commercial products, life science applications make majority part of the 2006 MEMS market, and is expected to continue the domination in 2010.⁸ Examples of commercial utilization in current market are Nanogen's NanoChip molecular biology workstation,⁹ Caliper's microfluidic LabChip systems,¹⁰ and Bio-Rad's Experion Automated Electrophoresis System.¹¹

1.2 Microfluidics and Electroosmosis

Microfluidics refers to principles and methods for controlling and manipulating a small volume of liquids through manifolds of channels with dimensions less than a millimeter.^{2, 12, 13} As microfluidics presents itself as a promising technology in the development of MEMS, it has emerged into a fast-growing field that has received intensive attentions from engineers and scientists. Microfluidics has several unique aspects that distinguish it from traditional fluid mechanics, as follows.

- In microfluidic flow, the hydraulic diameter of flow ranges from 0.1 micron to 100 micron. As a direct result, the Reynolds number is small, indicating the viscous force is dominant, and laminar flow occurs as it is way smaller than critical Reynolds number for turbulence flow.
- The continuum assumption still holds as indicated by the low Knudsen number in microfluidic flow. The Knudsen number is defined as $Kn = \lambda/L$, where λ is the mean free path of the fluid molecules and L is the characteristic channel dimension. In liquid, the mean free path is approximated by the lattice space of the molecules.¹⁴ The resulting Knudsen number for microfluidic flow is small, well within the range of continuum flow assumption. For example, the lattice spacing for water is on the order of 0.1 nm, and the corresponding Knudsen number for a microfluidic flow ranges from 10^{-3} to 10^{-6} .
- Electrokinetic effects at the interface between liquids and solids become significant because of the large surface-to-volume ratio in microfluidic flows. Electric double layer (EDL) is induced in a very thin layer of fluid adjacent to solid surface, and the ions in EDL can move at the presence of an external electric field. As a result, an electroosmotic flow (EOF) forms in the fluid, and this phenomenon was first described by F. F. Reuss in his

publication in the Proceedings of the Imperial Society and Naturalists of Moscow in 1809.¹⁴ In the later part of this chapter, I will discuss in details the EDL and the EOF in microfluidic systems.

- Because of its small volume, the internal heating from viscous dissipation becomes significant in the microfluidic flow when a large pressure drop applied. As a result, the fluid density and other properties may vary with the temperature, leading the flow to unexpected effects.
- In microfluidic flows, surface tension at the interface of liquid-solid and liquid-gas becomes one of the dominant forces. Due to the large surface-to-volume ratio, it may exceed body forces such as gravity and electrostatic fields in some applications.

Among all the effects mentioned above, the electrokinetic effects and the resulting EOF have received the most attention from researchers in the development of lab-on-a-chip devices. Since the interaction of liquids and solids at the interface forms the basis of the electroosmosis phenomenon, I first discuss electric double layer theory based on Gouy-Chapman-Stern model.¹⁴

1.2.1 Electric Double Layer

When an aqueous fluid is brought in contact with channel wall surface, the wall acquires surface charges due to ion adsorption, or ion dissolution, or a combination of the two ionization mechanisms.¹⁴ In case that a LOC device is made on surface of glass or silica, the deprotonation (ion dissolution) of surface silanol groups (SiOH) determine the charge on the surface. The pH-dependent equilibrium for the ionization process is represented as



Consequently, an electric double layer is formed close to the channel walls, consisting of two layers (Figure 1-1). Next to the wall is Stern layer, in which ions of opposite charge to that of the solid surface (called counterions, \oplus in the diagram) are tightly attracted to the channel surface. Beyond the Stern layer is diffuse layer, in which ions of like charge (called coions, \ominus in the diagram) are repelled from the wall. Stern plane is defined as the separating plane between the Stern layer and the diffuse layer. In the diffuse layer, the ions are distributed in a diffusive

manner, as the electro-migration of the ions (toward/away from the wall) is dynamically balanced by the thermal motions in the diffuse layer. The concentration of ions in the diffuse layer follows the Maxwell-Boltzmann distribution

$$c_{\pm} = c_0 \exp\left(\frac{\mp zF\phi_{surf}}{RT}\right), \quad (1-1)$$

where ϕ_{surf} is the electric potential in the EDL induced by the surface charge, c_0 is the concentration far from the surface where ϕ_{surf} approaches zero, F is the Faraday constant, R is the gas constant, T is the temperature of the fluid, and z is the valence number of the ions¹⁵. For a solution with a symmetric electrolyte, the charge density becomes

$$\rho_e = -2Fzc_0 \sinh\left(\frac{zF\phi_{surf}}{RT}\right) \quad (1-2)$$

Coupling Equation 1-2 with the Poisson's equation

$$\nabla^2 \phi_{surf} = -\frac{\rho_e}{\varepsilon} \quad (1-3)$$

where ε is the permittivity of fluid, it yields

$$\nabla^2 \phi_{surf} = \frac{2Fzc_0}{\varepsilon} \sinh\left(\frac{zF\phi_{surf}}{RT}\right) \quad (1-4)$$

The above equation can be simplified from Debye-Hückel approximation,¹⁶ which considers that the potential energy of the ions is small in comparison to their thermal energy in the EDL. As a result, the hyperbolic sine term is approximated by the first perturbation only,

$$\nabla^2 \phi_{surf} = \frac{2Fzc_0}{\varepsilon} \frac{zF\phi_{surf}}{RT} \quad (1-5)$$

Hence, the resulting expressions for electric potential and charge density are

$$\phi_{surf} = \zeta_{pot} \exp\left(-\frac{y-y_w}{\lambda_d}\right) \quad (1-6)$$

and

$$\rho_e = \frac{\zeta_{pot}}{\lambda_d^2} \exp\left(-\frac{y-y_w}{\lambda_d}\right), \quad (1-7)$$

where y is the coordinate normal to the wall, y_w is the coordinate of the Stern plane, ζ_{pot} is the electric potential at the Stern plane, and $\lambda_d = \sqrt{\frac{\epsilon RT}{2F^2 z^2 c_0}}$, referred as Debye length, typically is a very small constant. According to Probst, it's about 1nm for a concentration of 10^2 mol/m³ and 10 nm for a concentration of 1 mol/m³ solution.¹⁴

From Figure 1-1, it's evidential that the electric potential drops exponentially to zero towards the center of the fluid. At the edge of the diffuse layer, which is approximately several Debye lengths from the wall, the potential is close to zero. For instance, at the distance of $5\lambda_d$, the electric potential is already less than 1% of the zeta potential, ζ . The charge density also drops exponentially from the surface. Hence the bulk fluid, out of EDL, is assumed neutrally charged.

1.2.2 Electroosmosis

If an electric field is applied in the tangential direction along the solid surface, the ions in the diffuse layer will move under Lorentz body force and carry surrounding solvent with them, thus causing the entire fluid into motion. Such movement of liquid by an applied electric field relative to stationary charged surface is called electroosmosis.

To understand the electroosmotic flow properties (velocity magnitude and profile), a simple EOF confined in a channel between two infinite glass plates is considered. An electric field is imposed via electrodes at the ends of the channel. The electric double layer formed at the surface of the glass plates is assumed thin, such that the Debye length is much smaller in comparison to the channel width (the gap of the two plates).

As shown in Figure 1-2, a local Cartesian coordinate system is set up with the origin on the surface (stern plane actually, in order to simplify the exponential index in electric potential in Equation 1-6), the first axis x tangential to the wall surface, and the second axis y normal to the wall surface.

The set of governing equations for a steady, low Reynolds number EOF is given by

$$-\frac{1}{\rho} \frac{D\rho}{Dt} = 0, \quad (1-8)$$

$$-\frac{\nabla p}{\rho} + \nu \nabla^2 \vec{V} - \frac{\rho_e}{\rho} \nabla \phi = 0, \quad (1-9)$$

and

$$\nabla^2 \phi = -\frac{\rho_e}{\epsilon}, \quad (1-10)$$

where ρ is fluid density, ν is kinematic viscosity, and ϕ is electric potential of the fluid.

The overall electric potential inside the channel is a superposition of ϕ_{surf} , the electric potential associated with the surface charge, and ϕ_{ext} that caused by the external electric field

$$\phi = \phi_{surf} + \phi_{ext} \quad (1-11)$$

Since the external electric field will cause no local accumulation of electric charge, the

Laplacian of ϕ_{ext} drops to zero,

$$\nabla^2 \phi_{ext} = \frac{F}{\epsilon} \sum_i z_i c_i \approx 0 \quad (1-12)$$

ϕ_{surf} is assumed invariant along the glass plates, it is independent of x coordinate, hence

$\frac{\partial \phi_{surf}}{\partial x} = 0$. Thus, the Laplacian of ϕ_{surf} reduces to

$$\nabla^2 \phi_{surf} = \left(\frac{\partial^2}{\partial x^2} + \frac{\partial^2}{\partial y^2} \right) \phi_{surf} = \frac{\partial^2 \phi_{surf}}{\partial y^2} \quad (1-13)$$

Plug Equation 1-11 into Equation 1-10, and make use of Equations 1-12 and 1-13. The

Poisson's equation is reduced to

$$\rho_e = -\varepsilon \frac{\partial^2 \phi_{surf}}{\partial y^2} \quad (1-14)$$

Substitute the charge density term in Equation 1-9 with Equation 1-14. The momentum

equation in x direction yields

$$\frac{\partial^2 u}{\partial y^2} = \frac{1}{\rho\nu} \frac{dp}{dx} + \frac{\varepsilon}{\rho\nu} E_x \frac{\partial^2 \phi_{surf}}{\partial y^2} \quad (1-15)$$

where $E_x = -\nabla \phi_{ext} \cdot \hat{x}$, is a constant in a uniform electric field along the channel surface.

To solve Equation 1-15, the following boundary conditions are applied:

- The electric potential is known at the Stern plane

$$\phi_{surf} \Big|_{y=0,h} = \zeta_{pot} \quad (1-16)$$

- The geometric symmetry of flow field implies that the velocity gradient is zero at the centerline of the channel, i.e.,

$$\frac{\partial u}{\partial y} \Big|_{y=h/2} = 0 \quad (1-17)$$

- The flow is non-slipping at the stern layer, namely,

$$u \Big|_{y=0,h} = 0 \quad (1-18)$$

Integrate twice on the both sides of Equation 1-15, and make use of Equations 1-16 to 1-

18. The velocity is solved as

$$u(y) = \frac{1}{4\rho\nu} \cdot \frac{dp}{dx} \left[\left(\frac{h}{2}\right)^2 - \left(y - \frac{h}{2}\right)^2 \right] + \frac{\varepsilon}{\rho\nu} E_x (\phi_{surf} - \zeta) \quad (1-19)$$

Recall the expression of ϕ_{surf} in Equation 1-6, the result above can be rewritten as

$$u(y) = \frac{1}{4\rho\nu} \cdot \frac{dp}{dx} \left[\left(\frac{h}{2}\right)^2 - \left(y - \frac{h}{2}\right)^2 \right] + \frac{\varepsilon \zeta_{pot}}{\rho\nu} E_x (e^{-y/\lambda_d} - 1) \quad (1-20)$$

The resulting flow, as expressed in Equation 1-20, is the combination of a pressure driven flow and an EOF. The first term in Equation 1-20 represents the flow in the channel due to the presence of pressure drop, while the second term stands for the electroosmosis. By introducing an electroosmotic mobility term

$$\eta = -\frac{\varepsilon\zeta_{pot}}{\rho\nu}, \quad (1-21)$$

the expression for the electroosmosis component can be simplified as

$$u_{eo}(y) = \eta E_x (1 - e^{-y/\lambda_d}). \quad (1-22)$$

The velocity profile of an EOF ($dp/dx = 0$ in Equation 1-20) in the channel with an constant cross sectional area is thus a plug shape, as plotted in Figure 1-2. The EOF velocity near the channel wall is amplified and plotted in Figure 1-3. At the surface, the velocity is zero because of the non-slipping boundary condition. Towards the centerline of the channel, the flow velocity approximates asymptotically to a constant value (ηE), which is determined by the electric field, the fluid viscosity, the fluid dielectric permittivity, and the channel surface zeta potential. The velocity increases dramatically in the vicinity of the channel surface such that in the distance of several Debye length ($\sim 5\lambda_d$), the velocity already reaches within 99% of the asymptotic value. Consider a typical case that the channel width h is 3 orders of magnitude larger than the EDL thickness, the flow is approximately regarded as a plug flow moving at a constant velocity, $u = \eta E$. The EOF in a channel of varying cross sectional area, however, does not resemble a plug flow any more. The velocity profile, as will be discussed in Chapter 4, depends on the variation as well as the channel width.

1.3 Microfluidic Mixing

In general, a lab-on-a-chip device integrates multiple components capable of various analytical functions: mixing, extraction, separation and detection. A mixer, as demonstrated in the example below, is one of the most crucial components. Because of the difficulty in achieving convective mixing in laminar flows at low Reynolds numbers, LOC devices for application of chemical reactions or biological assays often require a mixer to rapidly homogenize solutions of

reagents. This need has long been recognized, and a considerable amount of literature has been devoted on micro mixer design for LOC devices.¹⁷⁻³⁵

Consider an example of a LOC device for protein expression. The device consists of an in vitro transcription and translation (IVT) system in which proteins are synthesized through two steps: a DNA template is transcribed into messenger RNA through RNA polymerase process with an appropriate promoter; the resulting RNA is thereafter translated into proteins with ribosomes and additional necessary components. To detect the protein expression yield, the product of the IVT has to be mixed with reagents and their reaction product is subsequently measured. For example, luciferase is a protein that can be produced by the IVT. The production of luciferase may be detected through its luminescent reaction with luciferin, adenosine triphosphate (ATP), molecular oxygen and Mg^{2+} .³⁶ IVT system product (with luciferase) is brought in contact with the reagent solution (with luciferin, ATP, Oxygen and Mg^{2+}) at the joint of a T-channel as shown in Figure 1-4. The reaction takes place at the interface of the two streams as they are driven toward the other end of T-channel. The product of reaction, bioluminescence emission, can be detected by an external detection system (a CCD camera or a photomultiplier tube). Thus, a thorough and rapid mixing is required to ensure all luciferase involved in the reaction simultaneously.

Mixing, however, is hard to achieve in a LOC device, especially for solutions of large molecules with low molecular diffusivity. As pointed out previously, a fluid flow in microchannels of LOC is often laminar, leaving the possibility for mixing to the molecular diffusion only. It takes considerable amount of time to achieve an effective mixing by the molecular diffusion. Take the luciferase detection as an example. Assume the segregated flows of luciferase and luciferin solution are pumped with a mean velocity $U \sim 1$ cm/s. The T-channel

has a typical width of $h \sim 100 \mu\text{m}$; the typical kinematic viscosity of fluid is $\nu \sim 10^{-5} \text{ cm}^2/\text{s}$. The resulting Reynolds number is thus $Uh/\nu \sim 1$ and the flow dominated by viscous force. The molecular diffusivity of proteins is very low with the typical value of $10^{-7} \text{ cm}^2/\text{s}$. The corresponding Peclet number of the flow ($Pe=Uh/D$), which is the ratio of molecular convection time to molecular diffusion time, turns out to be on the order of 10^5 , implying that the convection of the proteins is much faster than the molecular diffusion. The typical time for molecules diffusing half of the width of the channel, h^2/D , can be as long as 1000 seconds.

A microfluidic mixer is thus in demand to enhance fluid mixing in LOC devices. A principle of mixing two segregated streams is to increase interfacial area and at the same time reduce diffusion distance. The key to achieve effective mixing in a laminar flow is thus to induce transverse motion, namely by stretching and folding fluid flow at cross section of the channel. The past decade has seen a booming number of reports in scientific literatures describing new approaches following this strategy. In general, these approaches can be categorized into two strategies. One is passive mixing technique, in which the transverse motion is induced as a sole result of channel geometry. The other is active mixing technique, in which the transverse motions result from interaction of an additional force with driving force (pressure force for Poiseuille flow or electrokinetic force for electroosmotic flow).

In general, passive mixers are always preferable, as they require no additional forces. Sophisticated design and complicated fabrication, however, are always demanded to achieve effective and efficient mixing in the passive mixers. Various mixing designs have been reported by many research groups. Rohr fabricated a monolithic mixer by polymerizing porous monolithic polymers in the microchannels, and used it to mix aqueous solutions of two fluorescent dyes.²⁵ Burghelea added a small amount of flexible polymers to working liquids,

thus to induce chaos and achieved efficient mixing in microchannels.²⁶ Flow split-and-recombine was applied in Shonfeld's design of micro mixer to shuffle fluid flows, and resulted in a high mixing efficiency.²⁸ Chung et al. presented a simple yet effective mixing chamber to allow fluids self-circulate for mixing enhancement²⁹ Spiral 2D and 3D microchannels were fabricated to utilize the transverse dean flows resulting from centrifugal effects to enhance mixing.^{27,33} Thorough mixing may also be obtained by creating non-uniformity on channel surface.^{34,35} One noticeable design, reported by Whiteside's group, is to create an additional herringbone structures at the bottom of channel to achieve chaotic mixing.¹⁹ In general, for passive micro mixers, extra features have to be added to regular channel geometries, therefore the design is complex and the fabrication processes are stringent. Passive mixers, as an extra component to microfluidic systems, results in flow rate reduction in original flow. For example, the addition of herringbone structures at channel floors causes more pressure drop over the microchannel as fluids are pumped through, hence more pressure head is required to maintain same flow rate when a passive mixer is installed.

Active mixers use various forces, such as mechanical force, Lorentz force, magnetic force, centrifugal force, and acoustic force, to interact with driving force of a fluid flow, and therefore induce transverse flows at cross sections of microchannels. As a result, additional energy is consumed in active mixer other than driving fluid in microfluidic system. Magnetic force was exploited by Suzuki et al. to facilitate mixing.³² They embedded magnetic beads in microchannels and applied appropriate temporal variations of magnetic field to stir the fluids. Bau et al. developed a magneto-hydrodynamic stirrer in which a flow was stirred by Lorentz force induced by the coupling of alternating electric field and a static magnetic field.³¹ Electro-hydrodynamic force as a result of an electric field, was used by Moctar et al. to produce

transversal secondary flow and thus enhance mixing.³⁰ Ultrasonic waves from piezoelectric transducers were used by Yaralioglu et al. to generate acoustic stirring of the fluid perpendicular to the flow direction in a microchannel.²³ A simple active mixing approach by alternatively electroosmotically pumping fluids has been reported by various groups.^{18, 29} Grumann et al. proposed a novel fluidic concept to drastically accelerate mixing process in batch-mode using centrifugal forces.²¹ In general, active mixers usually yield a better mixing result, in comparison to the passive microfluidic mixers. However, the design, fabrication and the control of the additional forces are always more challenging.

1.4 Objectives and Study Overview

The major objective of this research is to study and develop a novel microfluidic mixer based on the phenomenon that fluid flow circulates in a three dimensional (3D) channel driven by pressure force and electrokinetic force. To evaluate the efficiency of microfluidic mixers, I also develop deconvolution microscopy for visualizing flows in microchannels and an analytical method to study flow recirculation in wavy channels. The remaining part of this proposal is organized as follows.

In Chapter 2, the design and fabrication process of LOC devices are presented. The construction of a 3D ridge structure in microchannels is explained. A microfluidic testing device is fabricated on a plastic plate using hot embossing method. A two dimensional (2D) wavy channel is fabricated on poly-dimethylsiloxane (PDMS) substrate for studying the mechanism and property of flow recirculation. Finally, a micro mixer utilizing the recirculation is manufactured on plastic substrate. The characterization of hot embossing process is also reported.

Chapter 3 describes deconvolution microscopy, an equivalent yet less expensive alternative to confocal microscopy, in evaluation of fluid mixing. The theory is discussed. An investigation

of mixing in a Poiseuille flow in ridged channels is carried out to illustrate the use of the deconvolution microscopy.

An analytical solution to EOF with finite pressure in 2D wavy channels is developed in Chapter 4. The method is used in exploring recirculation in a wavy channel, which is expected to help understanding recirculation in a 3D ridged channel. The effects of channel geometry on the electric field, streamline pattern, and flow rate are studied. The similarity between the electric field and the EOF velocity is also discussed. With a parametric study of recirculation in wavy channel, the onset conditions and the characteristic of flow recirculation in the wavy channels are investigated.

Chapter 5 includes results of a numerical study of recirculation in ridged channel using CFD simulation. A micro mixer, called pulsed recirculation mixer, is designed based on the study of flow recirculation in the ridged channel. Periodic recirculation is induced in the mixer to enhance fluid mixing. Experiments are carried out in a prototype mixer fabricated following the procedure in Chapter 2. The experiment results agree well with theoretical predictions by CFD simulations.

The conclusions are drawn and the future directions are discussed in Chapter 6.

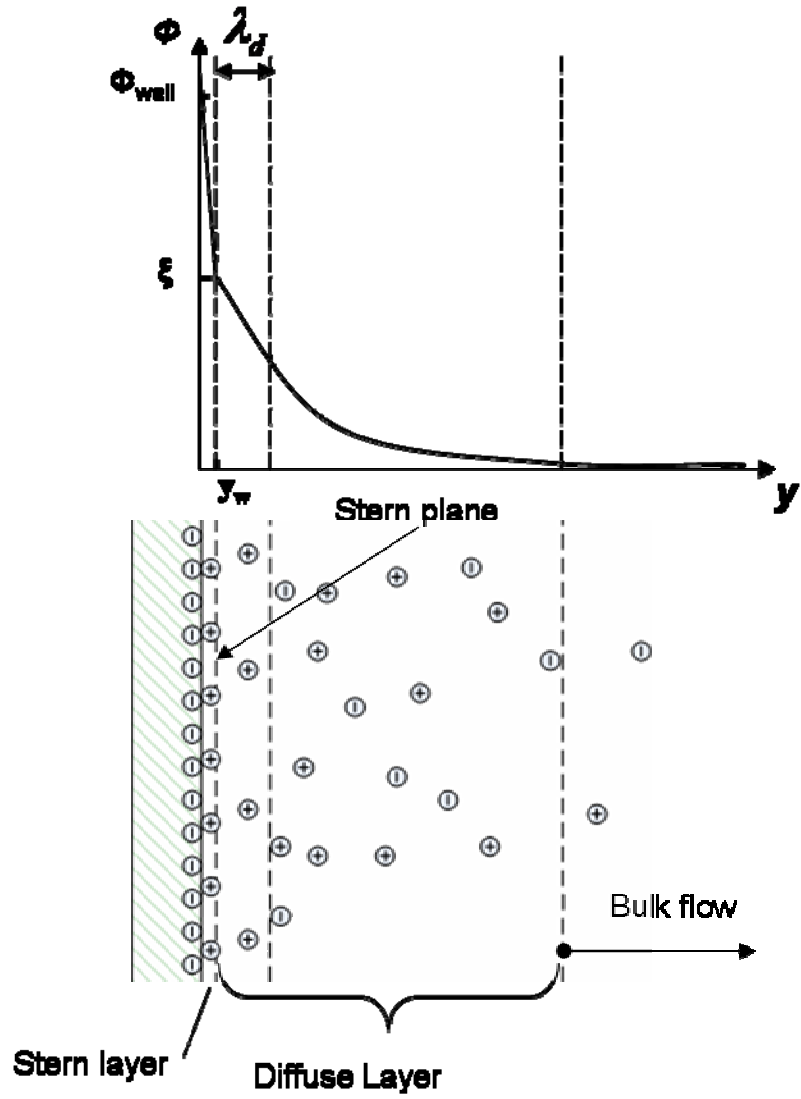


Figure 1-1. Electric double layer (EDL) and electric potential profile in EDL. The electric double layer locates next to the wall surface, and consists of Stern layer and diffuse layer.

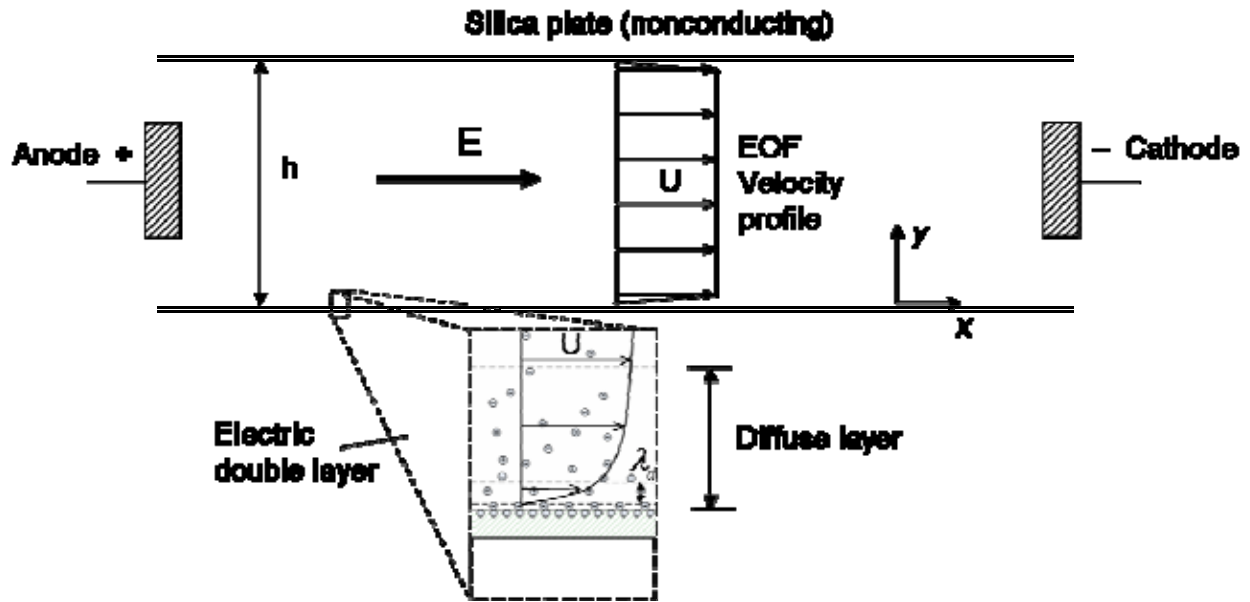


Figure 1-2. Electroosmotic flow between two parallel infinite glass plates with thin EDL. The velocity profile in bulk flow is uniform, while in the diffuse layer it is an exponential curve.

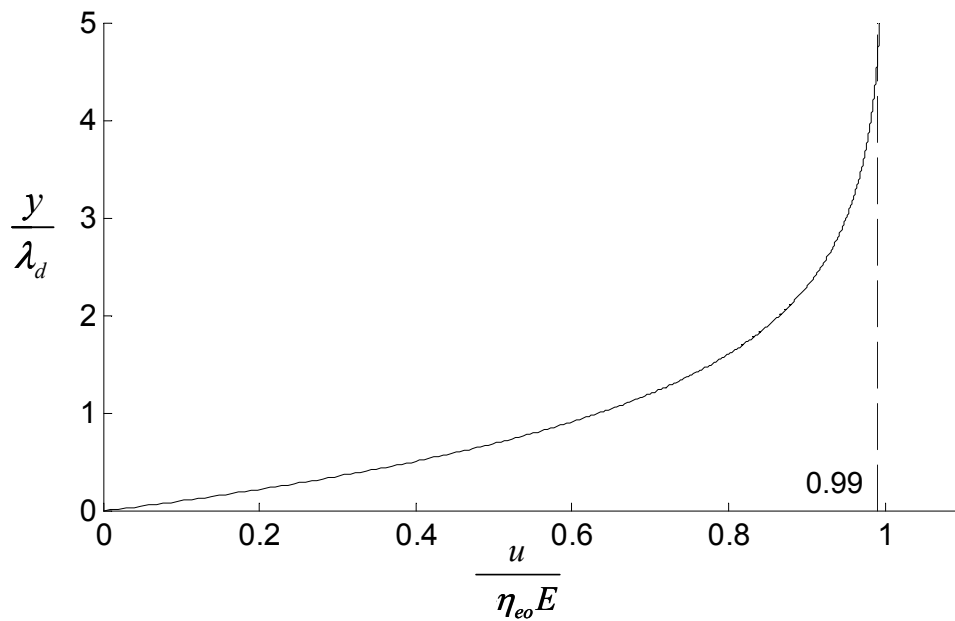


Figure 1-3. Velocity profile of an electroosmotic flow in the region close to the glass surface.

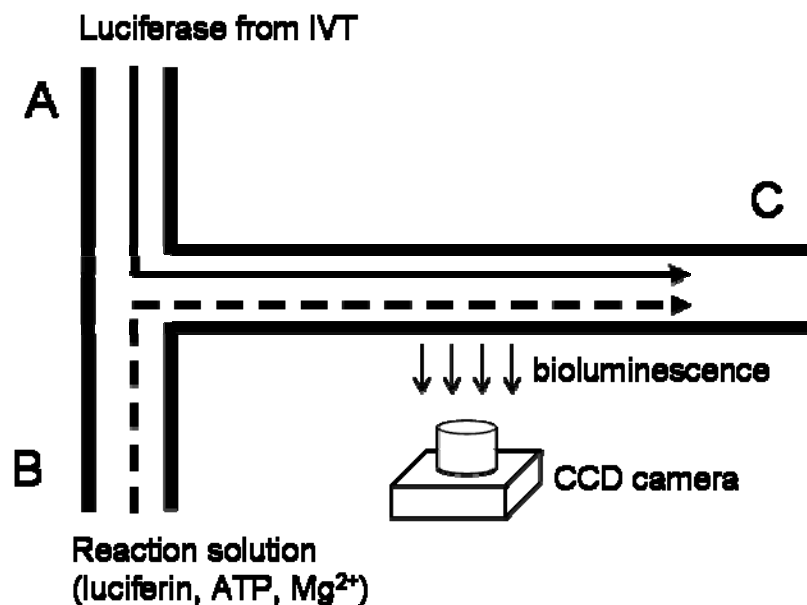


Figure 1-4. Schematic of bioluminescence detection in a T-microchannel. Luciferase solution from IVT is pumped into T-channel from inlet A, while reaction solution, including luciferin, ATP, Oxygen, and Mg²⁺, is pumped from inlet B. Bioluminescent reaction takes place at the interface of the two streams as they flow toward outlet C.

CHAPTER 2 DEVICE DESIGN AND FABRICATION*

This chapter describes the design and fabrication process of three LOC devices that are used in the dissertation work. The first device is made from plastics and consists of a ridged channel, which is used in studying fluid mixing in ridged channel and validating deconvolution microscopy for microfluidic visualization. The device is also used in studying the flow recirculation, a phenomenon observed in ridged channels when a pressure drop and an electric field are imposed. The second device is made from PDMS and consists of a wavy channel, which is essentially a simplified form (2D version) of the ridged channel. The third device, a micro mixer is developed utilizing the flow recirculation phenomenon. The mixer incorporates a portion of ridged channel and a pair of screen-printed electrodes. The characterization of the fabrication process is reported at the end of this chapter.

2.1 Ridged Channel

The ridge structures in the ridged channel are designed to mimic the herringbone structures¹⁹ or slanted wells³⁷ described in the literature. The formation of herringbone structures requires an anisotropic etching in a silicon wafer and then transferred into a PDMS device, but is difficult to achieve in a glass plate on which the anisotropic etching is difficult. In addition, the creation of two channel depths (one for the channel and one for herringbone structures) requires a multiple photolithographic process with two photomasks and a stringent optical alignment. Slanted wells are produced by using an additional step—laser ablation—after microfabrication of microchannels in a plastic device.²⁰

* Part of this chapter has been published in “Deconvolution Microscopy for Flow Visualization in Microchannels”, *Analytical Chemistry*, 2007, **79**(6): p. 2576-2582; and in “Effects of Fabrication Process Parameters on the Properties of Cyclic Olefin Copolymer Microfluidic Devices”, *Journal of MicroElectroMechanical Systems*, 2006, **15**(5): p. 1060–1068.

Ridged channels are fabricated on plastic substrates, from a metal mold, which is created from a glass plate. In comparison to the counterparts, the ridges, as a result of one-step operation, takes less effort in the fabrication. This section describes the ridge formation from isotropic etching, the design of the ridged channels, and the fabrication processes including photolithography, electroplating, hot embossing, and bonding. The plastic device with ridged channels is used in study of flow twisting and deconvolution microscopy reported in Chapter 3, as well as the study of flow recirculation presented in Chapter 5.

2.1.1 Design

It is well known that chemical wet etching in a glass plate results in an isotropic removal. As illustrated in Figure 2-1a, isotropic etching goes laterally under the mask (called undercutting) while it engraves downwards, as indicated by the arrows. Therefore, the cross section of the channel is in the shape of “D”, after the mask is removed and the bottom plate is sealed with another plate. A scanning electron micrograph (SEM) of such a channel is shown in Figure 2-1c. However, a ridge structure can be created when two features are designed close enough with an appropriate etching depth, as shown in Figure 2-1b. The ridges can be obtained by using a judicious design such as different shapes and angles as illustrated in Figure 2-1d.

A T-channel is thus designed to illustrate the feasibility and to study flow properties in such ridged channels. The photomask of the T-channel is drawn in AutoCAD (Autodesk, San Rafael, CA). As schematically shown in Figure 2-2, the layout is composed of a series of identical parallelograms that repeats at a distance of $l = 108\mu\text{m}$ between M and N. Lines from well 1 to M, well 2 to M, and well 3 to N are continuous lines of $30\mu\text{m}$ in width.

Drawing is then sent to Photo Sciences, a photomask manufacturer in Torrance, CA. to generate a 4-inch square dark-field chromium photomask.

2.1.2 Photolithography

The pattern on the photomask is then reproduced in a glass plate via photolithography using microfabrication equipments at the University of Florida Nano-Fabrication facility. A 4-inch square, 0.2-inch thick soda-lime glass plate, pre-coated with a chromium layer ($0.12\mu\text{m}$) and a photoresist layer ($0.2\mu\text{m}$ Shipley 1800), is purchased from Telic Company (Valencia, CA), and used in wet-etching for a glass master.

The fabrication procedure is described as follows and illustrated in Figure 2-3.

1. The glass plate aligned with the photomask (Figure 2-3a,b), is exposed to UV light (365 nm) for 30 seconds at an approximate intensity of 10 mW/cm^2 , using a Karl-Suss MA6 mask aligner (SUSS MicroTec, Germany).
2. The glass plate is then rinsed in photoresist developer (AZ 312MIF, Clariant Corporation, Somerville, NJ) for 40 seconds to removed the exposed photoresist.
3. The glass plate is transferred to a container with chromium etchant (1020, Transene, Danvers, MA) for 30 seconds to etch away the unprotected chromium.
4. A glass etching is subsequently carried out by immersing the glass plate in a glass etchant solution ($\text{HF}/\text{HNO}_3/\text{H}_2\text{O}$ mixture with volume ratio of 20:14:66) for 12 minutes. As a result of isotropic etching described above, ridged channels are created on the glass substrate (Figure 2-3c).
5. The remaining photoresist and chromium on the glass plate are removed in acetone and chromium etchant (Figure 2-3d).

2.1.3 Electroplating

The glass plate, with ridged channels created on the surface, serves as the master piece in electroplating. It is cleaned and then shipped to Optical Electro Forming (Clearwater, FL) to generate a nickel electroforming mold. The glass plate is first coated with a conductive seeding layer, and then connected to the positive pole of a power supply, while the negative pole is attached to a nickel source. Both are placed in a solution of nickel salt. As the electrical current flows through the circuit, nickel ions in the solution lose their charge and settle on the glass plate, while at the other pole the nickel source slowly dissolves and replenishes the ions in the

solution. This process is called electroplating, and the net result of electroplating is that the nickel is continuously transferred from the source and adherently deposited onto the glass plate surface. Note that the electroplating is a slow process in general. It takes a day to deposit a 2-mm thick nickel plate (E-form) that sturdy enough for molding.

After being taken off the glass master, the E-form possesses a negative image of the desired pattern (Figure 2-3e). However, there is a notable discrepancy between the resulting E-form and the glass plate. The cause and the characterization of the difference are discussed in the last part of this chapter.

2.1.4 Hot Embossing

As shown in Figure 2-3f, E-form is employed to produce plastic parts from cyclic olefin copolymer (COC) resins (Ticona Topas® 8007, Florence, KY) using a hydraulic press (Carver, Wabash, IN). Each plastic part is trimmed into a 1" x 3" substrate using a CNC milling machine (Flashcut CNC, San Carlos, CA), which is also used to drilled holes (2 mm diameter) at the ends of channels. The resulting plastic part is schematically drawn in Figures 2-3g, and 2-3h.

2.1.5 Bonding

The channels in the plastic substrate are sealed with 0.1-mm thick film (Topas® 8007) using a thermal laminator (Catena 35, GBC, Northbrook, IL), while the holes become wells as a result. Figure 2-4 shows a picture of the finished plastic device. The thickness of the device is 1.5 mm. Channels are 40 μm deep and 110 μm wide, except where specified otherwise. The height of ridge is 12 μm . The dimensions of channels are measured using a Dektak II surface profiler (Veeco USA, Woodbury, NY) before lamination.

2.2 Wavy Channel

In the study of the flow in ridged channels, a major objective is to understand the mechanism and the properties of flow recirculation. However, the complexity of the ridged

channel, a 3D geometry resulting from isotropic etching as discussed previously, makes it difficult to characterize the location, size, and intensity of recirculation. Although the deconvolution microscopy can be used to visualize flow in such ridged channel as demonstrated in Chapter 3, it is limited to measure the scalar properties in the flow, such as the fluorescence intensity. Particle image velocimetry (PIV)^{38, 39} is thus used for characterizing flow recirculation.

The ridged channel must be simplified to a 2D channel in order to use PIV because of its limited capability in measuring the velocity component along the camera axis. As a result, the width of a ridged channel is made much larger than the depth, as shown in Figure 2-5a, so that the geometric effect from side walls then becomes negligible at the center. This channel is then rotated by 90°; the channel width thus becomes along the optical axis direction. The resulting 2D ridged channel is illustrated in Figure 2-5b (stereo view and top view). The ridges on the bottom of the ridged channel are transferred to the side wall of the 2D ridged channel.

A wavy channel is similar to the 2D ridged channel, and shown in Figure 2-7, except the ridge features on the side wall are replaced by sinusoidal waves. The 2D ridged channel and the wavy channels are fabricated on a PDMS substrate by soft lithography.^{40, 41} Experiments in the wavy channel are carried out and results are presented in Chapter 4.

2.2.1 Design

The photomask layout for the wavy channels is drawn using AutoCAD, and the schematic is shown in Figure 2-6. 40 μm wide continuous lines connect wells 1, 2, and 3 to M, wells 4 and 5 to N. Between M and N are the patterns for a 2D ridged channel (Figure 2-6a), a wavy channel (Figure 2-6b), and three other types of channels. Drawing of the photomask is sent to Photo Sciences to generate a 4-inch square dark-field chromium photomask.

2.2.2 Soft Lithography

The pattern on the photomask is constructed on the surface of a silicon wafer using conventional photolithography techniques. By casting PDMS onto the silicon wafer the pattern is inversely reproduced on the PDMS. Closed channels are obtained by sealing the PDMS piece with another blank PDMS piece. This fabrication process is called soft lithography.⁴⁰ The detailed processing steps are provided below.

1. A silicon wafer is cleaned by rinsing in trichloroethylene (TCE), acetone, and deionized water in sequence.
2. After dehydrated in a vacuum oven at 200°C for 5 minutes, the wafer is primed with hexamethyldisilazane (HMDS) to promote adhesion between photoresist and the silicon substrate in the next step.
3. Negative photoresist NR7-1500P (Futurrex, Franklin, NJ) is spin-coated on the silicon wafer using a spinner (Headway Research, Garland, Texas) at 3000 rpm for 40 seconds.
4. The wafer is heated on a 150°C hotplate for 60 seconds for soft bake.
5. The wafer is then exposed on the Karl-Suss MA6 mask aligner using UV light (365 nm) for 60 seconds at an approximate intensity of 10 mW/cm².
6. The exposed wafer is then heated on a 100°C hotplate for 60 seconds for post-exposure bake.
7. Unexposed photoresist on the silicon wafer is then rinsed off by immersing in resist developer RD6 (Futurrex, Franklin, NJ) for 25 seconds.
8. The wafer is then dry etched in a deep reactive-ion etching (DRIE) system (Surface Technology Systems, UK) for an etching depth of 100 μm; the remaining photoresist is stripped off through a post O₂ ashing process in the same equipment.
9. The wafer, with the negative image of the desired pattern, is primed again with HMDS that will facilitate the peeling of PDMS off silicon substrate in next step.
10. Degassed PDMS (Dow Corning, Midland, Michigan) is poured on the top of the wafer.
11. PDMS piece is peeled off the wafer after fully curing (~24 hours at room temperature), and cut into a desired shape using a razor blade; the PDMS has the desired channel geometries at the surface.

2.2.3 Bonding

The PDMS piece is sealed by a blank PDMS cover of same size, and then bonded to a glass slide to the side with no features. The cover PDMS piece has holes punched at locations corresponding at well 2 and converging point N. The PDMS and the glass surfaces are treated by plasma using a high frequency generator (Electro-Technic Products, Chicago, IL) to promote bonding. A picture of the finished PDMS device with wavy channels is shown in Figure 2-7.

2.3 Micro Mixer

Once the flow recirculation in a ridged channel is well understood, it is incorporated in a micro mixer design to facilitate mixing by flow recirculation. Details of the discussion on the microfluidic mixer are provided in Chapter 5.

2.3.1 Device Design

The overall design of the micro mixer (Figure 2-8) is similar to the device consisting of the wavy channels, except for the patterns of the channel between M and N. The small portion of channel circled by dashed lines in the figure is the ridged channel similar to the ones discussed in section 2.1. The pattern, including 20 parallelograms, accounts for ridged channels of 2.1-millimeter in length, while the total length of the channel connecting M and N is 20 mm. Two electrodes, printed on the cover film, are to be placed outside the ridged channel portion as schematically shown in Figure 2-8.

2.3.2 Fabrication of Plastic Substrates

The fabrication processes (photolithography, hot embossing, trimming and drilling) of the micro mixer are exactly same as the process described in section 2.1. Briefly, the micro mixer is first built in a glass plate, which serves as a master to generate a nickel mold by electroplating. Plastic resins are then pressed against the mold to replicate plastic chips. They are cut into desired shapes on a CNC milling machine; and holes are drilled at the ends of the channels.

2.3.3 Electrode Printing

Electrodes are printed on a plastic thin film using screen printing technique.⁴² Figure 2-9a shows the drawing for the electrodes compiled in AutoCAD. The dashed lines indicate the outlines of the channels on the plastic part. The electrodes wires are lines of 0.3 mm wide, while the electrode pads (A and B) are circle of 1 mm in diameter. The distance between two electrodes is 3 mm.

The pattern is cut in a 0.3 mm thick stainless steel sheet by laser (Global Stencil, Austin, TX), forming a stencil. Conductive ink is obtained by dissolving carbonate paste (BQ225, DuPont, NC) in acetone at a concentration of 0.24 g/ml. An air brush (Badger, Franklin Park, IL) is used to spray the ink onto the plastic film with the electrode stencil firmly pressed against it. After a 2 hour curing in a 70 °C oven, the film with the screen printed electrodes is ready for thermal lamination. A picture of the screen-printed electrodes is shown in Figure 2-9b. The thickness of electrodes is about 5 microns.

After lamination, two 2-cm long metal wires are glued onto the electrode pads (A and B) using conductive epoxy (ITW Chemtronics, Kennesaw, GA). A picture of the finished micro mixer is shown in Figure 2-10.

2.4 Characterization of Fabrication Process

A glass master and an E-form are used in fabricating LOC plastic devices. Ideally, through the E-form (Figure 2-11b), micro features in the plastic chip (Figure 2-11c), should be identical to those in the glass master (Figure 2-11a). However, discrepancies exist between the glass master and the plastic replica. To characterize the difference, a Dektak profiler is used to measure the channel depths at 64 different locations in the glass master, the ridge heights at the corresponding locations on the E-form, and the channel depths at the corresponding locations in the plastic chip.

2.4.1 Comparison between Glass Master and E-Form

Comparing the measurements between the glass master and the E-form, it is found the ridge heights on the E-form are statistically greater than the channel depths on the glass master. The increase is averaged $0.31 \mu\text{m}$ with a variance of $0.09 \mu\text{m}$. Figure 2-12 shows the histogram of the difference between the two sets of measurements.

The expansion of E-form may result from the addition of a seeding layer between the E-form and the glass master during the electroplating process. Because glass is non-conductive material, a thin layer of silver nitride is deposited on the glass master surface to allow the growth of nickel. According to the manufacturer, a silver nitride solution is sprayed over the glass surface before it's placed into the electroplating bath. As the electroplating process is over, the whole piece is immersed in a solvent, where the seeding layer is dissolved and the nickel plate is separated from the glass master. The seeding layer, however, is not a conformal coating on the glass surface. Instead, less silver nitride is sprayed into the channel cavity, so that the seeding layer deposited on the channel surface is thinner than the rest of the glass plate surface. The non-uniformity leads to the difference between the ridge heights on the E-form and the channel depths on the glass master, and eventually contributes to the discrepancy between the resulting plastic chip and the glass master.

2.4.2 Comparison between E-Form and Plastic Chip

In comparison to the height of ridges on the E-form, the depth of the channel on the plastic chip is statistically shallower (Figure 2-13). The difference is averaged $-0.31 \mu\text{m}$ with a variance of $0.12 \mu\text{m}$. A possible cause for the shrinkage of the plastic chip is the mold shrinkage of the plastic material as it cools after the hot embossing. According to Topas Advanced Polymers,⁴³ Topas 8007 has a typical mold shrinkage value in the range of 0.6% to 0.7%. Since the feature

size is about $40\ \mu\text{m}$ (the ridge height on the E-form), the mold shrinkage reasonably explains the difference of $0.31\ \mu\text{m}$ between the E-form and the plastic substrate.

2.4.3 Comparison of Plastic Chip and Glass Master

The difference between the channels on the plastic chip and those on the glass master is a combined result of E-form expansion and plastic chip shrinkage. Figure 2-14 shows the histogram of the difference between the two sets of measurements. The average of the difference is $0\ \mu\text{m}$, indicating that the plastic replica is statistically same as its master. The variance of the difference is $0.14\ \mu\text{m}$, which is larger than either variance values in previous comparisons. This is because the electroplating and the hot embossing process both contribute to the discrepancy between the master and the replica.

Due to the inevitable errors in the electroplating and the hot embossing process, the plastic chip generally has slightly different dimensions from its glass master. Sometimes the difference can be negligible, which is the case above where the E-form expansion balances the plastic shrinkage. However in most cases, it turns out the opposite. Hence a prudential control the etching depth in the fabrication of glass master is preferred, so that the final plastic product results with a desired depth. At the same time, optimization the fabrication process is needed to minimize the variation in the difference between the plastic chip and the glass master. This, however, is beyond the scope of the thesis work.

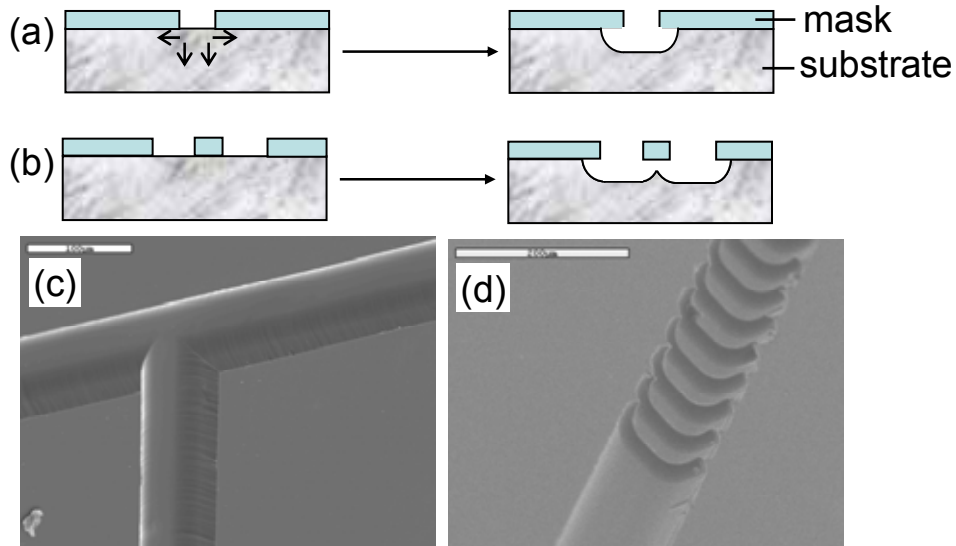


Figure 2-1. Creation of ridged channels through isotropic etching. Isotropic etching with a single continuous opening leads to a D-shaped channel (a), and the SEM picture is shown in (c). Ridges are obtained from judicious designs and isotropic etching (b), as illustrated by SEM picture of a ridged channel (d) in a microfluidic device made from cyclic olefin copolymers. The scaling bars in (c) and (d) are $100\ \mu\text{m}$ and $200\ \mu\text{m}$, respectively

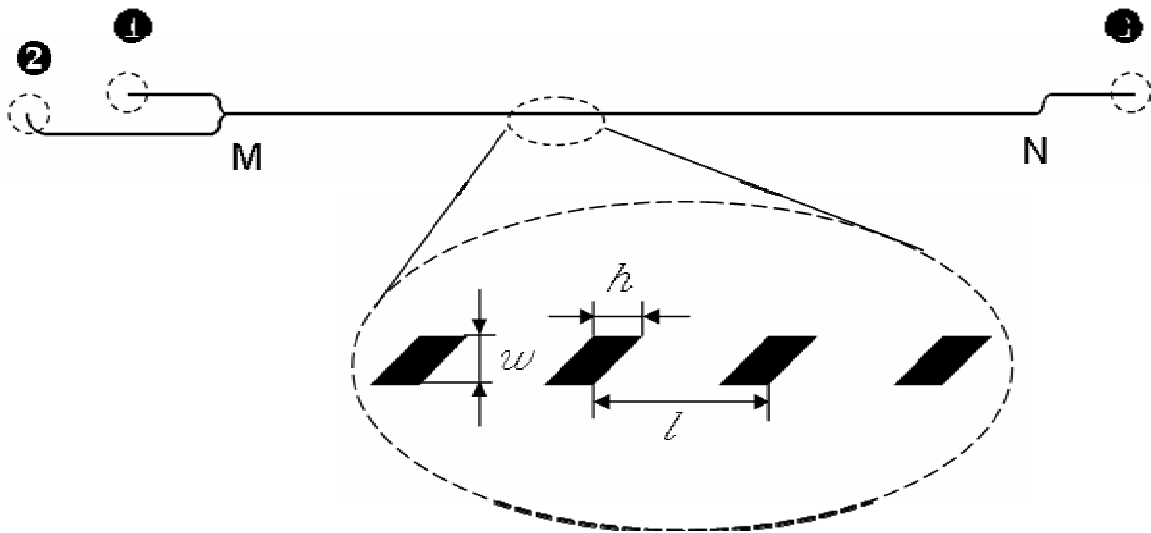


Figure 2-2. Photomask layout of a T-channel. Three wells in the layout are numbered for references in the text. The lengths of the lines connecting wells 1 and 2 to the intersection M are 4.6 and 10.2 mm respectively, while the line connecting well 3 to N is 4.6 mm long. The ridged channel portion (from M to N) is 40 mm in length. In the inset, the angle of parallelogram is 45° , $w = 30\ \mu\text{m}$, $h = 30\ \mu\text{m}$, and $l = 108\ \mu\text{m}$.

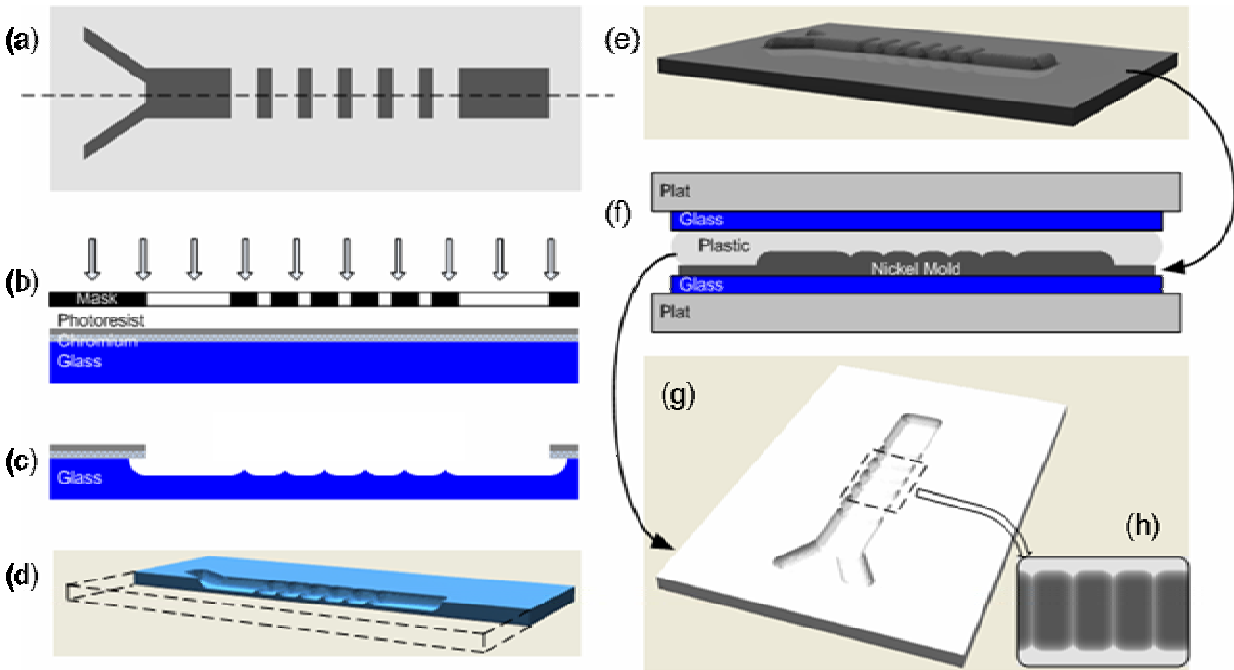


Figure 2-3. Fabrication process of plastic LOC devices. (a) photomask; (b) pre-coated glass plate, aligned with photomask, is exposed to UV light; (c) photoresist, chromium, and glass substrate are etched sequentially; (d) the remaining photoresist and chromium are stripped off the glass plate; (e) a nickel E-form is generated from the glass plate; (f) plastic resins are pressed against the E-form; (g-h) plastic chip is taken off the E-form, and trimmed into desired shape.

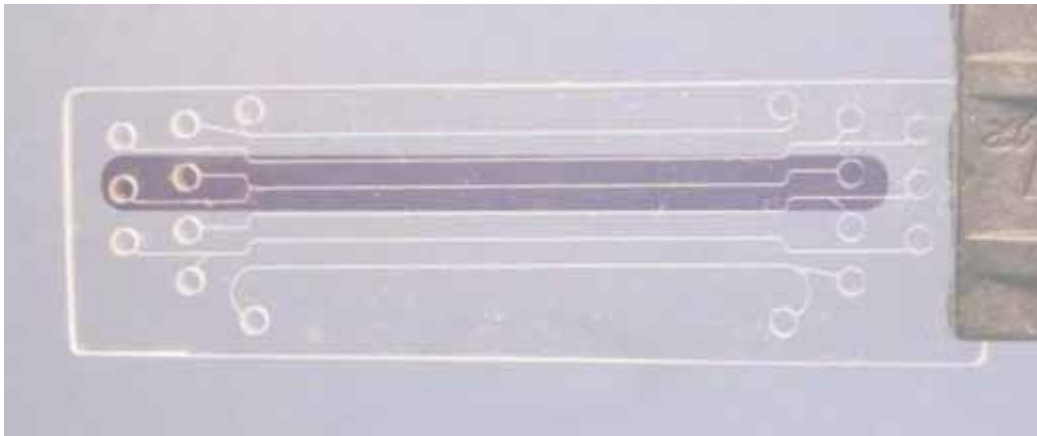


Figure 2-4. Plastic device with 6 channels. The highlighted one is the ridged channel designed for test.

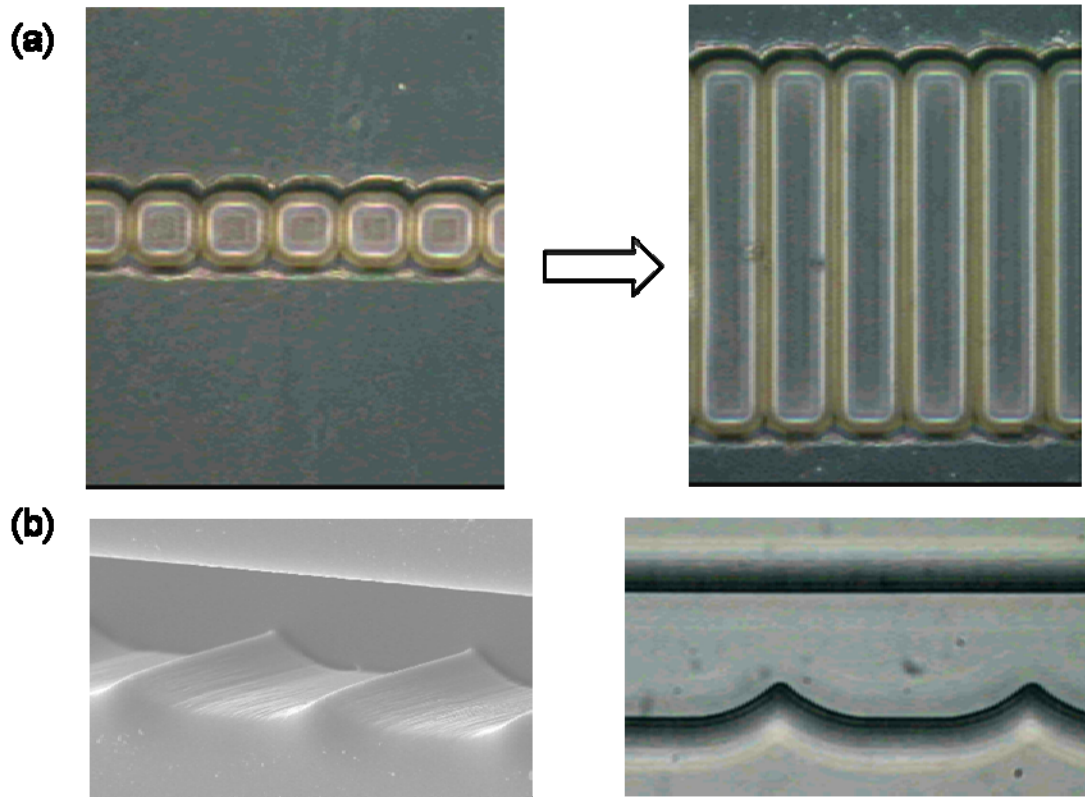


Figure 2-5. The 3D ridged channels and 2D simplified form of ridged channels. (a) Extending the width of ridged channel can minimize the variation of flow in lateral direction, thus reducing the number of dimensions by one. (b) An alternative simplification of the ridged channel is between a flat wall and a wall with profile that mimics ridged channel bottom.

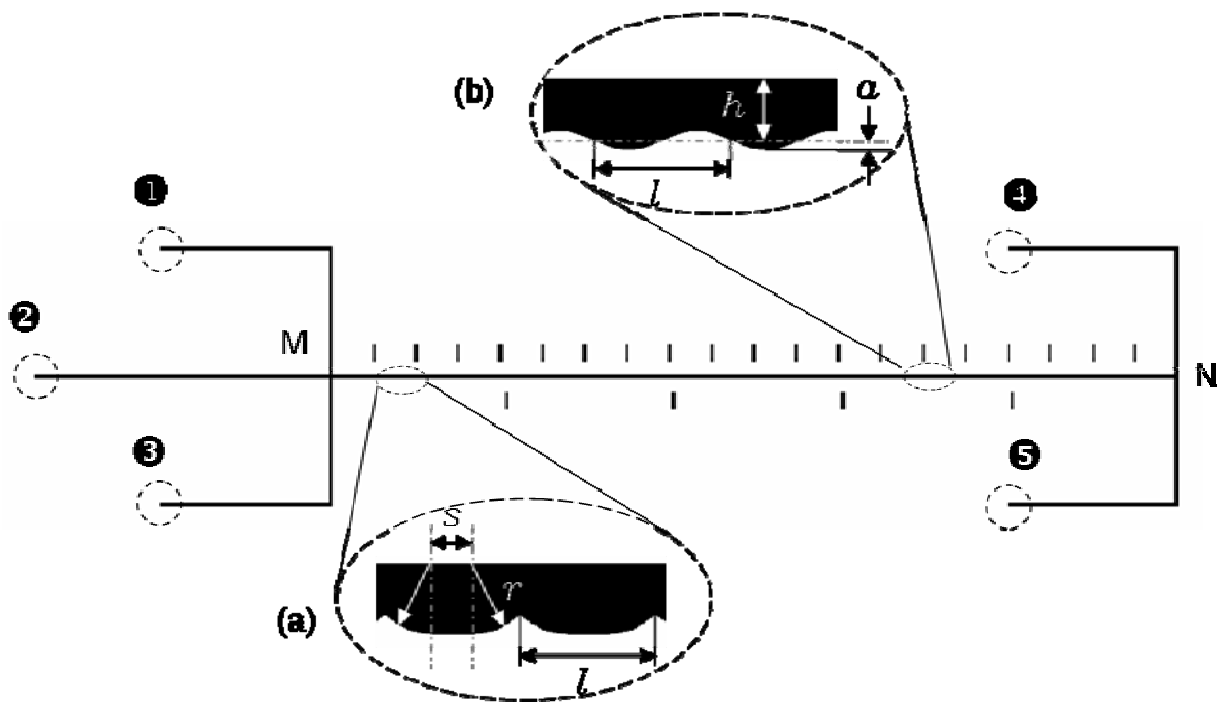


Figure 2-6. Photomask layout of wavy channels. Five wells in the layout are numbered for references in the text. The lengths of the lines connecting wells 1, 2 and 3 to the intersection M, and lines connecting well 4 and 5 to N are all 6 mm. Inset (a) shows the detailed photomask design of a 2D arc channel, whose profile mimics the bottom of ridged channels. $s = 21.2\mu\text{m}$, $r = 40\mu\text{m}$, and $l = 76.4\mu\text{m}$. Inset (b) shows the detailed photomask design of a wavy channel, whose bottom profile is a sinusoidal curve. $h = 34.5\mu\text{m}$, $a = 5.5\mu\text{m}$ and $l = 76.4\mu\text{m}$.

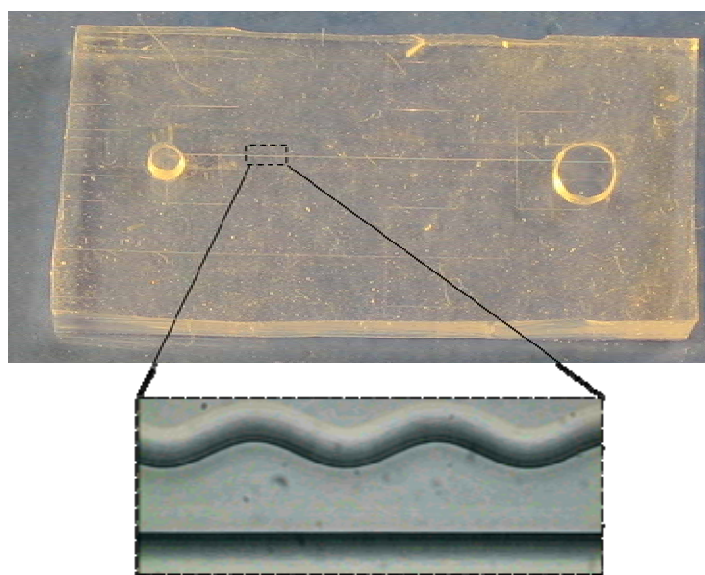


Figure 2-7. Wavy channels fabricated on PDMS substrates. The microscopic image is shown in inset.

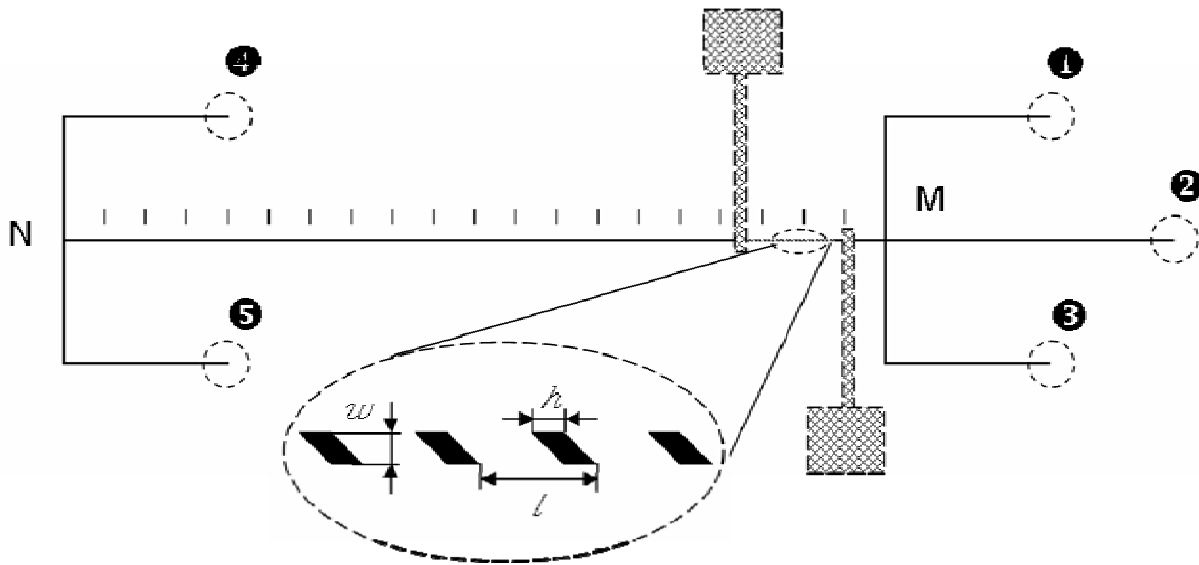


Figure 2-8. Photomask layout of a pulsed recirculation mixer. The lengths of the lines connecting wells 1, 2 and 3 to the intersection M, and lines connecting well 4 and 5 to N are all 6 mm. Two electrodes, spaced 0.3 mm, are schematically shown in the design. Between the electrodes is the ridged channel portion. Inset shows the detailed photomask design of ridged channel. The angel of parallelogram is 45° , $w = 30\mu\text{m}$, $h = 30\mu\text{m}$, and $l = 108\mu\text{m}$.

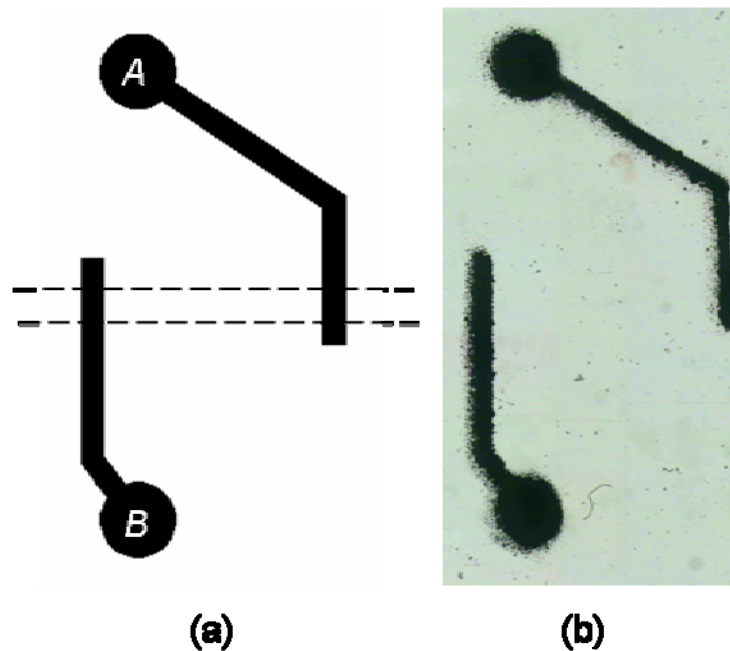


Figure 2-9. Layout and microscopic image of electrodes. The electrodes are printed on plastic film.

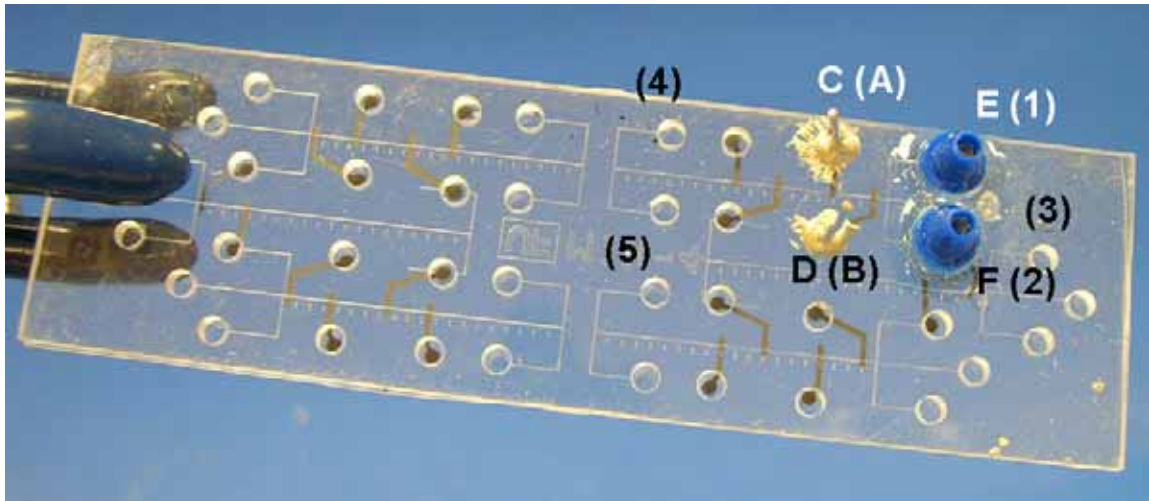


Figure 2-10. Plastic device with a pulsed recirculation mixer. Solutions are pumped into the mixer via inlets E and F, which are glued to wells 1 and 2. Wires C and D are glued to electrode pads A and B. An electric field is applied to the mixer by connecting C and D to an external power supply.

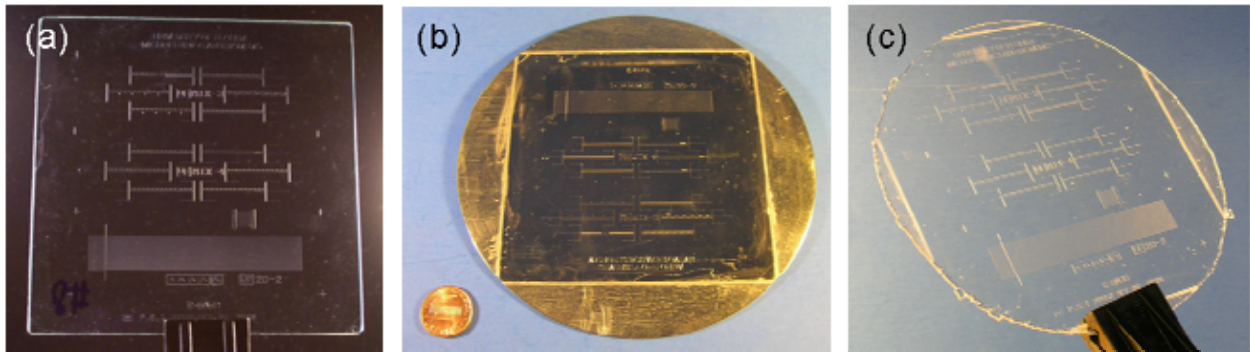


Figure 2-11. Glass master, the E-form and a plastic chip used in the work.

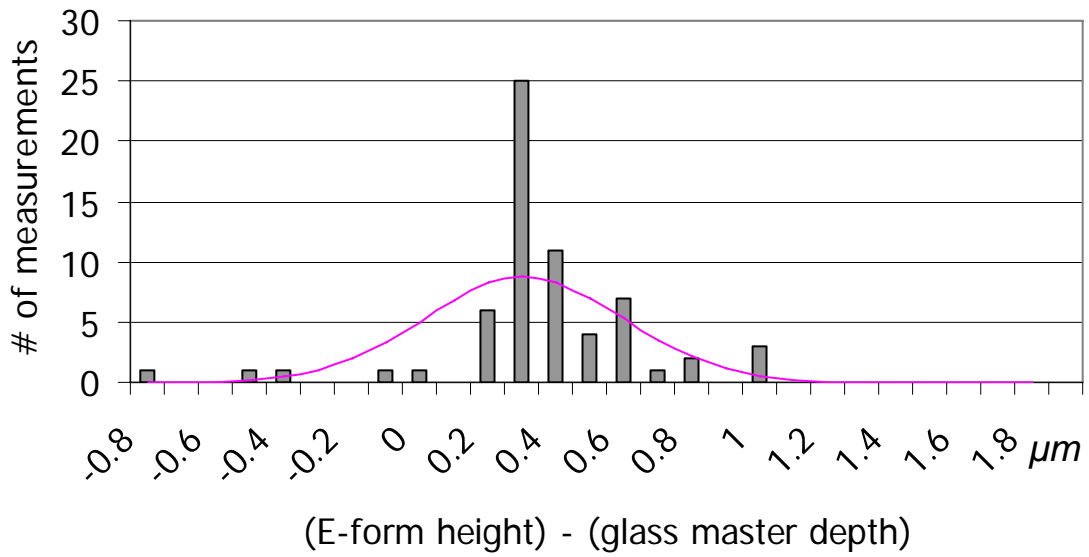


Figure 2-12. Histogram of the differences between the ridge heights on the E-form and the channel depths on the glass master. The profile of normal distribution with calculated mean and variance is also plotted.

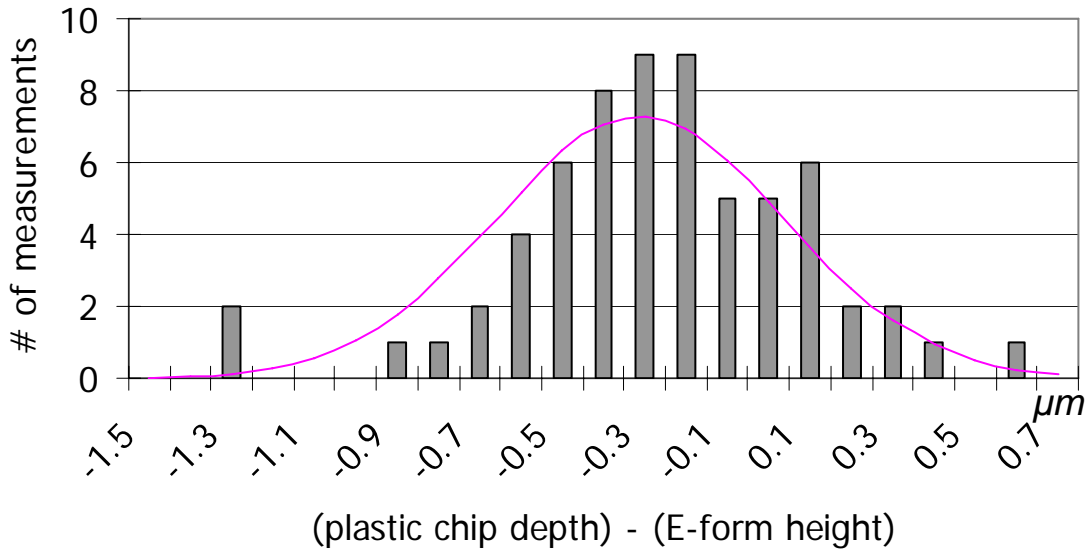


Figure 2-13. Histogram of the differences between the channel depths in the plastic chip and the ridge heights on the E-form. The profile of normal distribution with calculated mean and variance is also plotted.

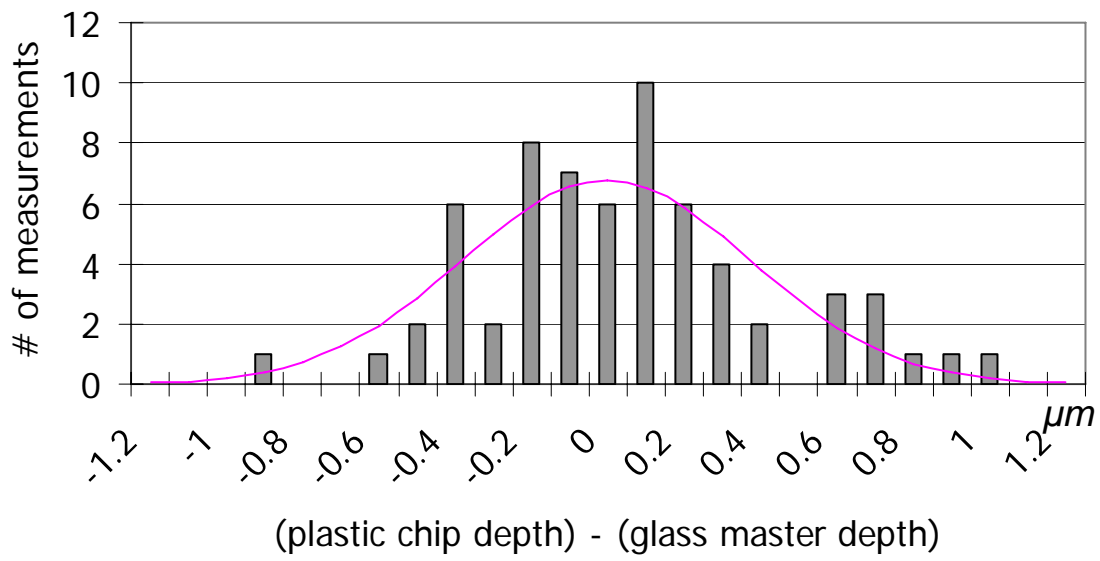


Figure 2-14. Histogram of the differences between the channel depths on the plastic chip and the channel depths on the glass master. The profile of normal distribution with calculated mean and variance is also plotted.

CHAPTER 3 DECONVOLUTION MICROSCOPY FOR FLOW VISUALIZATION*

3.1 Introduction

As explained in Chapter 1, microfluidic systems are widely used in chemical analysis and biological applications, and a thorough mixing of reagents is often required. To evaluate the efficiency of fluid mixing, flow visualization is often used. Direct flow visualization is also important for studying microflow properties, investigating flow behavior, and verifying computational fluid dynamics simulations.³⁹ The primary methods used for microscale flow visualization are particle-based flow velocimetry, such as particle image velocimetry (PIV)⁴⁴ and optical imaging techniques enabled by fluorophores or dyes. PIV measures the velocity in a two-dimension plane due to small depth-of-field of a high numerical aperture lens,⁴⁵ thus it is difficult to be used for visualization of a complex, three-dimensional flow.

Optical imaging is a flow visualization method to study fluid motions inferred from color or fluorescence intensity.³⁹ It has been used to study mixing in microflows,^{18, 20, 23, 24, 35, 37, 46-50} diffusion in a curved channel,^{51, 52} and the shape of injected samples at an intersection.^{53, 54} The majority of these optical imaging techniques acquire images from the top of a microchannel, visualizing a two-dimensional flow. Interpretation is thus straightforward when the vertical gradient components (from the top to the bottom of the channel) of flow variables are negligible. However, such top-view images can be easily misinterpreted if the flow is three-dimensional.⁵⁵ For instance, two vertical layers of unmixed flows could be mistaken as a mixed flow because an image acquired from the top may show uniform fluorescent signals across the channel. Examples of a three-dimensional flow include chaotic mixing due to transverse flows^{19, 20} and

* Part of this chapter has been published in “Deconvolution Microscopy for Flow Visualization in Microchannels”, *Analytical Chemistry*, 2007, **79**(6): p. 2576-2582.

advection in a three-dimensional serpentine channel with vertical through-holes.^{27, 55-58}

Characterization of these flows can be studied by confocal fluorescence microscopy.^{19, 24, 50}

However, such a setup is expensive and complicated, preventing it from becoming a widely used method.

This chapter aims to exploit a technique that combines a conventional optical microscope with a deconvolution method, and apply it in evaluating fluid mixing in microfluidic flows. The technique, called three-dimensional deconvolution microscopy, collects a series of images at different focal planes and then uses a computational deconvolution process to remove the out-of-focus fluorescence signal and correct the images. Compared to confocal microscopy that physically removes the out-of-focus light information via a pinhole, deconvolution microscopy employs a mathematical method to correct for optical blurring. Deconvolution microscopy has been used by medical and biological scientists for visualizing the cellular structures of tissue specimens; the details of the approach have recently been reviewed.^{59, 60} Moreover, there is software that is commercially available for the application. Compared to the confocal fluorescence microscopy, one advantage of our approach is its use of a widely-available conventional optical microscope. In addition, it does not have the drawback of the confocal microscopy that only allows limited amount of light to pass through the pinhole due to confocal requirement. The theoretical background before the description of the experimental results is briefly discussed in the end of this chapter.

3.2 Theoretical Background

Deconvolution microscopy is composed of two steps: optical sectioning and image reconstruction. Optical sectioning refers to the process of acquiring volume images by optically sectioning the solution in a channel, plane by plane via the displacement of the focal plane along the optical axis, as illustrated in Figure 3-1. The objective lens of the microscope is

consecutively adjusted in discrete steps, and a stack of two-dimensional images of different sections are collected. Since the acquired images are blurred due to contributions outside the focal plane during the image formation, a digital process—called deconvolution—is carried out to remove the blurring and to reconstruct a corrected 3D image. Optical sectioning and the deconvolution algorithms used in this work are briefly discussed as follows; additional details can be found in the literature.^{60, 61}

3.2.1 Optical Sectioning

In essence, optical sectioning samples discrete planes from a continuous light signal in a three-dimensional space. This sampling process must satisfy the Nyquist sampling theorem,^{62, 63} which requires the sampling frequency to be greater than twice the input signal bandwidth in order to assure perfect reconstruction of the original signal from the sampled version. In the spatial domain, this requires a sampling interval to be less than half of the characteristic dimension of the source signal.

A CCD camera is used to sample the discrete planes along the optical axis. The sampling interval in the axial direction (Δ_z) is defined by the spacing between two adjacent image acquisitions. The axial resolution of a microscope is defined by $r_z = \frac{1.4\lambda n}{NA^2}$, where λ is the light wavelength, n is the refractive index of media, and NA is the numerical aperture of the objective lens.⁶⁰ To meet the requirement of the Nyquist sampling theorem, then $\Delta_z \leq \frac{1}{2}r_z$, i.e.,

$$\Delta_z \leq \frac{0.7\lambda n}{NA^2} \quad (3-1)$$

3.2.2 Convolution

The images acquired via optical sectioning are degraded for two reasons: optical blurring and image degradation due to electronic noise. Optic blurring is due to the optical aberration of

light during its passage through the microscope optical lenses. Among optical aberration,⁶⁴ chromatic aberration is insignificant because band-pass filters are used in the optical system. Optic blurring occurs because each image taken at one focal plane is contaminated with the out-of-focus information from the adjacent planes above and below the examined.⁶⁰ However, this distortion is reproducible and inherent to the optical system and thus can be mathematically corrected.

The optical aberration of light in the optical system can be mathematically expressed as a convolution of the object (i.e., the fluorescein solution in the channel in this case) with a spatial function called the point spread function (PSF), which is the three-dimensional image recorded by the microscopy when the input is a point source.^{60, 61} As the most fundamental characteristic of an imaging system, PSF can be viewed as the impulse response function of a microscope in the spatial domain (see Appendix A). The resultant 3D image of a point source is thus defined by PSF, hence the intensity at any point in the image is a weighted sum of all the point sources in the channel. A mathematical description of this image formation process is given by a spatial convolution, i.e., a volume integration over space, of the spatial function of fluorescein concentration in the channel and the PSF of the microscope.⁶⁰ As a result, the images taken from the microscope deviate from the real fluorescence intensity. A deconvolution process must be undertaken to reconstruct the images by deblurring the image.

As mentioned above, the other source of the image degradation is photonic and electronic noise during image acquisition. The electronic noise of the CCD camera can be rectified by a bias image, which is taken by the camera when light to the camera is completely blocked. Non-uniformity of light source can be corrected by a flat-field image, which is taken when a fluorescein solution with uniform thickness is illuminated with the UV lamp of the microscope.

The flat-field image also compensates for any variation in the sensitivity of different pixels in the CCD camera. These images will also be used in the deconvolution process to reduce both photonic and electronic noises.

3.2.3 Deconvolution

A variety of deconvolution algorithms has been developed to remove the blurring and noise in images acquired via optical sectioning. These algorithms can be classified into three groups: inverse filter,⁶⁵ constrained iteration,⁶⁶⁻⁶⁹ and blind deconvolution.⁷⁰ Two implementations of the constrained iteration are investigated, namely the Gold algorithm⁶⁷ and the maximum likelihood estimation (MLE) by Richardson and Lucy^{68, 69}. Mathematical description of each algorithm is summarized in Appendix B, and the advantages and disadvantages of each method, as well as essential references, are listed in the **Table 3-1**. These methods are used and compared for microflow visualization, and then the best one is chosen for the mixing study as explained in the Results and Discussion.

3.3 Experimental Methodology

3.3.1 Experimental Setup

A plastic device (Figure 2-4) with ridged channels is fabricated as described in Section 2.1. It is connected to a syringe pump (KDS 100, KD Scientific, Holliston, MA) via the Nanoport® kit (Upchurch, Oak Harbor, WA). Fluorescein solution (1 μM) is pumped into the device at a preset flow rate (5.2 $\mu\text{L}/\text{min.}$, or 2.3 cm/s based on the cross-sectional area). Using the hydraulic diameter of the channel and $3.3 \times 10^{-6} \text{ cm}^2/\text{s}$ as the diffusion coefficient of fluorescein,⁷¹ the Peclet number¹⁹ of this flow is 3.9×10^3 . The device is placed on the sample stage of an inverted microscope (IX51, Olympus America Inc, Melville, NY), which is equipped with a 75W xenon lamp (U-LH75X). A 20x objective lens (Olympus) with a numerical aperture of 0.5 is used. The light pass through an excitation filter (HQ480/40, Chroma Technology, Rockingham, VT), a

beam splitter, and an emission filter (HQ535/50, Chroma Technology), and then is collected by a scientific-grade, cooled CCD camera (2184 x 1472 pixels, Apogee, Auburn, CA). The CCD pixel size is $6.8 \mu\text{m} \times 6.8 \mu\text{m}$.

3.3.2 Optical Sectioning and Image Reconstruction

Prior to the acquisition of sample images, both bias and flat-field images are collected for optical calibration of the microscopy. The bias image is taken with the camera shutter closed; it is used for rectifying the noise level of the CCD camera. The flat-field image is taken when a fluorescein solution is contained between two flat glass slides and illuminated with the UV light; it is then used for calibrating the uneven UV illumination and the variation in the sensitivity of different regions of the camera.

To collect images via optical sectioning, the microscope objective lens is moved in steps of $1 \mu\text{m}$ along the optical axis to acquire consecutive images. A total distance of $80 \mu\text{m}$ is displaced in the optical axial direction, ensuring a full sampling of the $40\text{-}\mu\text{m}$ -deep channel and enough information from the out-of-focus neighboring region. The stack of 80 images, together with the bias and the flat-field images, are then imported into AutoDeblur® and AutoVisualize® (AutoQuant Imaging Inc, Troy, NY) for deconvolution analysis. A variety of deconvolution algorithms are studied, including the inverse filter, Gold, MLE, and blind MLE. A Dell computer with Intel Pentium® 4 processor (OptiPlex GX270) is used for computation.

3.4 Results and Discussion

3.4.1 Optical Sectioning

As discussed in Section 3.2, the sampling interval in the optical axis must meet the Nyquist sampling theorem defined by Equation 3-1. The sampling distance in the axial direction (Δ_z) is $1 \mu\text{m}$, which is the adjustment step of the microscope objective lens. Using 520 nm for the emission wavelength of fluorescein, 0.5 for NA of the lens used, and 1 for the refractive index of

air, the axial resolution of the microscope (r_z) is calculated to be 2.9 μm . Therefore, our experiment condition meets the requirement of Nyquist sampling theorem, $\Delta_z \leq \frac{1}{2}r_z$.

Fluorescein solution is first pumped into the microchannel from both inlets (wells 1 and 2 in Figure 2-2). As a result, uniform fluorescence signals should be observed in the mixing channel connected to well 3. This serves as a test case to assess the accuracy of each algorithm. Using the optical sectioning described in Section 3.3, images are acquired in the region with smooth surfaces and in the region with ridges. Figure 3-2 shows the three-dimensional view of the fluorescein flow in the channel by stacking all images together in sequence. Figure 3-2a is from the region with smooth surfaces while Figure 3-2b is from the region with ridges. Although both images roughly indicate the image of the fluorescein flow (i.e., the shape of the channel), blurred edges and a hazy background are obvious. As explained in Section 3.2, these optical distortions result from the aberration of the fluorescent emission, and photonic and electronic noise. Therefore, deconvolution is performed to rectify these effects, obtaining the correct fluorescent intensity values at the points in the channel and reconstructing the actual image of the corresponding fluorescein flow.

3.4.2 Deconvolution

As discussed previously in Section 3.2, the bias image and the flat-field image are first obtained for optical calibration of the microscopy. These calibration images, as well as the image stack in Figure 3-2a, are imported into the deconvolution software, AutoDeblur®. The raw images are offset by the bias image and then normalized by the flat-field images. A variety of deconvolution algorithms are then investigated for reconstructing the images, including the inverse filter, Gold, MLE, and blind MLE algorithms mentioned above. A theoretical PSF (see

Appendix A) is used except for the blind MLE algorithm, which does not require an estimate of the PSF.

Figure 3-3 shows the images after deconvolution using different algorithms. Each image is constructed as a yz-plane, the cross-sectional view of the regular channel in Figure 3-3a. Due to isotropic etching, a D-shaped channel should be observed in the yz-plane as indicated by the dashed line in each image. As explained in Table 3-1 and in the literature,⁶⁰ the inverse filter deconvolution causes many artifacts as expected (Figure 3-3b). The strips in Figure 3-3c indicate that the Gold algorithm exhibits slow convergence and suffers from constructive artifacts.⁶⁰ The results in Figures 3-3d to 3-3g suggest that the MLE and blind MLE deliver better results, even though they take longer computation time (~30 minutes compared to a few seconds on same computer). When the number of iterations is increased from 30 to 60, the blind deconvolution algorithm generates even better results than the MLE. The corrected image after 60 iterations of the blind MLE is the closest to the channel geometry. Therefore, the blind MLE deconvolution algorithm is chosen to study mixing as follows. It's noted that even after reconstruction with the blind MLE deconvolution, fluorescence is still found outside of the channel geometry, indicating the incomplete rectification of optical distortion. The commercial deconvolution software used in current study is not tailored for microfluidic studies. A better deconvolution algorithm can be developed for visualizing microfluidic flows in microchannels.

3.4.3 Mixing in Ridged Channel

To study mixing, fluorescein solution is now introduced into the microchannel at well 1 of the device in Figure 3-4a, and pressurized water is introduced at well 2. The two streams merge at the intersection M, travel through the ridges in the channel, and finally exit at well 3. The top view of the first 36 ridges is in Figure 3-4a.

Figure 3-4b shows the fluorescent images acquired at five locations downstream of the point M. The locations correspond to the centers of the 1st, 12th, 24th, 36th, and 48th ridge in the channel as indicated in the figure. For each location, the raw image is the synthesized photograph by simply stacking together all pictures taken during optical sectioning. The reconstructed image after 60 iterations of the blind MLE for each location is shown in Figure 3-4c. The raw images from the first to the 48th ridge do not tell any trend in fluorescein distribution along the channel, whereas the reconstructed counterparts indicate the twisting flow as reported previously.^{19,20} The two streams, fluorescein and water, twist about the axis of the channel. The images indicate that the two streams started to mix at 12th ridges, and a portion of fluorescein transposed to the other side indicated by the fluorescence signal at 24th ridge. When two streams travel further along the ridged channel, mixing becomes more thorough, as indicated by the more uniform fluorescence intensity in the downstream portion of the channel (48th ridge). In addition, the reconstructed images possess much less haze and are in a better agreement with the channel geometry. The results clearly show that the reconstructed image is the better reflection of the mixture in the channel.

Using the reconstructed image in Figure 3-4c, the mixing efficiency is calculated.

Following Johnson et al.,²⁰ percentage of mixing is quantified using formula

$$mix\% = 1 - \sqrt{\frac{1}{N} \sum_1^N (I_i - I_\infty)^2} / \sqrt{\frac{1}{N} \sum_1^N (I_i^0 - I_\infty)^2} \quad (3-2)$$

where I_i is the intensity value at i^{th} pixel, I_∞ is the intensity value when solution is perfectly

mixed (at infinity), and I_i^0 is the intensity value at i^{th} pixel at the beginning. The mixing

percentages are 26%, 38%, 49%, and 59% at 12th, 24th, 36th, and 48th ridge, respectively.

These values are comparable to what reported in the literature¹⁹ for the flow with a similar Peclet number, which takes into account the difference in the flow rate and geometry.

3.5 Summary

Deconvolution microscopy is explored for imaging a 3D flow such as mixing in a microfluidic device. Compared to confocal fluorescence microscopy that is often used for visualizing a 3D flow, the deconvolution microscopic imaging employs a widely-available conventional optical microscope. Optical sectioning is straightforward for acquiring a series of images at different focal planes, and the deconvolution can simply be carried out by commercially available software. A variety of deconvolution algorithms may be used to reconstruct the corrected 3D image, depending on the optical setup, time allowed, and computational power available. After comparison among a number of deconvolution algorithms, it is found that the blind MLE deconvolution gave the best results for this microchannel application.

Deconvolution microscopy can be used to study mixing in a ridged channel of a microfabricated device. The creation of ridges in the microchannel is accomplished by judicious design and isotopic etching. Deconvolution microscopy is exploited to confirm the presence of the twisting flow in a ridged channel. Although the ridges in the channel of this work are different from the microfabricated rectangular microwells in the channel reported in the literature,^{19,37} the resultant flow patterns are similar. Mixing is evident from the experimental results using streams of fluorescein and water. Flow twisting due to the addition of the ridge structures is proved to be effective in fluid mixing in microfluidic systems.

Table 3-1. Comparison of deconvolution algorithms

| Methods | Description | Pros | Cons | References |
|-----------------------|---|---|--|------------|
| Inverse filter | Transfers images from spatial domain to Fourier domain | Simple and fast, requires less computation | Sensitive to noise, induces artificial defects, requires PSF | 65 |
| Constrained iteration | Reconstructs images in a successive process under a variety of constraints | Less susceptible to noise | Requires more computation and PSF | 66-69 |
| • Gold | | | | |
| • MLE | | | | |
| Blind deconvolution | Reconstructs images with an estimated PSF in an iterative process under constraints | Less susceptible to noise, does not require PSF | Is the most computationally intensive method | 70 |

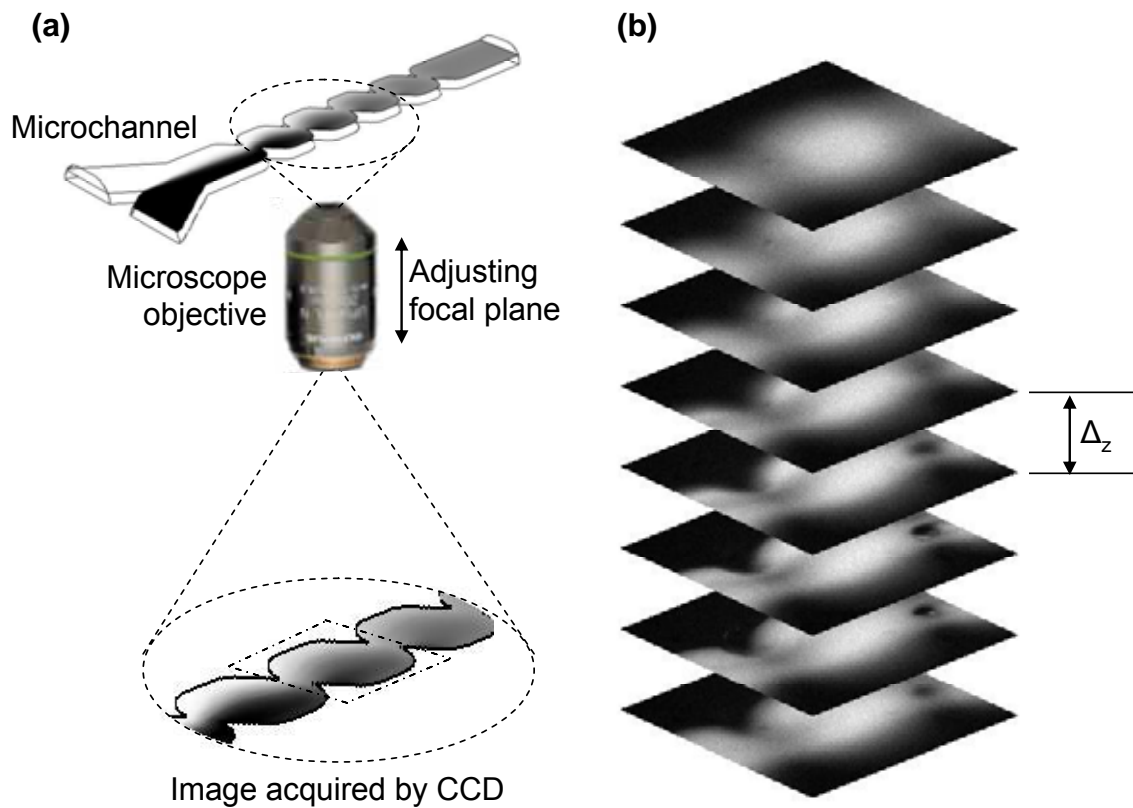


Figure 3-1. Optical sectioning process for visualization of a microfluidic flow. (a) A device with a microchannel is placed on the microscope stage. The objective lens of an inverted microscope is moved in the axial direction to obtain the image corresponding to a focal plane at a desired depth of microchannel. The image is captured by a CCD camera. (b) A stack of images are acquired by adjusting the objective lens in a discrete step, Δ_z , through the entire channel depth of the microchannel. There are more blurs in the images that are out of focus.

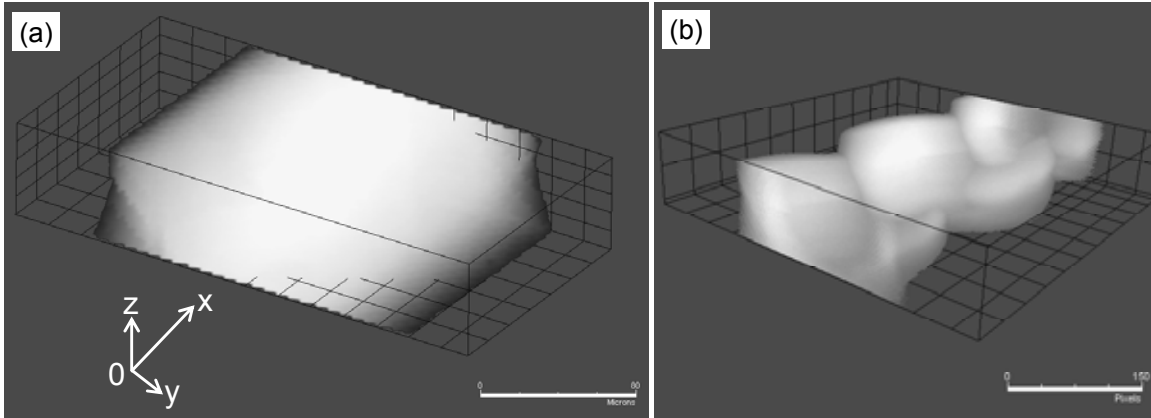


Figure 3-2. Three-dimensional view of fluorescein in a channel by stacking raw images acquired by optical sectioning. The coordinate system is defined as: x in the flow direction, y in the horizontal direction, and z in the vertical direction. (a) fluorescein flow in a regular channel; (b) fluorescein flow in the ridged channel.

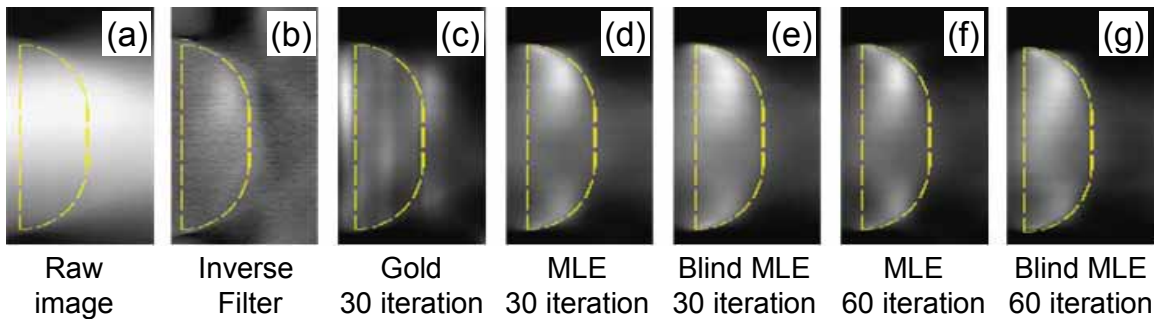


Figure 3-3. Cross-sectional image of a fluorescein flow in ridged channels. The images are reconstructed to represent the yz -plane of Figure 3-3a. The dashed lines indicate the expected shape. From left to right, pictures are the raw image (a) and corrected images using inverse filter (b), Gold algorithm with 30 iterations (c), MLE algorithm with 30 iterations (d), blind MLE with 30 iterations (e), MLE with 60 iterations (f), and blind MLE with 60 iterations (g).

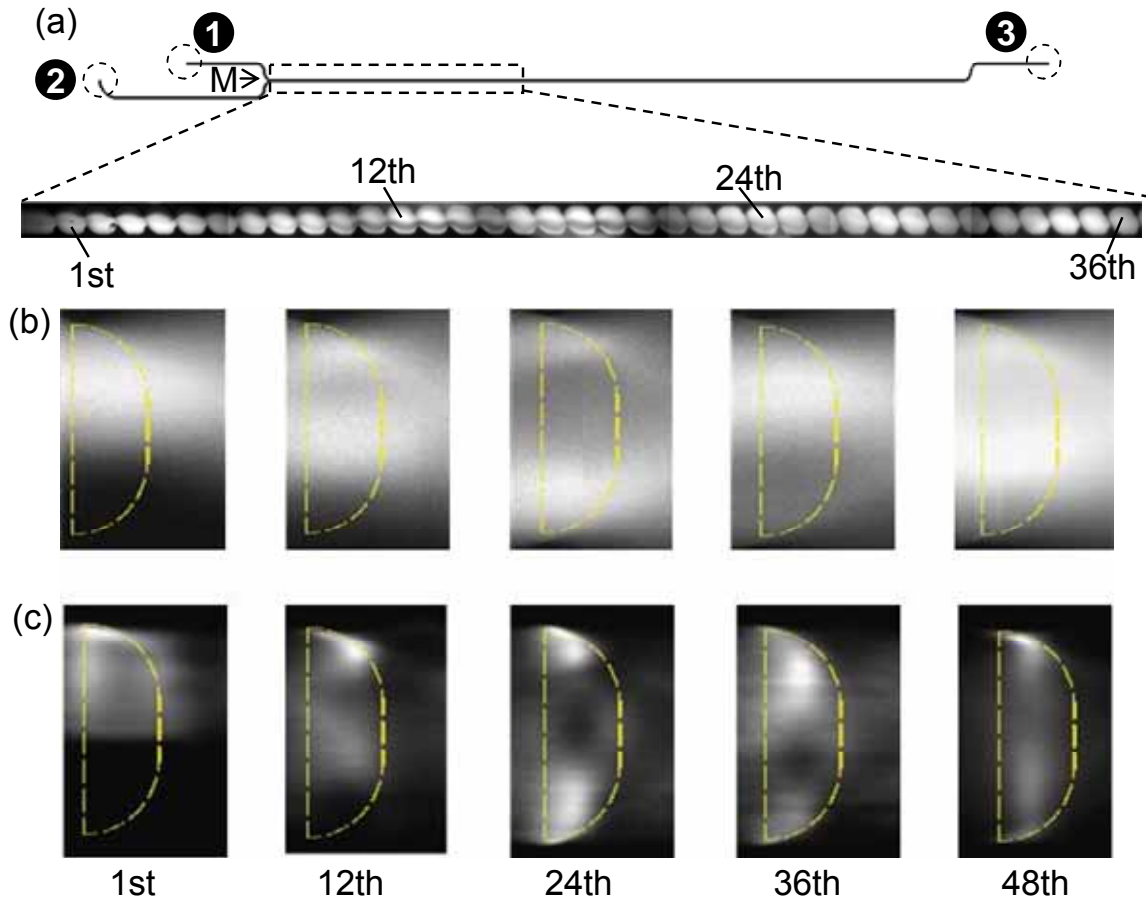


Figure 3-4. Top view and cross section views of a Poiseuille flow in ridged channels. (a) Layout of ridged channel and the expanded view of ridges in the channel. Two channels connecting to wells 1 and 2 merge at the intersection, M. (b, c) Cross-sectional views (yz -planes) of the fluorescein flow in ridged channel at different locations. Two streams of fluorescent solution and water are pumped into the channel simultaneously from wells 1 and 2, with equal flow rate (2.3 cm/s). The location for each cross-sectional view is indicated at the bottom. Views from the raw image stack are presented in (b) and views from the deconvoluted image stack are in (c).

CHAPTER 4 ELECTROOSMOTIC FLOW IN WAVY CHANNELS*

4.1 Introduction

Flow recirculation is observed in EOF in ridged channel, which is promising in enhancing fluid mixing in microchannels. In order to apply such recirculation in microfluidic mixing, we ought to explore and understand the properties of EOF in the ridged channel. However the flow is three-dimensional and difficult to deal with. A sinusoidal wavy channel is chosen as the simplified form of the ridged channel. It is a 2D channel with a varying channel cross section area; yet the variation is simple. So in this chapter, I shift focus temporarily from the ridged channel to the wavy channel. An analytical solution to EOF in a wavy channel is developed. Using the exact solution, EOF can be analytically studied and hence the flow recirculation can be consequently characterized. Once the parametric study of recirculation in the wavy channel is completed, the focus is shifted back to the recirculation in the ridged channel and the development of a microfluidic mixer using recirculation.

Electroosmotic flow, a surface phenomenon, has been investigated in this research and explored for its use in fluid mixing in microfluidic systems. As pointed out in Chapter 1, the Reynolds number of an EOF is typically less than unity. As a result, EOF is often in the regime of a creeping flow, thus governed by the Stokes equation.⁷² The velocity profile of an EOF in a microchannel of a constant cross-sectional area (e.g. a channel between two parallel flat plates) is a uniform, plug-like shape, which is different from the parabolic profile in a Poiseuille flow. EOF in microfluidic devices has been studied by many research groups.^{51, 73-81} In these studies,

* Part of this chapter has been accepted to publish in “Electroosmotically driven creeping flow in a wavy microchannel”, *Microfluid Nanofluid*, in press, DOI10.1007/s10404-008-0290-8.

an electroosmotic slip velocity is often used to simplify the flow without the calculation of the flow field in the EDL.^{74, 76, 78, 80}

While EOF is continuously exploited in a variety of applications, channels with non-uniform geometry have increasingly been designed for different microfluidic elements, including pumps,⁸² dispensers,⁸³ and mixers.²⁰ As a result, there is a growing need for a fundamental understanding about the effects of the geometry on the fluid motion and the associated transport properties. Although there are some efforts to address this need, most of them used commercial or in-house software to search for the solution of EOF. Little work focuses on obtaining analytical solutions; one example is Ghosal's study on the flow in a channel with slowly varying cross-sectional areas.⁷⁸ The solution, however, requires the wall variation small enough to validate the lubrication approximation and perturbation expansion method.

At the same time, a vast amount of studies are found in classic fluid mechanics studies for the creeping motion in periodic channel geometries.⁸⁴⁻⁹⁹ Various analytical and numerical methods have been employed in these studies. However, most of these creeping flows are either Poiseuille or Couette flows, in which no slip conditions are used at the boundary. They cannot be used for studying EOF.

In this chapter, an exact solution to an EOF in a microchannel with a periodically varying cross-sectional area is described, with a focus on a channel confined by a flat wall and a sinusoidal wall. The governing equations for the EOF are simplified using the slip velocity approximation.^{76, 100} An exact solution to the electric potential in the microchannel is obtained by solving a Poisson equation using complex function formulation and boundary integral method. The EOF is then solved by applying the same approach to a biharmonic equation of the stream function. Using the exact solutions of the electric potential and EOF flow, the effects of

the channel width and wave amplitude on the flow field are studied, and the similarity between the electric field and EOF velocity is examined. More interestingly, recirculation regions are predicted when a pressure gradient of sufficient strength in the opposite direction is added to the EOF in a wavy channel. The presence of the flow recirculation region is experimentally verified. The solution is further systematically examined over a large range of physical and geometrical parameters to determine the onset condition of the recirculation region. The onset condition is presented in the form of α (the ratio of the wave amplitude to the wavelength) as a function of h (the ratio of the channel width to the wavelength) for a given K (the ratio of the pressure force to the electrokinetic force). The size and shape of the recirculation region are also found to be dependent on K , α and h . The conclusions of recirculation in wavy channels will be used as guidelines in the investigation of recirculation in ridged channels and the design of micromixer in Chapter 5.

4.2 Governing Equations

Let's consider a two-dimensional wavy channel of infinite length between a top flat plate and a bottom sinusoidal plate, as shown in Figure 4-1. The average width of the channel is H , the wave amplitude at the bottom wall is A , and the wavelength is L . Using the Cartesian coordinate system in Figure 4-1, the channel walls are expressed as $y = H$ (top flat wall), and $y = -A \cos(2\pi x/L)$ (bottom sinusoidal wall). The top and the bottom walls are both stationary. An electric field is applied along the channel, and the average electric potential increase over one wave length is Φ_0 (i.e., EOF from the right to the left). The pressure drop over one wave length is P_0 . The flow is assumed to be steady, incompressible, and Newtonian. The fluid has density ρ , kinematic viscosity ν , and electric permittivity ε . The characteristic potential at the

edge of EDL is assumed a constant (denoted as ζ_{pot}). Because the periodic channel geometry, the flow is periodic in the x-direction.

The governing equations in this flow include the continuity equation, momentum equations, and Poisson equation:

$$\nabla \cdot \bar{V} = 0, \quad (4-1)$$

$$(\bar{V} \cdot \nabla) \bar{V} = -\frac{\nabla p}{\rho} + \nu \nabla^2 \bar{V} - \frac{\rho_e}{\rho} \nabla \phi, \quad (4-2)$$

and

$$\nabla^2 \phi = -\frac{\rho_e}{\varepsilon}, \quad (4-3)$$

where $\bar{V}(x, y)$ is the velocity vector (with u as the x component and v as the y component),

$p(x, y)$ is the pressure, $\rho_e(x, y)$ is the electric charge density and $\phi(x, y)$ is the electric potential in the fluid flow.

The boundary conditions are

$$\bar{V}(x - L/2, y) = \bar{V}(x + L/2, y), \quad (4-4)$$

$$p(x - L/2, y) = p(x + L/2, y) + P_0, \quad (4-5)$$

$$\phi(x - L/2, y) = \phi(x + L/2, y) - \Phi_0, \quad (4-6)$$

and

$$\bar{V}|_{walls} = 0. \quad (4-7)$$

In the bulk flow (also called as the outer flow region, relative to the double layer¹⁰⁰), the electric charge is neutral. As a result, the Lorentz force is dropped from the momentum Equation 4-2, which becomes the incompressible Navier-Stokes equation,

$$(\bar{V} \cdot \nabla) \bar{V} = -\frac{\nabla p}{\rho} + \nu \nabla^2 \bar{V}, \quad (4-8)$$

and the Poisson equation (Equation 4-3) becomes the Laplace equation by dropping the charge density term,

$$\nabla^2 \phi = 0 \quad (4-9)$$

Since the double layer thickness is much smaller than the channel width, the effect of the flow in the double layer (also called as the inner flow region) on the outer flow can be approximated by the slip velocity.^{74, 76, 78, 80, 100} The effective slip boundary condition is described by the Helmholtz-Smoluchowski equation,¹⁴

$$\bar{V}|_{walls} = -\eta \nabla \phi|_{walls}, \quad (4-10)$$

where η is the electroosmotic mobility, defined in Equation 1-21 as $\eta = -\frac{\epsilon \zeta_{pot}}{\rho \nu}$.

To non-dimensionalize x , y , u , v , p , and ϕ in Equations 4-1, and 4-4 to 4-10, the following is introduced: $[x^* = \frac{x}{L/2\pi}, y^* = \frac{y}{L/2\pi}, u^* = \frac{u}{2\pi\eta\Phi_0/L}, v^* = \frac{v}{2\pi\eta\Phi_0/L},$

$p^* = \frac{p}{\rho\nu\eta\Phi_0(2\pi/L)^2}, \phi^* = \frac{\phi}{\Phi_0}]$. It should be noted that the scale of the convection term in the

momentum equation is on the order of Reynolds number, $Re = \frac{uL}{\nu}$. As EOF is typically in the regime of a creeping flow where $Re \ll 1$, the inertial term is then dropped from the momentum equation (Equation 4-8),

$$\nabla p^* = \nabla^2 \bar{V}^* \quad (4-11)$$

For clarity, the superscript stars in the dimensionless variables are dropped hereinafter.¹⁰¹

To characterize the effects of the channel geometry, two dimensionless parameters related to the channel geometry are introduced: scaled wave amplitude $\alpha = 2\pi A/L$ (the ratio of the wave amplitude to the wavelength, the characteristic slope of the sinusoidal wall) and scaled channel width $h = 2\pi H/L$ (the ratio of the channel width to the wavelength).⁹⁶ By using a stream function $\psi(x, y)$ and taking the curl of the momentum equation (Equation 4-11), a biharmonic equation for ψ is obtained,

$$\nabla^4 \psi = 0 \quad (4-12)$$

For the given solution domain as shown in Figure 4-2a, the resulting non-dimensionalized boundary conditions include the following equations,

$$\psi(x - \pi, y) = \psi(x + \pi, y), \quad (4-13)$$

$$p(x - \pi, y) = p(x + \pi, y) + \frac{P_0 (L/2\pi)^2}{\rho \nu \eta \Phi_0}, \quad (4-14)$$

$$\hat{t} \cdot \nabla \psi|_{\text{walls}} = 0, \quad (4-15)$$

$$\hat{n} \cdot \nabla \psi|_{\text{walls}} = -\hat{t} \cdot \nabla \phi|_{\text{walls}}, \quad (4-16)$$

$$\phi(x - \pi, y) = \phi(x + \pi, y) - 1, \quad (4-17)$$

and

$$\hat{n} \cdot \nabla \phi|_{\text{walls}} = 0, \quad (4-18)$$

where (\hat{t}, \hat{n}) are the unit vectors in the tangential and normal directions with the respect to the walls.

4.3 Formulation of Solutions

Since $\phi(x, y)$ is uncoupled from $\psi(x, y)$, it can be solved separately from Equation 4-9 with boundary conditions given by Equations 4-17 and 4-18. Subsequently, $\psi(x, y)$ can be obtained by solving Equation 4-12 with the boundary conditions (Equations 4-13 to 4-16).

4.3.1 Electric Potential

Using complex functions,¹⁰² a general solution to the Laplace equation (Equation 4-9) is written as,

$$\phi(x, y) = Ax + 2\Re[G(\zeta)], \quad (4-19)$$

where $\zeta = y/2 + ix/2$ is a complex variable; \Re and \Im denote the real and imaginary parts of a complex value; A is a real constant; $G(\zeta)$ is an arbitrary analytical periodic complex function satisfying the periodic boundary conditions in the x-direction $G(y/2 + (x - \pi)i/2)$

$= G(y/2 + (x + \pi)i/2)$. By substituting Equation 4-19 into the periodic boundary condition (Equation 4-17), A can be simply determined as $A = 1/(2\pi)$.

The complex function $G(\zeta)$ can be expressed as an integral along the channel boundary based on Cauchy integral formula,¹⁰³

$$G(\zeta) = \frac{1}{2\pi i} \int_{+\infty}^{-\infty} \frac{G^\varphi(x)}{\varphi(x) - \zeta} \varphi'(x) dx + \frac{1}{2\pi i} \int_{-\infty}^{+\infty} \frac{G^\beta(x)}{\beta(x) - \zeta} \beta'(x) dx \quad (4-20)$$

where $G^\varphi(x) = G(\varphi(x))$, $G^\beta(x) = G(\beta(x))$, and the complex functions $\varphi(x) = (h + ix)/2$ and $\beta(x) = (-\alpha \cos x + ix)/2$ are the profiles of top and bottom walls in the complex plane.

Substituting the complex function $\phi(x, y)$ given by Equation 4-19 into the boundary condition in Equation 4-18, and employing Cauchy-Riemann equations,

$$\frac{\partial}{\partial x} G(\zeta) = i \frac{\partial}{\partial y} G(\zeta) \quad (4-21)$$

We have

$$\frac{d}{dx} \Re[G^\varphi(x)] = 0 \quad (4-22)$$

at the top flat wall and

$$\frac{1}{2\pi} \alpha \sin(x) + 2 \frac{d}{dx} \Re[G^\beta(x)] = 0 \quad (4-23)$$

at the bottom sinusoidal wall. In order to determine uniquely the complex function $G(\zeta)$,

additional equations are needed to complete Equations 4-22 and 4-23. We define a series of analytic complex functions

$$F_n(\zeta) = \exp(2n\zeta) \quad (4-24)$$

where $n \in \mathbb{Z}$. Note that $F_n(\zeta) \cdot G(\zeta)$ is an analytic function, since $F_n(\zeta)$ and $G(\zeta)$ are both

analytic. Based on Cauchy integral theorem, the integral of an analytic complex function on a closed contour (path ABCDA in Figure 4-2b) is zero,

$$\oint_{ABCD} F_n(\zeta)G(\zeta)d\zeta = 0 \quad (4-25)$$

As both $F_n(\zeta)$ and $G(\zeta)$ have a period of 2π , the integral along BC balances the integral along

DA. Hence the sum of integrals along path AB and CD is zero,

$$\int_{\pi}^{-\pi} \exp(2n\varphi(x))G^\varphi(x)\varphi'(x)dx + \int_{-\pi}^{\pi} \exp(2n\beta(x))G^\beta(x)\beta'(x)dx = 0 \quad (4-26)$$

Equations 4-22, 4-23 and 4-26 form a complete set of equations to solve $G^\varphi(x)$ and

$G^\beta(x)$. The detailed solving procedure is detailed in Appendix C. $G(\zeta)$ is subsequently obtained from Equation 4-20, and $\phi(x, y)$ is determined from Equation 4-19.

Since the electric field is defined as $\vec{E} = -\nabla\phi$, the tangential electric field strength along walls, which is used in solving stream function, is obtained from

$$E_t^\varphi(x) = 2 \frac{d}{dx} \Im[G^\varphi(x)] - \frac{1}{2\pi}, \quad (4-27)$$

and

$$E_t^\beta(x) = \frac{2 \frac{d}{dx} \Im[G^\beta(x)] - \frac{1}{2\pi}}{\sqrt{1 + \alpha^2 \sin^2(x)}} \quad (4-28)$$

4.3.2 Stream Function

The same approach is also used to obtain the solution of the biharmonic equation (Equation 4-12). Using the periodic boundary condition (Equation 4-13), a general solution to the biharmonic equation is written as,

$$\psi(x, y) = By^2 + Cy^3 + \left(R(\zeta) + \overline{R(\zeta)} \right) + y \left(Q(\zeta) + \overline{Q(\zeta)} \right), \quad (4-29)$$

where $R(\zeta)$ and $Q(\zeta)$ are arbitrary periodic analytical functions satisfying the periodic boundary conditions in the x-direction $R(y/2 + (x - \pi)i/2) = R(y/2 + (x + \pi)i/2)$ and $Q(y/2 + (x - \pi)i/2) = Q(y/2 + (x + \pi)i/2)$; B and C are real-valued constants.^{96, 102}

Using Equations 4-14, 4-21 and 4-29, the pressure can be expressed as

$$p(x, y) = p_c + 6Cx - i \left(Q'(\zeta) - \overline{Q'(\zeta)} \right), \quad (4-30)$$

where p_c is a reference pressure, an arbitrary constant, and $Q'(\zeta)$ is the derivative of $Q(\zeta)$

with respect to ζ . From the periodic boundary condition in Equation 4-14, the constant C is

determined as

$$C = -\frac{K}{12\pi}, \quad (4-31)$$

where

$$K = \frac{P_0 (L/2\pi)^2}{\rho\nu\eta\Phi_0}, \quad (4-32)$$

is a dimensionless parameter representing the ratio of pressure force to electrokinetic body force

in the fluid flow. Therefore, the stream function (Equation 4-29), pressure (Equation 4-30), and

velocities are expressed as,

$$\psi(x, y) = By^2 - \frac{K}{12\pi} y^3 + 2\Re[R(\zeta) + yQ(\zeta)], \quad (4-33)$$

$$p(x, y) = p_c - \frac{K}{2\pi} + 2\Im[Q'(\zeta)], \quad (4-34)$$

$$u(x, y) = 2By - \frac{K}{4\pi} y^2 + 2\frac{\partial}{\partial x} \Im[R(\zeta)] + 2\Re[Q(\zeta)] + 2y\frac{\partial}{\partial x} \Im[Q(\zeta)], \quad (4-35)$$

and

$$v(x, y) = -\left(2\frac{\partial}{\partial x} \Re[R(\zeta)] + 2y\frac{\partial}{\partial x} \Re[Q(\zeta)] \right). \quad (4-36)$$

Using the Cauchy integral formula, $R(\zeta)$ and $Q(\zeta)$ can be written as

$$R(\zeta) = \frac{1}{2\pi i} \int_{+\infty}^{-\infty} \frac{R^\phi(x)}{\phi(x) - \zeta} \phi'(x) dx + \frac{1}{2\pi i} \int_{-\infty}^{+\infty} \frac{R^\beta(x)}{\beta(x) - \zeta} \beta'(x) dx, \quad (4-37)$$

and

$$Q(\zeta) = \frac{1}{2\pi i} \int_{+\infty}^{-\infty} \frac{Q^\phi(x)}{\phi(x) - \zeta} \phi'(x) dx + \frac{1}{2\pi i} \int_{-\infty}^{+\infty} \frac{Q^\beta(x)}{\beta(x) - \zeta} \beta'(x) dx, \quad (4-38)$$

where $R^\varphi(x) = R(\varphi(x))$, $R^\beta(x) = R(\beta(x))$, $Q^\varphi(x) = Q(\varphi(x))$, and $Q^\beta(x) = Q(\beta(x))$.

Substituting Equation 4-33 into Equations 4-15 and 4-16, the boundary conditions at the top flat wall yield

$$\frac{d}{dx} \Re[R^\varphi(x)] + h \frac{d}{dx} \Re[Q^\varphi(x)] = 0 \quad , \quad (4-39)$$

and

$$Bh - \frac{K}{4\pi} h^2 + \frac{d}{dx} \Im[R^\varphi(x)] + \Re[Q^\varphi(x)] + h \frac{d}{dx} \Im[Q^\varphi(x)] = \frac{1}{2} E_t^\varphi(x) \quad . \quad (4-40)$$

And at the bottom periodical wall, we have

$$B(-\alpha \cos(x))^2 - \frac{K}{12\pi} (-\alpha \cos(x))^3 + 2\Re[R^\beta(x)] + 2(-\alpha \cos(x))\Re[Q^\beta(x)] = 0 \quad , \quad (4-41)$$

and

$$\begin{aligned} & B(-\alpha \cos(x)) - \frac{K}{4\pi} (-\alpha \cos(x))^2 + \frac{d}{dx} \Im[R^\beta(x)] + \Re[Q^\beta(x)] + (-\alpha \cos(x)) \frac{d}{dx} \Im[Q^\beta(x)] \\ & = \frac{1}{2} E_t^\beta(x) \sqrt{1 + \alpha^2 \sin^2(x)} \quad . \quad (4-42) \end{aligned}$$

Taking Cauchy integrals for $F_n(\zeta) \cdot R(\zeta)$ and $F_n(\zeta) \cdot Q(\zeta)$ along a contour $ABCD$

shown in Figure 4-2b, the integral in this closed contour is zero according to the properties of an analytic function. Since the integral along BC cancels the integral along DA, the sum of integrals along path AB and CD is zero:

$$\int_{\pi}^{-\pi} \exp(2n\varphi(x)) R^\varphi(x) \varphi'(x) dx + \int_{-\pi}^{\pi} \exp(2n\beta(x)) R^\beta(x) \beta'(x) dx = 0 \quad , \quad (4-43)$$

and

$$\int_{\pi}^{-\pi} \exp(2n\varphi(x)) Q^\varphi(x) \varphi'(x) dx + \int_{-\pi}^{\pi} \exp(2n\beta(x)) Q^\beta(x) \beta'(x) dx = 0 \quad . \quad (4-44)$$

Equations 4-39 to 4-44 form a complete set of equations to solve $R^\varphi(x)$, $R^\beta(x)$, $Q^\varphi(x)$,

and $Q^\beta(x)$. $R(\zeta)$ and $Q(\zeta)$ are then obtained from equations Equation 4-37 and 4-38, and

subsequently substituted into equation 4-29 to yield the desired $\psi(x, y)$.

To recapitulate, the problem of solving the harmonic and biharmonic equations has been reduced to solving a set of one-dimensional periodic functions. They can be solved efficiently by using highly accurate spectral (Fourier series) method. The solution to the set of the complex periodic functions $\Theta(x)=\{G^\varphi(x), G^\beta(x), R^\varphi(x), R^\beta(x), Q^\varphi(x), \text{ and } Q^\beta(x)\}$ can be sought in the form of Fourier series as

$$\Theta(x) = \sum_{m=-\infty}^{+\infty} \theta_m \exp(-imx) \quad (4-45)$$

where $\theta_m = \{g_m^\varphi, g_m^\beta, r_m^\varphi, r_m^\beta, q_m^\varphi, q_m^\beta\}$ are the respective Fourier coefficients. In the absence of singularity of the field variables, the series solution converges exponentially. Hence only 10-40 terms of the Fourier series are typically needed, depending on the values of (K, α, h) , to ensure that the error in the solutions for the electric and velocity fields do not exceed a predefined threshold value (10^{-8} in this study).

For the infinite interval of integration defined in Equations 4-20, 4-37 and 4-38, the interval is split into three parts: $(-\infty, -L_{\text{int}})$, $[-L_{\text{int}}, L_{\text{int}}]$, and (L_{int}, ∞) . The middle interval, $[-L_{\text{int}}, L_{\text{int}}]$, is bounded so that it can be accurately and efficiently evaluated using the built-in adaptive quadrature routine based on Simpson's rule in the MATLAB. In the present study, $L_{\text{int}} = 1,024\pi$ and a tolerance of 10^{-8} are used. For the unbound intervals, the details of the evaluation of the velocity are illustrated below. From Equation 4-35 $u(x, y)$ can be rewritten as

$$u(x, y) = 2By - \frac{K}{4\pi} y^2 + \Re \left[\frac{1}{2\pi i} \int_{-\infty}^{+\infty} \text{int_}u(\xi) d\xi \right], \quad (4-46)$$

where the integrand is

$$\begin{aligned} \text{int_}u(\xi) = & \frac{R^\varphi(\xi)}{(\varphi(\xi) - z)^2} \varphi'(\xi) - \frac{R^\beta(\xi)}{(\beta(\xi) - z)^2} \beta'(\xi) + 2 \left(\frac{Q^\varphi(\xi)}{\varphi(\xi) - z} - \frac{Q^\beta(\xi)}{\beta(\xi) - z} \right) \\ & + y \left(\frac{Q^\varphi(\xi)}{(\varphi(\xi) - z)^2} \varphi'(\xi) - \frac{Q^\beta(\xi)}{(\beta(\xi) - z)^2} \beta'(\xi) \right), \quad z = (y + ix)/2 \end{aligned}$$

Typically, an asymptotic behavior, $\Re \left[\frac{\text{int}_- u(\xi)}{2\pi i} \right] \sim a_2 / \xi^2 + a_3 / \xi^3 + \dots$, is clearly established for $|\xi| > 10\pi$. For $|\xi| > 100\pi$, the asymptotic approximation becomes a very accurate representation of the integrand. Hence, to ensure sufficient overall accuracy, $L_{int} = 1,024\pi$ is used and $\Re \left[\frac{1}{2\pi i} \int_{L_{int}}^{+\infty} \text{int}_- u(\xi) d\xi \right] \sim \frac{a_2}{L_{int}}$. The constant a_2 depends on $\{\xi, K, \alpha, h\}$ but can be reliably determined for each set of position, flow condition, and geometric parameters via a simple polynomial fit for large values of $|\xi|$ using $1/|\xi|$ as a variable. The leading order asymptotic error of the integration is estimated to be $\frac{a_3}{2L_{int}^2}$ which is close to 10^{-8} for $|a_2| < 0.8$ (as is the case in the present study) and $L_{int} = 1,024\pi$.

The detailed solution procedures for θ_m in Equation 4-45 are provided in the Appendix C.

4.4 Results and Discussion

4.4.1 Electric Potential

The electric potential distribution in a wavy channel depends on the scaled channel width (h) and the scaled wave amplitude (α) as illustrated by the plot of equipotential lines (Figures 4-3 and 4-4). The plots are based on the assumption that a fluid with uniform properties is filled in the channel, a uniform zeta potential exists on the channel walls.

Figure 4-3 shows the variation in the electric potential distribution as a function of α while the h is fixed at 2.5. The baseline is in Figure 4-3a when the wave amplitude is zero (i.e., the bottom wall is also flat). The exact solution gives a series of equidistant parallel lines normal to the channel walls. Therefore, the electric field strength is uniform with the same magnitude along walls, as shown in Figures 4-3e (top wall) and 4-3f (bottom wall) when $\alpha = 0$. When the

bottom wall becomes corrugated as in Figure 4-3b to 4-3d, the equipotential lines spread out. The electric field strength at both walls becomes uneven as indicated in Figures 4-3e (top wall) and 4-3f (bottom wall) when $\alpha \neq 0$. The result also predicts that the electric field strength is strong at the neck area ($x = \pm\pi$) and weak at the trough ($x = 0$). The variation of the electric field strength increases with the wave amplitude of the bottom wall. In addition, the variation for the wavy bottom wall (Figure 4-3f) is larger than for the flat top wall (Figure 4-3e).

Figure 4-4 shows the effect of the channel width on the electrical field distribution in a wavy channel. The scaled width of channel, $h = 2\pi H/L$, varies from 0.6 to 5 while the scaled wave amplitude, $\alpha = 2\pi A/L$, is fixed at 0.5. As h increases, the top wall is further away from the bottom wave wall. As a result, the equipotential lines spread more uniformly. The electric strength profile at top flat wall is approaching uniform ($h \geq 2.5$ in Figure 4-4e), while the profile at bottom wall approaches a sinusoidal shape ($h \geq 2.5$ in Figure 4-4f). This result can be explained by the fact that the electric potential distribution at the walls is more dominated by the local geometry when they are further apart.

4.4.2 Flow Velocity

An EOF at a very small Reynolds number can be viewed as a creeping flow with the velocity of its moving boundaries being proportional to the electric field strength at the wall surface. The geometric parameters, α and h , directly affect the flow in the wavy channel in the absence of electric field; the superposition of the electric field E , which also depends on α and h in addition to the zeta potential, compounds the influence of α and h on the flow pattern. A major focus is thus to use the exact solution to elucidate the effects of α and h on the flow pattern and its interplay with the imposed electric field.

Figure 4-5 shows the effect of the scaled wave amplitude, α , on the streamlines and velocity field for $h = 2.5$ and $K = 0$ ($P_0 = 0$). In Figure 4-5a to 4-5d, the streamlines of an EOF conform to the curvature of the walls of any wave amplitude, and there is no flow separation observed even when the bottom wall is strongly modulated. The absence of flow separation is also confirmed by the velocity profiles in Figure 4-5e to Figure 4-5h. There is no backflow in the plot of velocities when the wave amplitude increases. In contrast, flow separation has been reported in a creeping Poiseuille flow and creeping Couette flow in wavy channels of large wave amplitude in the absence of an electric field by other researchers.^{91, 95, 97, 104} The difference between electroosmosis-driven and pressure-driven flows lies in the fact that the electric field provides a sufficient near-wall momentum in an electroosmosis-driven flow to prevent any back flow near the wall and makes the near-wall flow separation impossible to develop.

Figure 4-6 shows the effect of the channel width on the velocity field in a wavy channel. The scaled width of channel, h , varies from 0.6 to 5 while the scaled wave amplitude, α , is fixed at 0.5. As h increases, the streamline pattern simply becomes more uniform (Figure 4-6a), so does the velocity profile of the EOF. Again, there is no flow separation observed in all cases. It should be noted that the lack of flow separation, i.e., the absence of a dead volume, is a desirable feature of the EOF when it is used for electrophoresis and other applications in microfluidic devices.

The effect of the channel geometry on the flow rate of EOF is also studied. Figure 4-7 shows the flow rate as a function of α/h with different h . The flow rate is normalized against the regular channel with same channel width. The result indicates that the flow rate decreases at a parabolic rate for small amplitudes, and at a quasi-linear rate for large amplitudes. As the wave

amplitude is approaching to the channel width ($\alpha/h \rightarrow 1$), the gap between the top and bottom walls diminishes and the flow rate drops close to zero.

4.4.3 Similarity between Flow Velocity and Electric Field

The similarity between the flow velocity and the electric field is examined and shown in Figure 4-8. The data suggests a high similarity between the plot of the electric field and the streamline pattern. This similarity also exists between the electric field vectors and the velocity vectors.

The similarity between the electric field and the EOF velocity field of arbitrary channel geometry has been mathematically and experimentally verified.^{80, 100} The following assumptions are made for verification, including (1) the channel walls possess a constant uniform zeta potential; (2) no singularity exists at channel wall profile; and (3) there is a negligible applied pressure gradient in EOF.

Since $\vec{E} = -\nabla\phi$, Poisson equation (Equation 4-9) is rewritten as

$$\nabla \cdot \vec{E} = 0. \quad (4-47)$$

According to Faraday's law of induction, the curl of an electric field equals to the vector rate of decrease of magnetic flux density with time, which is typically negligible in EOF. Hence, the curl of the electric field is zero,

$$\nabla \times \vec{E} = 0. \quad (4-48)$$

For channels with uniform zeta potential, the boundary conditions in Equations 4-16 and 4-18 become

$$\vec{E}|_{\text{walls}} = \vec{V}|_{\text{walls}}, \quad (4-49)$$

and

$$\hat{n} \cdot \vec{E}|_{\text{walls}} = 0. \quad (4-50)$$

The hypothesized solution ($\vec{V} = \vec{E}$) are examined by plugging it back to the governing equations and the boundary conditions in Equations 4-11 to 4-18. Employing the assumptions and the properties of \vec{E} in Equations 4-47 to 4-50, it is found that the governing equations are satisfied and the boundary conditions are met. Hence the solution $\vec{V} = \vec{E}$ is a valid solution, and as a result $\nabla \times \vec{V} = 0$. The electroosmotic flow velocity field is thus a conservative vector field, meaning the EOF is irrotational. This explains why a flow separation is absent in EOF in a wavy channel whereas a creeping Poiseuille or Couette flow in the same wavy channel may experience as mentioned in Section 4.4.2. However, the similarity fails to hold when heterogeneity is present in the zeta potential of channel walls or when an external pressure is applied, where flow recirculation may occur.^{34, 35, 77, 105}

4.4.4 Vorticity in Electroosmotic Flow

As pointed in previous section that $\nabla \times \vec{V} = 0$ is valid everywhere in EOF, implying vorticity is zero throughout the electroosmotic flow (except inside EDL). This is true not only to EOF in the wavy channel, but to EOF in any shape of channels. To explain this, let's consider a 2D, incompressible, barotropic flow of fluid with constant viscosity and permittivity, and subject to a slipping wall ($\vec{V}_{wall} = V_{wall} \hat{t}$). The momentum equation for EOF is

$$\frac{D\vec{V}}{Dt} = -\frac{1}{\rho} \nabla p + \nu \nabla^2 \vec{V} - \frac{\rho_e}{\rho} \nabla \phi \quad (4-51)$$

At the channel surface, the momentum equation in tangential direction is rewritten as

following, where $\omega = \frac{\partial V_{wall}}{\partial \hat{n}}$ is the vorticity at the surface.

$$-\nu \frac{\partial \omega}{\partial \hat{n}} \Big|_{wall} = \underbrace{\frac{\partial V_{wall}}{\partial t}}_{\text{acceleration of surface}} \Big|_{wall} + \underbrace{\frac{1}{\rho} \frac{\partial p}{\partial \hat{t}}}_{\text{wall pressure gradient}} \Big|_{wall} + \underbrace{\frac{\rho_e}{\rho} \frac{\partial \phi}{\partial \hat{t}}}_{\text{wall electric field}} \Big|_{wall} + \underbrace{V_{wall} \frac{\partial V_{wall}}{\partial \hat{t}}}_{\text{velocity gradient of surface}} \Big|_{wall} \quad (4-52)$$

The formula implies that vorticity that diffuses toward the EOF at the channels comes from

- the acceleration of the wall,
- the tangential pressure gradients along the boundary,
- the tangential electric field along the boundary, or
- the tangential velocity gradient of the boundary.

The first and the last sources are zero when the boundary is stationary in most situations, such as the EOF in the wavy channel discussed in this work. Hence, vorticity is generated at the surface by the induced pressure gradient and the wall electric field, and they generate equal amount but opposite tone of vorticity, resulting the net production of vorticity zero at the channel surface. Hence the vorticity inside the channel remains zero.

When the boundary is moving, the vorticity generation at the channel wall surface has to include the tangential acceleration and the tangential velocity gradient. For example in the EOF with the effective slipping boundary condition, the Helmholtz-Smoluchowski velocity is assumed at the edge of the electric double layer, and the entire fluid is assumed electrically neutral ($\rho_e = 0$). The wall pressure gradient and the velocity gradient of boundary become the sources of vorticity in EOF. Again, their vorticity production cancels each other and zero vorticity enter into the EOF from the channel surface. As a result, vorticity is zero everywhere in the EOF.

4.4.5 Electroosmotic Flow with Pressure Gradients

The discussion in Sections 4.4.1-4.4.4 pertains to an electroosmosis-driven flow with no external pressure applied. When an external pressure drop is present, the resulting flow can be viewed as superposition of a Poiseuille flow and the EOF, since the governing equation in a creeping flow is a linear ordinary differential equation. Figure 4-9a shows the velocity profile of an EOF in a wavy channel of scaled width $h = 2.84$ and scaled wave amplitude $\alpha = 0.45$ while the velocity profile of the pressure driven flow in the same channel is illustrated in Figure 4-9b.

Note that the EOF is from right to the left based on the boundary condition defined in Equation 4-6 whereas the pressure-driven flow is from the left to the right based on the boundary condition defined in Equation 4-5. The ratio of the pressure drop (Figure 4-9b) to the electric potential difference (Figure 4-9a) is $|K| = 2$. A negative K value indicates that one of these two flows is reversed and they move in the same direction. The superposition of the EOF and the Poiseuille flow in the same direction results in a combined flow, that is shown in Figure 4-9c for the velocity profile and in Figure 4-9d for the streamline. The combined flow possesses a quadratic velocity profile, which is different from the EOF. The combined flow also possesses finite velocity at the wall, which is different from no slip condition in the pressure driven flow.

It is interesting to observe the presence of recirculation when the EOF is superposed in the opposition direction with the pressure driven flow ($K = 2$), as shown in Figures 4-9e and 4-9f. The velocity profile in Figure 4-9e indicates the presence of a backflow, while the streamline pattern in Figure 4-9f shows the presence of recirculation region where two series of eddies are observed at the top of the trough area and the bottom of the neck area of the wavy channel respectively. This is different from the flow separation in a typical creeping Couette flow or Poiseuille flow in wavy channels that occurs in the bottom of trough area due to the adverse pressure gradient.^{91, 95, 97}

The formation of the recirculation region in Figure 4-9f is the result of the interaction between the pressure driven flow and electroosmotic flow in channels of varying cross sections. As shown in Figure 4-9e, the superimposed flow experiences backflow at the center of the channel when the maximum velocity of the pressure driven flow exceeds the EOF velocity. Two separation bubbles can be easily identified in the flow. They form mainly as a result of

competition between the EOF and the pressure driven flow in the opposite direction. The specific pattern and size of the bubbles depend on the values of K , α , and h as discussed later.

Visual studies have also been carried out to verify the presence of the recirculation region as predicted by the solution, as shown in Figure 4-10. The experiment is performed in a microchannel in the poly(dimethylsiloxane) device fabricated by following the procedure in the Chapter 2. The channel is filled with water containing latex beads of 0.75-micron diameter (Polyscience, Inc.). The pressure gradient is provided by the difference (43.3 mm) in the solution level in reservoirs. Figure 4-10a shows the velocity profile corresponding to the case in Figure 4-9c. The velocity is calculated from two consequent images (with an interval of 33 milliseconds) acquired by a CCD camera. Commercial particle imaging velocimetry software (PIVview, PIVTEC GmbH) is used to generate the velocity field of the flow. Figure 4-10b shows the pathlines of beads generated by overlapping 60 consequent images, corresponding to the case in Figure 4-9f. The experimental result exhibits a qualitative agreement with the theoretical solution.

4.4.6 Onset of Recirculation

The onset of flow recirculation depends on the channel geometry and the magnitude of the applied pressure drop relative to the electrokinetic force. It is observed that when the applied pressure drop slightly exceeds a threshold value, a small isolated bubble forms half way between two walls near the neck region and the u-component velocity becomes slightly positive over a small region along the y -direction. Figure 4-11 shows the streamlines of the flow in a wavy channel with K at 0, 1.0, 1.1, 1.2, 1.25, 2, and 4.2 when $\alpha = 0.45$ and $h = 2.84$. No recirculation region is present when K is zero (Figure 4-11a). Recirculation appears in the channel when K reaches a threshold value. It starts to occur at the neck region (Figure 4-11c), and then form a separate bubble in the trough region (Figure 4-11d). As K increases further, the recirculation

region expands (Figure 4-11e), then shrinks (Figures 4-11f and 4-11g), and finally diminishes to the channel walls when the flow is completely dominated by the pressure-driven flow.

Since the combination of the pressure gradient and the electrokinetic force in the opposite direction will always produce a local maximum, u_{\max} , in the u -profile at the neck, the condition for which $u_{\max} = 0$ at $x = -\pi$ is taken as the onset of the recirculation flow. To compute u_{\max} for a given set of (K, α, h) , the velocity profile at $x = -\pi$ is computed at 10 locations in the y -direction. A polynomial fit for $u(y)$ is then obtained based on those 10 data. A preliminary location, y' , of the maximum u is identified. The velocities at five location near y' are computed using very small interval size and a much more refined polynomial fit is obtained for the velocity profile near y' . Subsequent determination of the true maximum velocity, u_{\max} , and its location, y_{\max} , contain very small interpolation error.

Figure 4-12 shows the velocity profiles at the neck as a function of K used in Figure 4-11. The data supports the conclusion that the onset of the recirculation bubbles starts when a flow opposite to EOF appears at the neck.

By keeping K constant, we also examine the effects of the channel geometry represented by the scaled wave amplitude (α) and the scaled channel width (h). When the gap between the top wall and the neck of the wavy bottom wall becomes small, i.e. either α becomes large or h becomes small, EOF dominates. Hence there is no backflow, and no recirculation exists in the flow. In contrast, when α becomes small or h becomes large the pressure flow dominates and recirculation occurs in the flow.

Figure 4-13a shows the geometric relationship between α and h required for the onset of recirculation at $K = 2$. The solid black line represents the physical boundary when the neck of the wavy bottom wall touches the top wall, $\alpha = h$. As a result, only the region below this line is

physically possible in terms of the channel geometry. The curve with circles splits entire parameter space into two zones: a recirculation zone below the curve and a recirculation-free zone between the curve and the solid line. The circles represent the data obtained from the solution. The curve starts from $(\alpha = 0, h = 2)$ and approaches to the physical boundary as h increases. The wavy channel of $\alpha = 0.45$ and $h = 2.84$ described in Figures 4-9e and 4-9f does fall in the recirculation zone, consistent with the result shown in Figure 4-13a.

Note that the intercept (h_0 value when $\alpha = 0$) of the curve corresponds to a channel of constant cross sectional area, in which the flow velocity at the centerline is zero due to the fact that the maximum velocity of a pressure flow ($u_{\max} = P_0 H^2 / (8\mu L)$) is equal to the EOF velocity ($u_{eo} = \eta\Phi_0 / L$). Equating u_{\max} to u_{eo} results in $h_0 = \sqrt{8/K}$. This equation can be used as the starting point of the calculation for the K curves, which separates the recirculation zone from the recirculation-free zone for the given K value.

The exploded view of the K curve near the intercept is shown in the inset of Figure 4-13a. The solid line is based on the calculated velocity profile at the neck, while the dashed line is based on the velocity profile at the trough of the wavy channel. They coincide at $h = 2$, but the onset conditions of recirculation are slightly different, depending on the location and geometry of the channel. As shown in Figure 4-11c, flow recirculation is observed only at the neck, but not at the trough of the channel when $\alpha = 0.015$, $h = 2$ with $K = 2$. As a result, the diagrams in Figure 4-13 are generated by using flow reversal at the neck as the criteria of flow recirculation.

Figure 4-13b shows the dependence of the onset of flow recirculation on the applied forces represented by the dimensionless parameter K . When K is small, EOF dominates and it is difficult to have recirculation in the flow. When K is large, pressure flow dominates, recirculation easily occurs. The plot provides a means to determine the geometry and external

force requirement when recirculation is desirable. It also provides a convenient tool to determine whether flow recirculation occurs in a wavy channel.

4.4.7 Recirculation Pattern and Size

As expected, the pattern and size of recirculation region are dependent on the three dimensionless parameters, α , h , and K . The pattern of the recirculation region as a function of K is shown in Figure 4-11. Two recirculation modes are identified when there is flow recirculation in the wavy channel. As shown in Figures 4-11d and 4-11e, type I recirculation mode consists of two series of bubbles: one centered at the trough of the wavy channel and the other centered at the necks. The bubbles are located near the centerline of the channel. Type II recirculation mode is displayed in Figures 4-11f and 4-11g, also consisting of two series of bubbles. However, the bubble centered at the trough is close to the top plain wall whereas the bubble centered at the neck is close to the bottom wavy wall. Both bubbles are spindle shaped and they are separated by flow streams in the direction of pressure gradient and in the middle of the channel. Flows in the direction of EOF lie between the bubbles and the channels walls. Significant difference exists between the center streams in two types of recirculation: the center streams wind through bubbles in type I whereas they flow smoothly in type II.

The relationship between the size of recirculation region and the K value is plotted in Figure 4-14. The size is defined by the ratio of the area of recirculation region to the whole area of the wavy channel. The same geometry in Figure 4-11 is used and the flow patterns in Figure 4-11 are marked on the plot in Figure 4-14 with corresponding labels (a-g). As expected, the flow is recirculation-free when K is small. As K increases to 1.1, recirculation starts to occur. The bubbles rapidly expand as K increases until it reaches 1.25, at which the recirculation region reaches the maximum size, ~52% of the total channel area. The bubble slowly shrinks

afterwards. As K increases toward infinity, the bubble diminishes to the channel boundary and their size approximates asymptotically to zero.

Figure 4-15A shows the effect of the scaled wave amplitude (α) on the size of recirculation region in a wavy channel. The K value is set at 2 while h is fixed at 2.84. The result indicates that recirculation occurs when $\alpha < 1.31$, but flow becomes recirculation-free beyond the value. This result agrees with the discussion above on the onset of recirculation: recirculation occurs at small α values, but not at large α values. The maximum size of the recirculation region takes place when $\alpha = 1.08$. The streamline patterns corresponding to $\alpha = 0.31, 0.91, \text{ and } 1.19$ are shown in the insets of Figure 4-15A.

The effect of the scaled channel width (h) on the size of recirculation region is also studied (Figure 4-15B). The K value is set at 2 while α is fixed at 0.45. The flow is recirculation-free until $h = 2.0$. Bubbles rapidly enlarge as h increases, and reaches to the maximum size at $h = 2.2$. As h further increases, the size of recirculation region slowly decreases and drops asymptotically to zero.

4.5 Summary

Using the complex function and boundary integral formulation, an accurate method for obtaining 2D electroosmotic flow in a wavy channel is developed. Effective slipping boundary conditions are employed to decouple the electrostatic and hydrodynamic effects. Because of the flexibility of the boundary integral formulation, this method is shown to be an effective and more accurate alternative to the lubrication theory and perturbation method. Compared to the approximate solutions using the lubrication theory, the restriction of a slow change in the wall charge or geometry is removed in the present formulation so that the effects of arbitrary values of α and h can be investigated.

The solution indicates that the electric field strength changes along the wall surface as a result of the variation of the channel wall. A similarity exists between the flow velocity and the electric field; this verifies the calculation result that suggests the EOF is irrotational in a wavy channel. Unlike a creeping flow driven by a pressure gradient or a Couette flow, an EOF contains no recirculation region even with a wall of large wave amplitude.

The EOF in a wavy channel can result in recirculation regions when a pressure gradient in the opposite direction is added. The prediction by the analytical solution is confirmed by the presence of recirculation bubbles observed in experiments. The result in a microfabricated device agrees with the similar observation in a capillary recently reported and studied using a perturbation method.¹⁰⁵

The onset conditions for recirculation in a wavy channel are found to depend on one dimensionless parameter related to the external forces (K) and two dimensionless parameters related to the wavy channel geometry (α and h). The results are summarized in a diagram relating recirculation to K , α , and h . The pattern and size of the recirculation region are also found to depend on these three dimensionless parameters. This work on the sinusoidal wavy channel is expected to help understand the interaction between pressure and electrokinetic forces in an irregular geometry flow, including the flow in ridged channels.

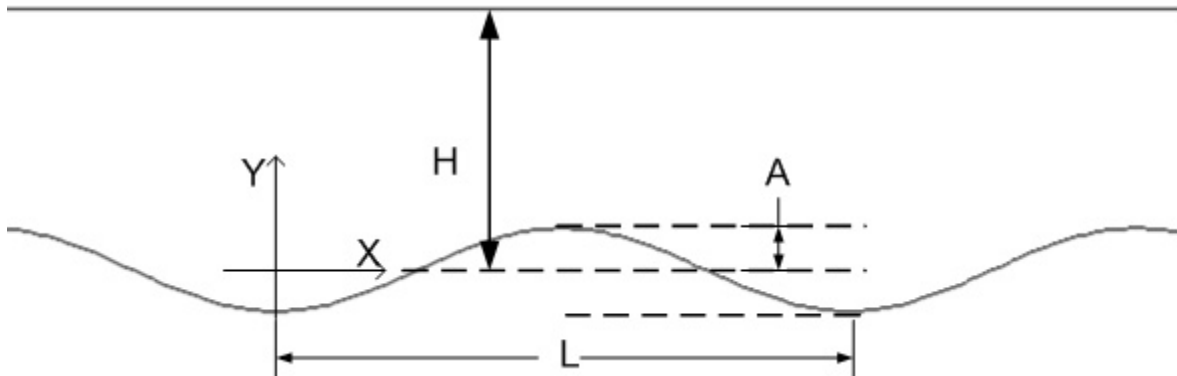


Figure 4-1. Two-dimensional wavy channel between a flat plate at the top and a sinusoidal plate at the bottom. Also indicated are the coordinate system and the channel geometries, including wavelength L , wave amplitude A , and average channel width H .

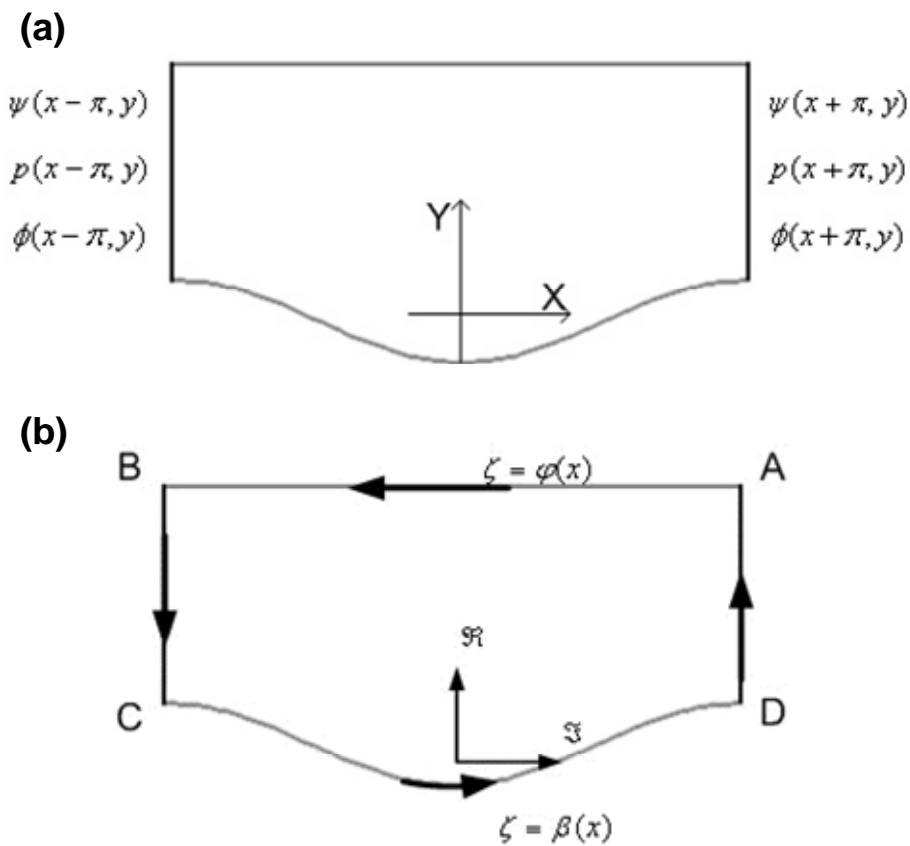


Figure 4-2. Boundary conditions and contour path used in the analytical solution. (a) One period of a wavy channel with boundary condition at both ends. (b) Contour path for the Cauchy integral over one period of a wavy channel.

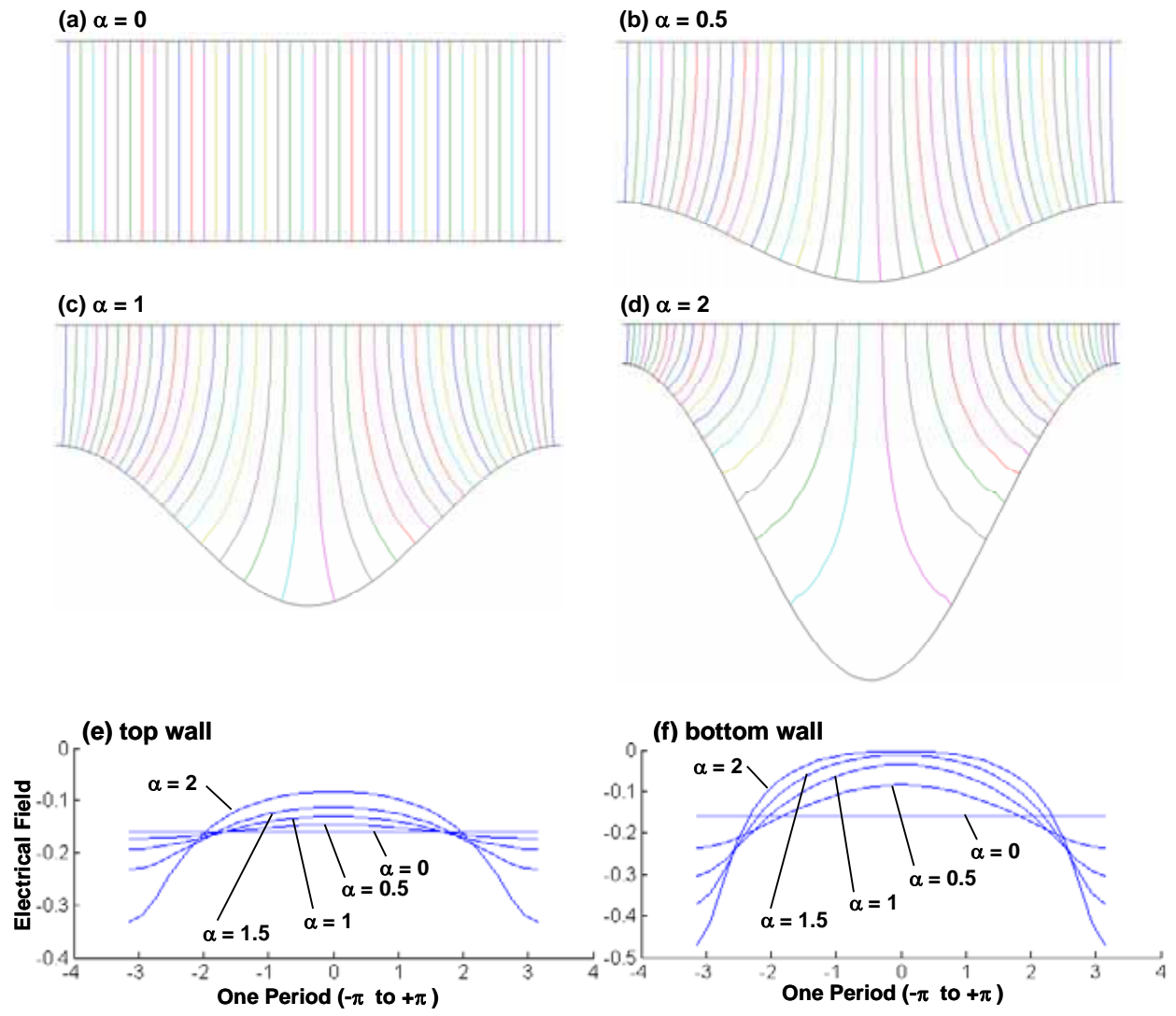


Figure 4-3. Effect of the scaled wave amplitude on the electric potential distribution in a wavy channel ($K=0$). (a-d) Equipotential line patterns. The scaled wave amplitude, α , changes from 0 to 2 while the channel width, h , is fixed at 2.5. (e-f) The electric field strength at the top flat wall (e) and the bottom wavy wall (f) at each wave amplitude. For clarity, data points on the lines are removed.

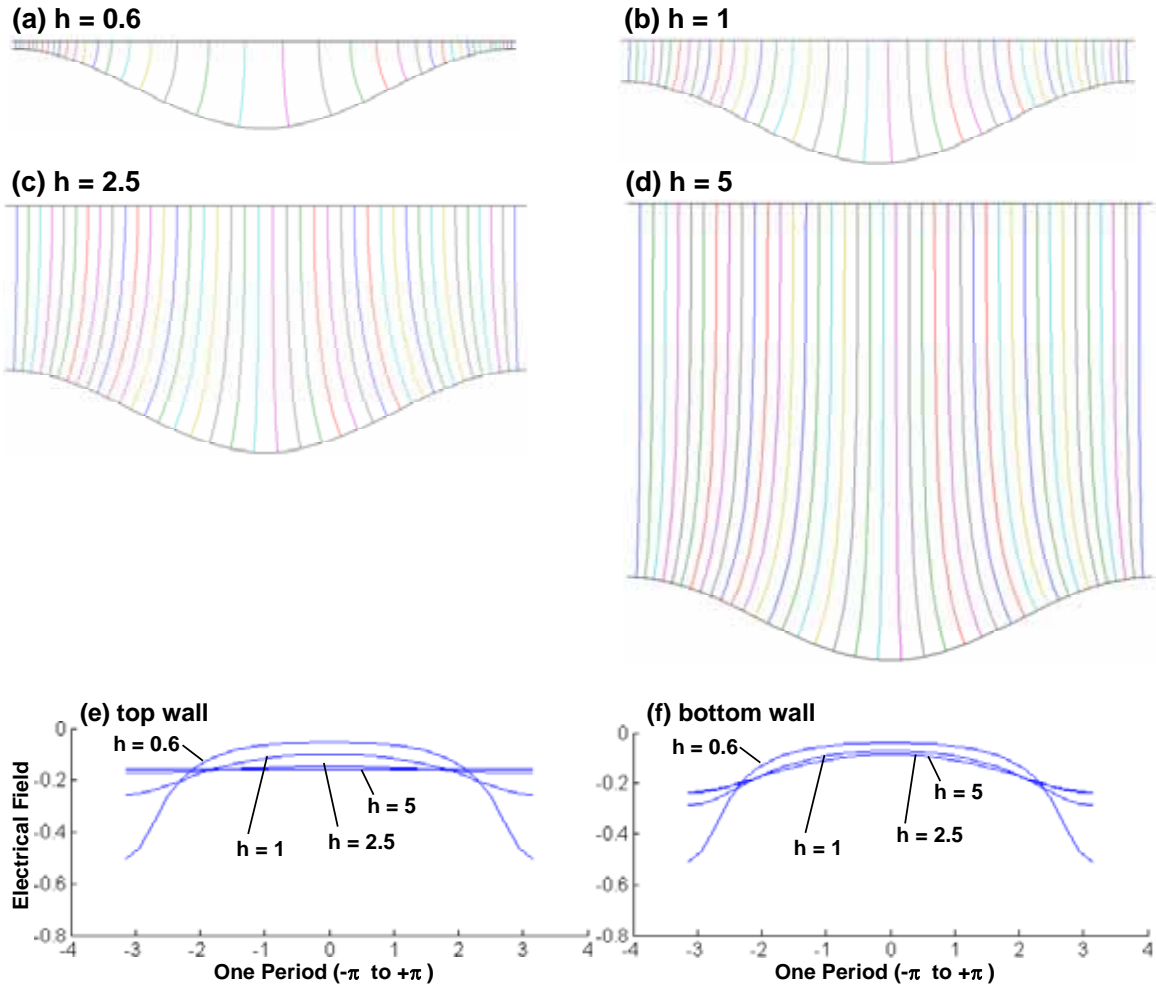


Figure 4-4. Effect of the channel width on the electrical potential distribution in a wavy channel. (a-d) Equipotential line patterns. The channel width, h , changes from 0.6 to 5 while the wave amplitude, α , is fixed at 0.5. (e-f) The electric field strength at the top flat wall (e) and the bottom wavy wall (f) at each channel width. For clarity, data points on the lines are removed.

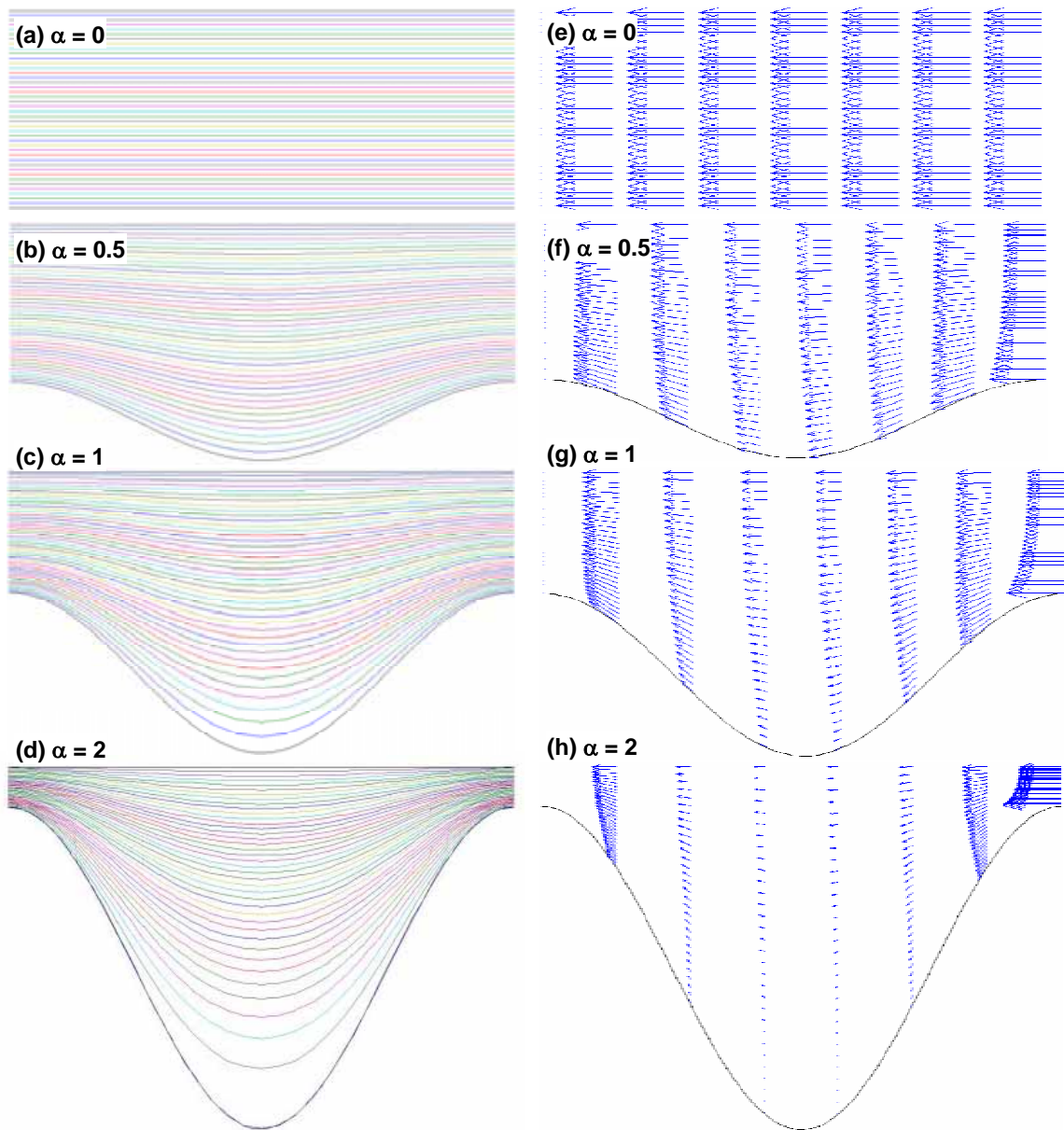


Figure 4-5. Effect of the scaled wave amplitude on the velocity field in a wavy channel ($K=0$). (a-d) The streamline patterns of EOF. The scaled wave amplitude, α , changes from 0 to 2 while the channel width, h , is fixed at 2.5. (e-h) The velocity profiles of EOF corresponding to (a) to (d).

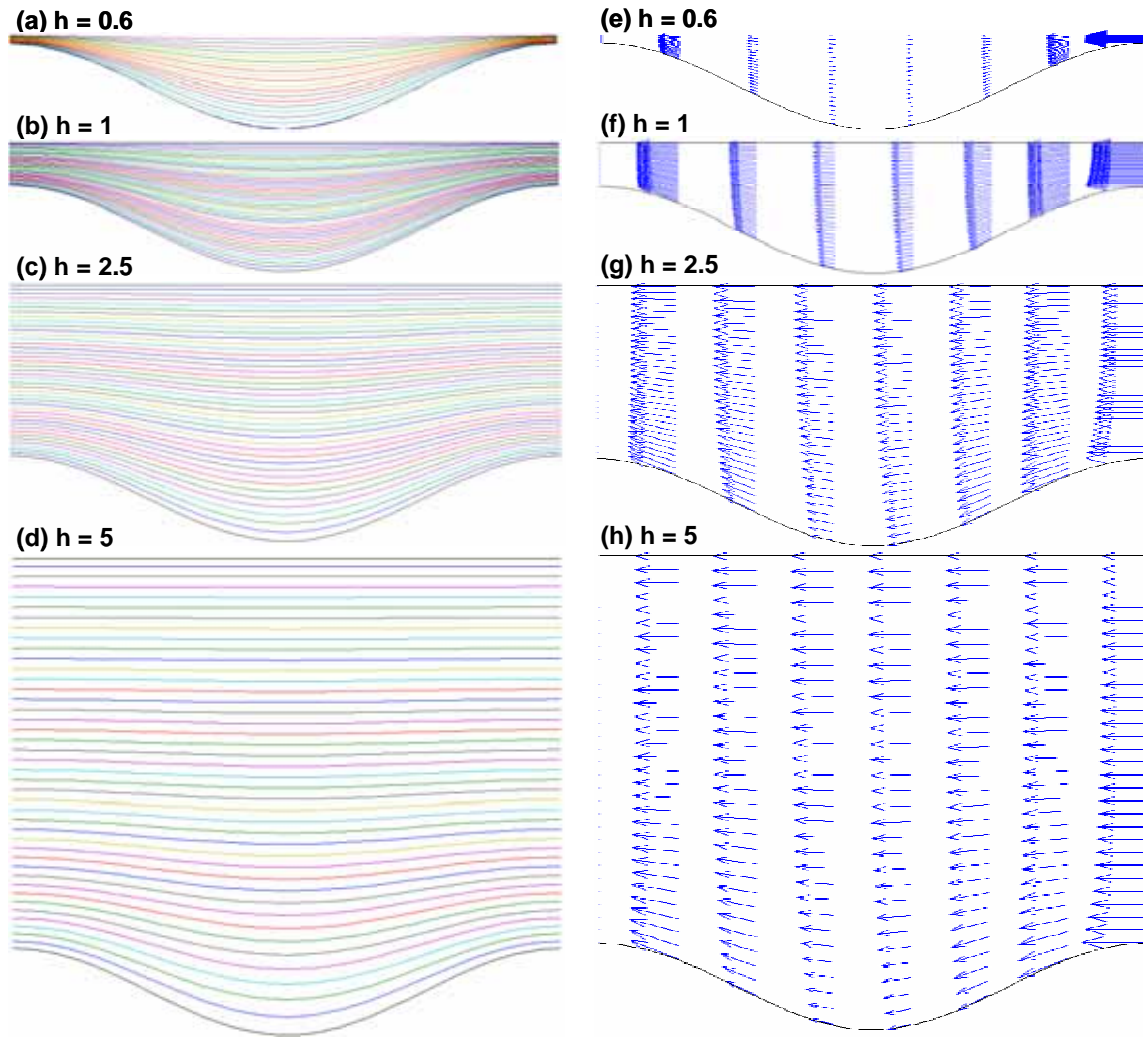


Figure 4-6. Effect of the scaled channel width on the velocity field in a wavy channel ($K=0$). (a-d) The streamline patterns of EOF. The scaled channel width, h , changes from 0.6 to 5 while the scaled wave amplitude, α , is fixed at 0.5. (e-h) The velocity profiles of EOF corresponding to (a-d).

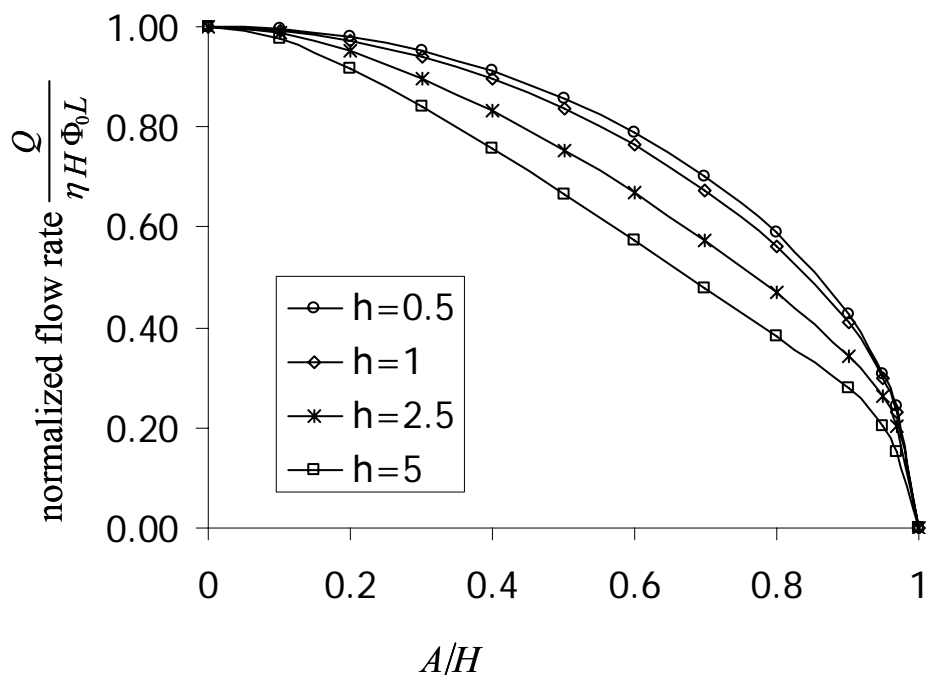


Figure 4-7. Flow rate as a function of the ratio of wave amplitude to channel width. Flow rates are normalized against the one in a smooth channel with the same channel width. The channels width, h , ranges from 0.5 to 5.

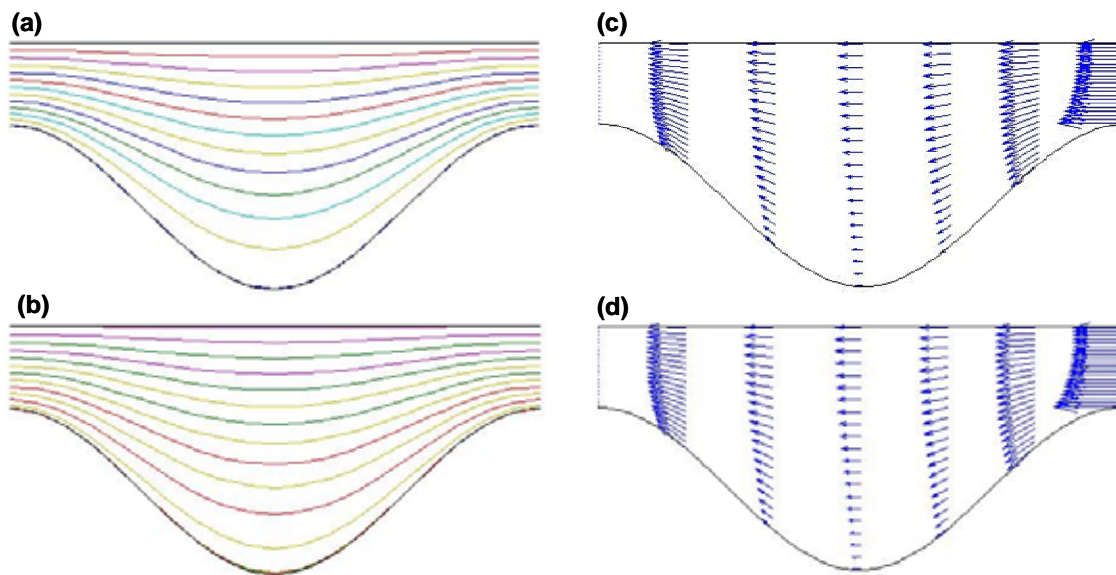


Figure 4-8. Similarity between the electric field and the velocity field of an EOF in a microchannel of $h = 2$ and $\alpha = 1$, as demonstrated in (a) streamlines, (b) electric field lines, (c) velocity vectors; and (d) electric field vectors.

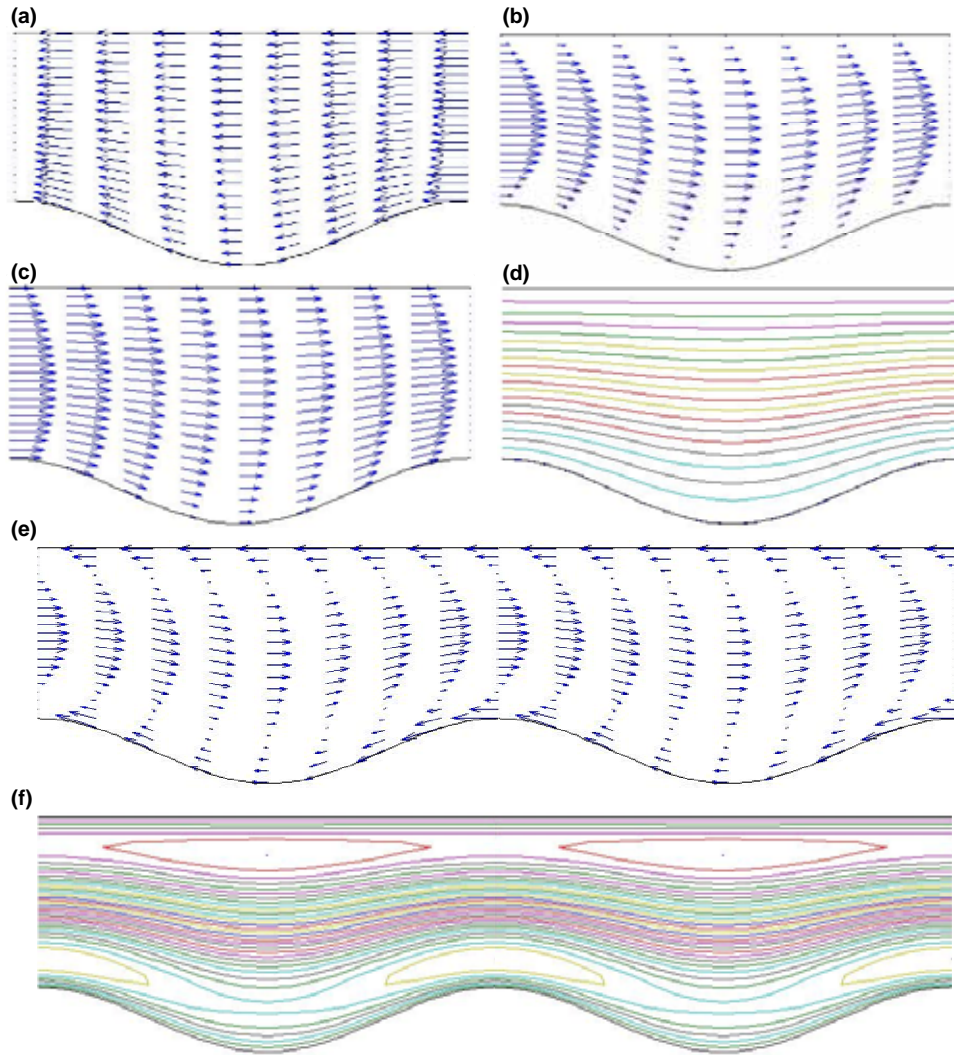


Figure 4-9. Combined flow driven by electroosmosis and pressure. (a) The velocity profile of an EOF in a wavy channel with channel width $h = 2.84$ and wave amplitude $\alpha = 0.45$. (b) The velocity profile of a pressure driven flow in the same channel as in (a). (c-d) The velocity profile (c) and the streamline pattern (d) of a combined flow driven by electroosmosis and pressure in the same direction. The ratio of the pressure drop to the electric potential difference (K , as defined in the text) is 2. (e-f) The velocity profile (e) and the streamline pattern (f) of a combined flow driven by electroosmosis and pressure in the opposite direction; K is 2.

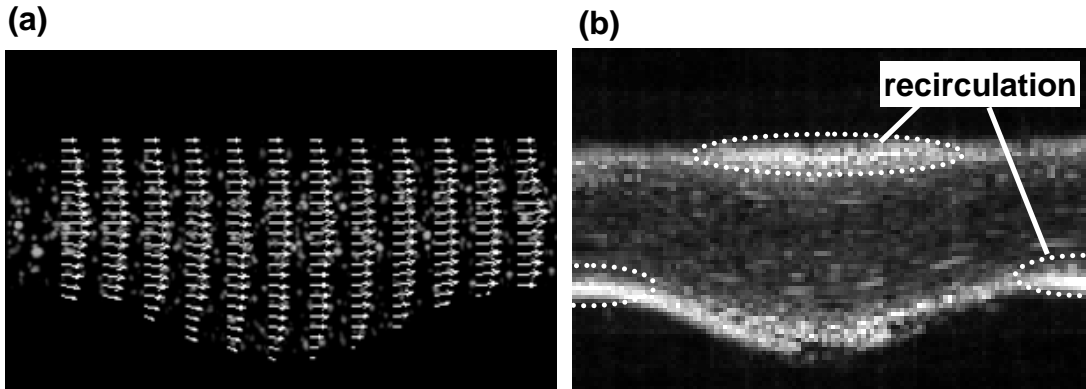


Figure 4-10. Images of microbead flow in a wavy channel in a microfabricated PDMS device. The images are inverted; beads are represented by white spots. The channel width is $34.5 \mu\text{m}$, the depth is $95 \mu\text{m}$, the wavelength is $76.4 \mu\text{m}$, and the wave amplitude is $5.5 \mu\text{m}$. The flow is driven by both pressure and electroosmosis. The hydrostatic pressure results from the solution level between two reservoirs (43.4 mm) while the electric field strength is 800 V/cm . (a) Image of the flow overlapped with velocity vectors that are calculated using velocimetry software. The pressure is applied in the same direction of the EOF. (b) Pathlines of beads obtained by overlapping 60 consecutive images. EOF is in the opposite direction of the pressure gradient. The recirculation flow regions are indicated by denser bead population (more white spots).

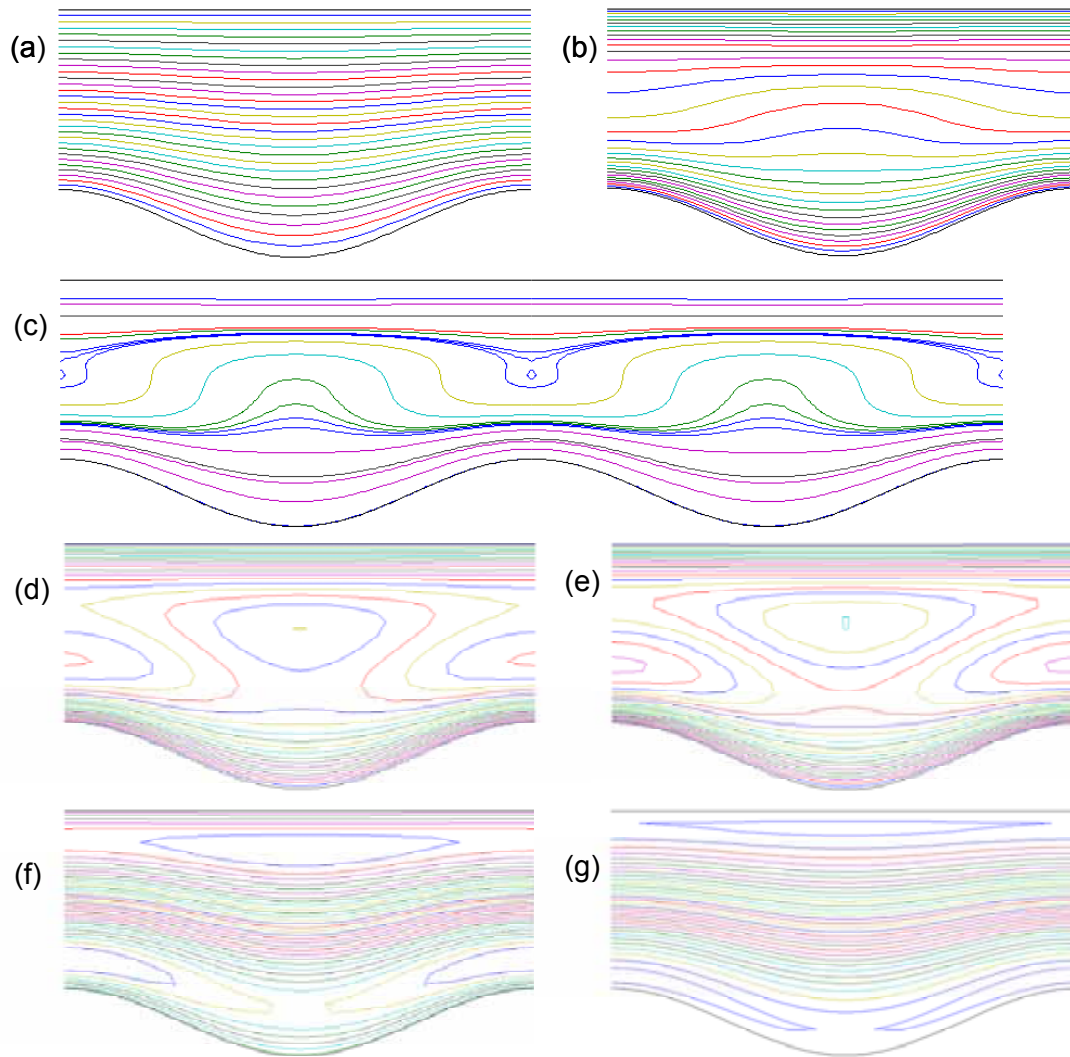


Figure 4-11. Streamline patterns of fluid flows in wavy channels. The scaled channel width (h) = 2.84, and the scaled wave amplitude (α) = 0.45. The ratio of the pressure force to the electrokinetic force, $K = 0$ (a); $K = 1.0$ (b); $K = 1.1$ (c); $K = 1.2$ (d); $K = 1.25$ (e); $K = 2$ (f); and $K = 4.2$ (g). Two periods are plotted for (c) to show the onset of recirculation in the neck region, but not in the trough region yet.

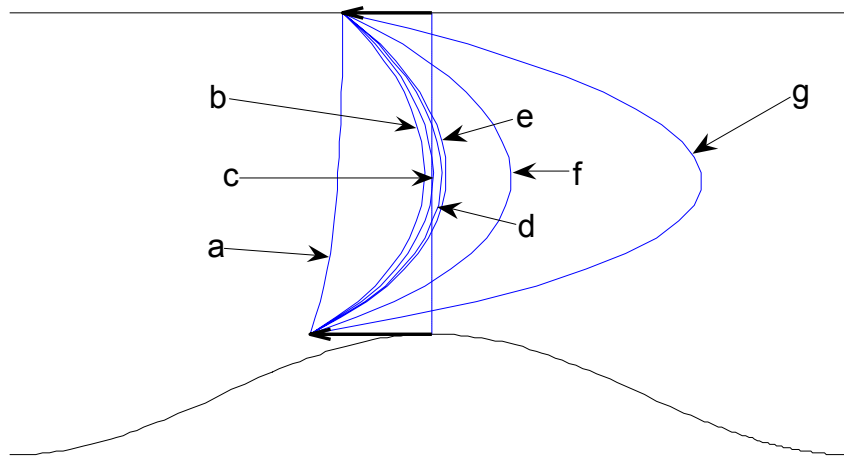


Figure 4-12. Velocity profiles at the neck as a function of K . The wavy channel is the same as in Figure 4-11, with $h = 2.84$ and $\alpha = 0.45$. The labels (a-g) correspond to the flow patterns in Figure 4-11, with $K = 0$ (a); $K = 1$ (b); $K = 1.1$ (c); $K = 1.2$ (d); $K = 1.25$ (e); $K = 2$ (f); and $K = 4.2$ (g). The profile c at $K = 1.1$ is when the recirculation starts with a reversal flow.

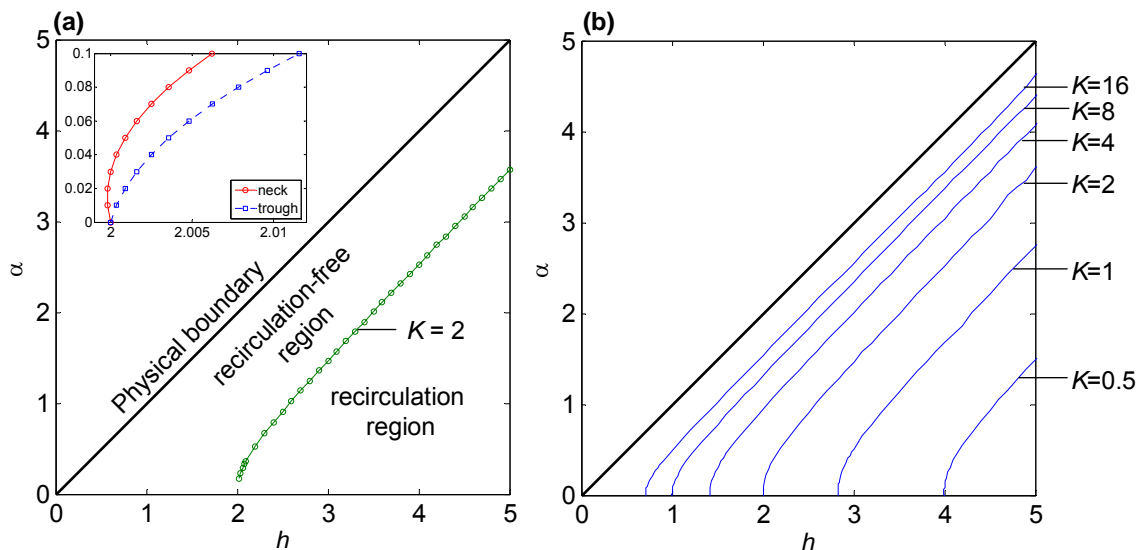


Figure 4-13. Flow recirculation diagram for various scaled wave amplitude (α), scaled channel width (h), and the ratio of pressure force to electrokinetic force (K). (a) Recirculation region, recirculation-free region, and region for impossible channel geometry are indicated when $K = 2$. (inset) The exploded view of the curves near the intercept. The solid line is based on the calculated velocity profile at the neck, while the dashed line is based on the velocity profile at the trough of the wavy channel. (b) Diagram with various K values as indicated. The bold solid line represents the physical boundary. Other curves represent the approximate boundary lines of recirculation zone and recirculation-free zone.

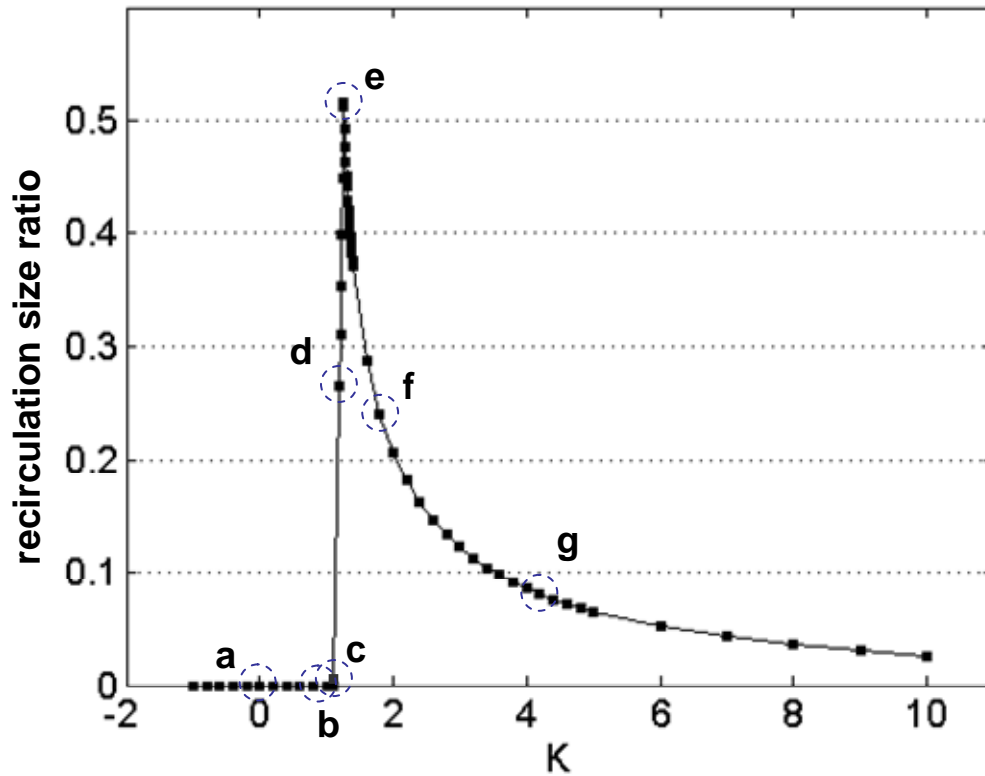


Figure 4-14. Size of recirculation region as a function of K . The size is represented by the ratio of area of recirculation region to the total area of the wavy channel. The wavy channel is the same as in Figure 11, with $h = 2.84$ and $\alpha = 0.45$. The labels (a-g) correspond to the flow patterns in Figure 11, with $K = 0$ (a); $K = 1$ (b); $K = 1.1$ (c); $K = 1.2$ (d); $K = 1.25$ (e); $K = 2$ (f); and $K = 4.2$ (g).

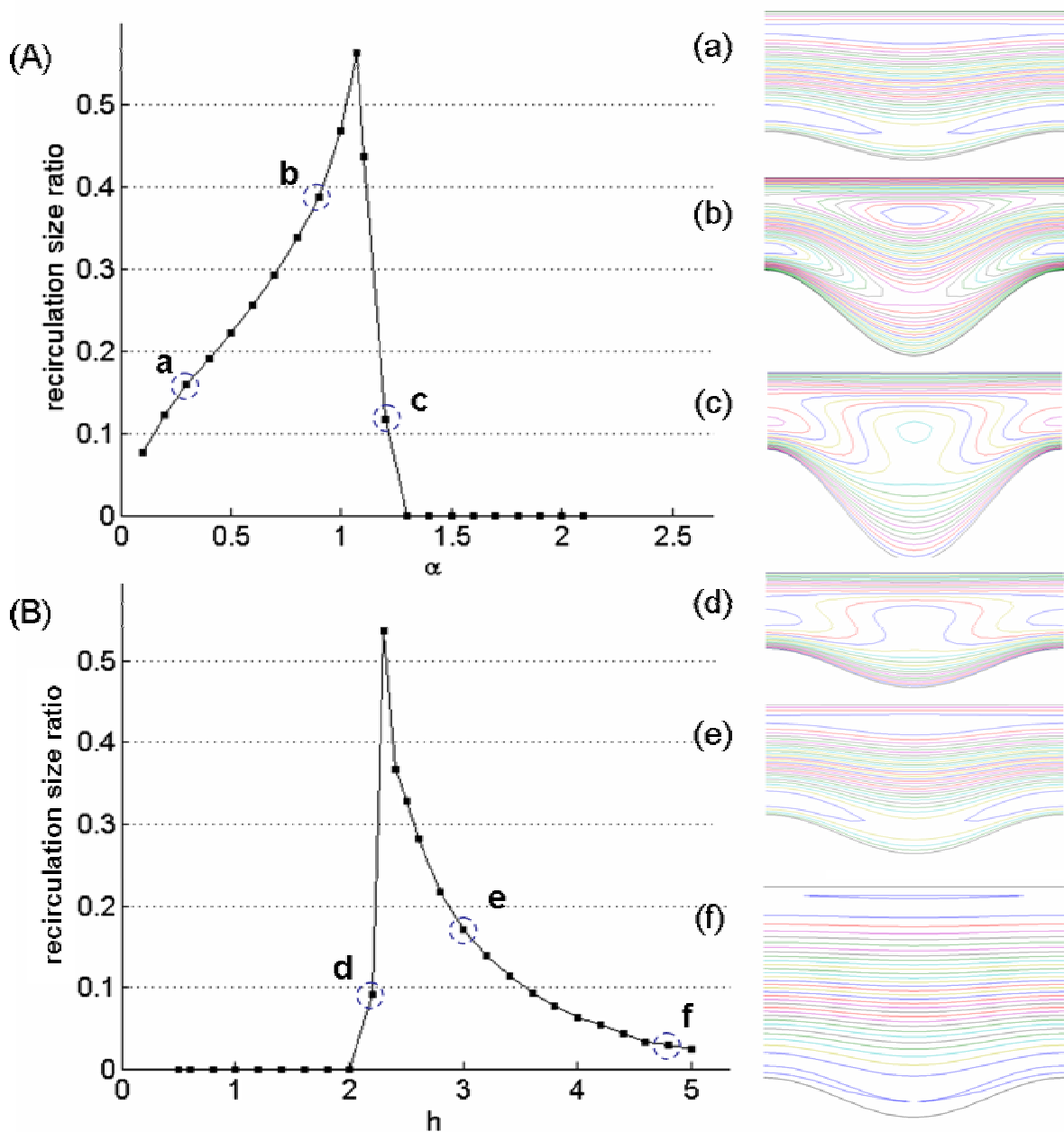


Figure 4-15. Size of recirculation region as a function of α and h . (A) The size of recirculation region as a function of the scaled wave amplitude, α . The K value is fixed at 2 while $h = 2.84$. The streamline patterns of fluid flows in the wavy channel are shown in the inset with $\alpha = 0.31$ (a), 0.91 (b), and 1.19 (c). (B) The size of recirculation region as a function of the scaled channel width, h . The K value is fixed at 2 while $\alpha = 0.45$. The streamline patterns of fluid flows in the wavy channel are shown in the inset with $h = 2.1$ (d), 3.0 (e), and 4.8 (f).

CHAPTER 5 PULSED RECIRCULATION MIXER

5.1 Introduction

As discussed in Chapter 4, flow recirculation is induced when a pressure drop and an electric potential difference are imposed in opposite directions on a fluid flow in a wavy channel. It's found that the recirculation is due to the competence of electrokinetic force and pressure force in the flow, and strong flow recirculation is obtained in the fluid flow when their magnitudes are comparable, or the dimensionless parameters related to forces (K , the ratio of the pressure force to the electrokinetic body force) is in certain range related to the channel geometry.

Similar recirculation phenomenon is observed in a ridged channel, which also has a varying cross section. By properly adjusting the external forces, flow recirculation is illustrated in a ridged channel by the traces of micro particles that seeded in the fluid flow (Figure 5-1). Note that recirculation in the ridged channel also depends on channel geometries and the forces, like the case in a wavy channel.

This phenomenon has a promising potential in enhancing the fluid mixing in microfluidic systems. A micro mixer, referred hereafter as pulsed recirculation mixer (PRM), utilizes flow recirculation as described in this chapter. The mixing mechanism is discussed and validated using CFD simulations. Fluid mixing experiments are also conducted in a prototype PRM to verify the simulation findings.

The outline of this chapter is as follows. The characteristics of flow recirculation in ridged channels are first discussed and investigated using commercial CFD simulation package. The simulation results are verified by experiments of seeded fluid flow in ridged channels. A mixer based on recirculation is presented and its mixing scheme is discussed. Following numerical

validation of the mixing performance of the mixer by CFD simulation, experiment of fluid mixing in a prototype PRM are carried out. Chapter 5 concludes with a summary of the proposed novel mixer.

5.2 Recirculation in Ridged Channels

With the theoretical and experimental analysis of flow in a 2D wavy channel, flow recirculation is expected in a 3D ridged channel under similar conditions, like the one in Figure 5-1. To investigate the flow recirculation in the ridged channels, computational fluid dynamics simulations are first performed using commercial CFD software, CFD-ACE+, before further experiments are carried out with the ridged channels.

5.2.1 Validation of CFD-ACE+

CFD-ACE+ is a CFD and multi-physics simulation package developed by ESI group for simulation of a wide range of applications, including electroosmosis. It is supported by a set of pre-processing and post-processing tools. CFD-GEOM generates general geometries (either 2D or 3D) and the meshes for CFD-ACE+. CFD-MICROMESH is an automated tool for 3D geometries modeling and meshes generation, primarily for the needs of MEMS applications. Based on the 2D mask layouts and the deposition/etching process parameters, CFD-MICROMESH is capable of simulating the fabrication process, creating a model for the resulted geometries, and at the same time generated meshes as specified by user. CFD-VIEW is a post-processing tool for analyzing simulation results from CFD-ACE+.

Before proceeding to simulate flow in the ridged channel with CFD-ACE+, a quick validation is conducted to verify its capability in simulating electroosmosis in microchannels. Wavy channel of width of 34.5 micron, wave amplitude of 5.5 micron, and wavelength of 76.4 micron is generated using CFD-GEOM. An opposite pair of pressure gradient and electric field is applied on the model, which is solved by CFD-ACE+. Flow recirculation is predicted in the

wavy channel (Figure 5-2) from the streamline plot and the velocity profile, and this agrees very well with the results from the analytical solution developed in Chapter 4. In both cases, the dimensionless parameter K is 2.

Further comparison are made between the simulated stream function and electric potential data from CFD-ACE+ and the calculated data from the analytical solution. Electric potential values at 122 locations inside the wavy channel are extracted from the simulated flow, and then normalized to be in the range of 0 to 1. Another set of data are calculated at the same locations but using the analytical solution. To compare the two sets of electric potential data, Figure 5-3a is generated with the pair of simulated and calculated data as the x and y coordinates, respectively. Similarly, Figure 5-3b is generated based on the stream function data from the CFD simulation and the analytical solution. The near perfect linear relation in both plots suggests the good match between these two solutions, hence CFD-ACE+ is capable of simulating electroosmosis and yielding valid solution to flow recirculation in microchannels.

5.2.2 Modeling of Ridged Channels

A small portion of ridged channels is modeled using CFD-MICROMESH. Given the mask layout (Figure 5-4a), etching properties (isotropic) and desired etching depth (40 micron), the software simulates the etching process, generates the ridged channel model and subsequently meshes it with specified type of meshing algorithm. Figure 5-4b shows the resulting simulation model. The geometry of the ridge structure, same as the ridged channel from which the image (Figure 5-1) is acquired. The model, containing 11 ridge structures, has 907,889 cells (prisms and hexahedra) and 738,236 nodes. The typical length scale of an average cell structure is about 1 micron.

The fluid properties and the boundary conditions, including the pressure and the electric potential at both ends, and the zeta potential at the walls, are properly defined. Finite volume

method is chosen in the CFD-ACE+ software settings to solve the Navier-Stokes equation for the flow and the Poisson's equation for the electric field in the channel. Algebraic Multigrid Solver (AMG) is elected in solving the linear equations for its advantage in solving unstructured meshing. A maximum of 1000 iteration was carried out to ensure the convergence of solution, unless a 10^{-4} order of reduction in the residue is met or the absolute value of the residue reaches 10^{-18} .

5.2.3 Poiseuille Flow in Ridged Channels

The experiment in Chapter 3 has shown that a segment of ridged channels can achieve a comparable mixing performance to the staggered herringbone mixer. With the model illustrated in Figure 5-4, CFD-ACE+ is employed to quantitatively evaluate the performance of the ridged channel mixer.

Two distinct streams, deionized water and a solution containing 0.1 mM specimen, are introduced into the ridged channel (Figure 5-5a) at the same flow rate. Each fills half of the cross section of the entrance. The diffusivity of specimen is set to be $3.3 \times 10^{-10} \text{ m}^2/\text{s}$. Without the ridge structures, specimen molecules gradually diffuse into water stream from their interface as the two fluids move through a regular channel (Figure 5-5b). Complete mixing is achieved when specimen diffusion reaches from the interface of the two streams to the other side of water stream and a uniform concentration (0.05 mM) is reached throughout of the channel cross section. The process, however, takes considerable amount of time as the molecular diffusion is generally very slow, especially for large molecules.

The ridged channel is able to increase the diffusion process by stretching and folding flows so that the distance for diffusion to reach becomes shorter and the interfacial area becomes larger. The mixing process in the channel is verified by inspecting the specimen distribution at the cross sections in CFD-VIEW (Figure 5-5c). In the cross sectional views, blue stream

represents DI water, red stream is for 0.1 mM specimen solution, and the mixture of the two streams appears white color. Also plotted are the contour lines calculated from the specimen concentration. Comparing the contour lines at the entrance (i) to exit (iv) of the channel, it's evidential that the flow has a clockwise rotating motion along the axis of the channel. This agrees to the experimental observation by deconvolution microscopy presented in Chapter 3. Because of this transversal motion, flow is stretched in the ridged channel. As a result, the segregated streams become thinner and their interfacial area becomes larger. Compared to the diffusion process in a regular channel (Figure 5-5d), the mixing of two streams is thus improved by the ridge structures, as fewer contour lines are observed at the exit of the ridged channel.

To quantify the mixing effectiveness as a function of travel distance in the ridged channel, the variation of specimen concentration at cross sections and a segment of regular channel are calculated and plotted in Figure 5-6A. δ_0 is the variance of specimen concentration at the entrance. At cross sections further downstream, lower concentration variance is achieved, indicating a thorough mixing of two streams. For example, when $Pe = 450$, the variation of specimen concentration reduces to 5.9 nM at the exit of the ridged channel. In comparison, without the ridge structures, the variation at the exit of a segment of regular channel of same length only drops down to 23 nM. To define the mixing improvement by the ridged channel, we define amplification of mixing as follows,

$$\text{amplification of mixing} = \delta_{reg} / \delta_{rc}$$

where δ_{rc} is the variation of concentration at the exit of a segment of ridged channel and δ_{reg} is the variation at the exit of segment of regular channel of same length. Hence, the segment of ridged channel delivers a roughly 4-fold mixing amplification to flows at $Pe = 450$. The amplification of mixing of the segment of ridged channel containing 11 ridges is plotted as a

function of $\ln(Pe)$ in Figure 5-6B. A linear relation is found between the amplification and the logarithm of Peclet number of flow. As the Peclet number increases, the ridged channel becomes less effective in fluid mixing. This can be explained by that a flow with a larger Peclet number becomes more dominated by the streamwise convection, and the mixing effect from flow twisting becomes negligible.

5.2.4 Flow Recirculation Intensity

To induce flow recirculation, pressure and electric field are simultaneously imposed on the ridged channel model. In the simulation, the pressure gradient is applied by fixing the pressure at inlet zero and imposing a finite pressure, P , at the outlet, so that the pressure flow is from right to left in the top view, as illustrated in Figure 5-7a. The electric field is imposed by setting a finite electric potential, V , on the inlet of ridged channel model, while keeping the outlet grounded all the time. The resulting EOF in the channel is from left to right in the top view of the flow (Figure 5-7b). In the simulation, the electroosmotic mobility is set as $4.8 \times 10^{-8} \text{ m}^2/\text{s}$.

CFD-VIEW is used to analyze the flow field and visualize the calculated streaklines in the flow. Particle streaks were calculated from the simulated flow field. A total of 141 streaklines are generated in the flow, each of which represents the trajectory of a massless particle travels with the flow. The particles are released from an array of locations near the ridge structure (Figure 5-4c). The streaklines are calculated by connecting 500 segments of 1-millisecond travel distance.

Figure 5-7 shows the simulated trajectories and flow velocity profiles in a Poiseuille flow and an electroosmotic flow in the ridged channel. Quadratic velocity profile is identified in the pressure driven flow, so are the front of the streaklines. In the EOF, the velocity profile has a much more uniform profile, so that all the particles travel about equal distance with the same time lapse. No flow recirculation is observed in both flows. Similar to what we predicted in a

flow in a 2D wavy channel, the creeping electroosmotic/Poiseuille flow in a slow varying channel doesn't have any backflows, hence no flow recirculation occurs. However in case both pressure and electric field are imposed simultaneously on the fluid in the ridged channel, flow recirculation takes place around the ridge structures.

The flow recirculation is expected to be related to the ratio of electrokinetic force and the pressure force in the flow. Inherited from the study of recirculation in 2D wavy channel, the dimensionless parameter $K = P_0 L^2 / (4\pi^2 \rho \nu \eta \Phi_0)$ (Equation 4-32), represents the ratio of imposed pressure drop to electric potential difference on the fluid in the ridged channel. K is zero when zero pressure drop is applied, and the electroosmotic flow prevails; K becomes infinity in case that zero electric field is imposed on the fluid flow, hence the pressure flow dominates. With the combination of different P and V , a total of 18 flows of different K are simulated, and the boundary conditions are summarized in Table 5-1.

Figure 5-8 illustrates the streaklines in the ridged channels of some cases listed in Table 5-1. It's clear that the variation of flow recirculation is similar to that observed in a wavy channel. In the two extreme cases (Figures 5-16a and 5-16g), flow recirculation is rarely observed from the streaklines. While in cases where K is a moderate number (Figures 5-16b to 5-16f), the circulating streaklines become obvious, implying the presence of flow recirculation. Based on the simulation results, with current ridged channel geometry, flow recirculation is significant when K is in the range from 1.8 to 20, and it reaches strongest state when K approximates 4.5, where the net flow rate is roughly about zero in the channel.

5.2.5 Experiment Validation

To validate the numerical predictions of flow recirculation in ridged channels, a set of experiments are conducted on the ridged channels. The fabrication and parameter of ridged

channels is described in Chapter 2. Deionized water seeded with submicron latex particles is pumped into a ridged channel, and an electric field is applied on the fluid opposite to the direction of the Poiseuille flow. Time-lapse images of the flow are acquired by a CCD camera, and are overlapped to obtain the pathlines of the micro-particles in the flow. The parameter K is adjusted by changing the amplitude of the imposed electric field.

Figure 5-9 shows the variation of recirculation with respect to K in experiment, which agrees fairly well to the numerical predictions (Figure 5-8). Strong recirculation is obtained in flows with parameter K roughly in the range in the neighborhood of 5.8. The recirculation becomes weak as K increases to a large value. It vanishes when K decreases to zero. The minor discrepancy between the CFD simulation and experiments may result from the deformation of channel prototype caused by fabrication, and/or the errors during the analysis.

5.3 Mixing by Recirculation

It has been validated both numerically and experimentally that the construction of ridge structures on channel walls can cause flow twisting and yield effective mixing. Similar to flow twisting, flow recirculation also results in stretching and folding of fluid in the ridged channel, and ought to have a potential to improve fluid mixing. In the remaining of this section, a mixing scheme utilizing flow recirculation is discussed in details.

It's already known that the addition of an electric field to the Poiseuille flow in a ridged channel leads to the occurrence of recirculation in the flow. To induce recirculation of proper intensity, the pair of forces in the fluid, namely electrokinetic force and the pressure force has to satisfy the requirement obtained in previous section. A continuous application of the electric field, however, will result in dead volume in the recirculation region in the flow, which doesn't help in fluid mixing. Hence a discrete signal, for example a square wave (Figure 5-10), should be applied for fluid mixing. As a result, an unsteady EOF is induced in the ridged channel.

5.3.1 Formulation of Unsteady EOF

Formulations of the equations of the motion of fluid flow in pulsed recirculation mixer is similar to that provided in Section 4.2, except the addition of the temporal term due to the application of a periodic electric field. The formulas include continuity equation, momentum equation and Poisson equation. After the application of the effective slip boundary condition and the normalization by

$$\begin{aligned}\bar{x}^* &= \bar{x}/L \\ \bar{V}^* &= \bar{V}L/(\eta\Phi_0) \\ t^* &= t/\tau \\ p^* &= p/P_0 \\ \phi^* &= \phi/\Phi_0\end{aligned}$$

The formulas become

$$\nabla^* \cdot \bar{V}^* = 0 \tag{5-1}$$

$$(\text{Re} \cdot \text{St}) \frac{\partial \bar{V}^*}{\partial t^*} + \text{Re} \bar{V}^* (\nabla^* \bar{V}^*) = -4\pi^2 K \nabla^* p^* + \nabla^{*2} \bar{V}^* \tag{5-2}$$

$$\nabla^{*2} \phi = 0 \tag{5-3}$$

In the formulas, \bar{x} , \bar{V} , t , p , ϕ are the position vector, velocity vector, time, pressure, and electric potential, and they are non-dimensionalized using P_0 , L , η , Φ_0 , τ , which are the characteristic applied pressure, the characteristic length scale of the ridged channel (the distance between the periodic ridge), the electroosmotic mobility at the boundary (defined in Equation 1-21), the characteristic applied electric potential, and the characteristic time scale (the period of the applied pulsed electric field), respectively. The Laplacian and the gradient operators are also normalized using L . K is the same dimensionless number defined in Equation 4-32, Re and St are the Reynolds and Strouhal numbers respectively, and defined as

$$Re = \eta\Phi_0/\nu \tag{5-4}$$

$$St = L^2 / \eta \Phi_0 \tau \quad (5-5)$$

As the Reynolds number is less than the order of unity in a typical EOF; the second term in the momentum equation can be dropped off. However, the Strouhal number, as the ratio of time scale of EOF to the period of the applied electric field can be large, making the temporal term in the momentum equation dominant.

5.3.2 Pulsed Recirculation

The application of a constant pressure and such a pulsed electric field results in a time periodic flow in the ridged channel. Each period consists of two phases: recirculation phase when the electric field is on, and feeding phase when the electric field is off. In the recirculation phase, recirculation occurs in the flow and the fluids in the ridged channel are homogenized due to the actuation; the mixer is active. While in the second phase, the flow restores to laminar and thus the mixer is inactive. During the feeding phase, the mixed fluids are flushed out of the ridged channel, and unmixed fluids are fed into the mixer.

The mixing is related to the manner that electric field is applied, namely the magnitude of electric field, the oscillation frequency, the wave form and the duty cycle. The optimization of mixer is not performed in this work, and only guidelines are discussed here. In general the following operation conditions are desired in order to obtain an optimal mixing.

Strong recirculation intensity. The stronger the recirculation, the more effective the mixer is. Based on the numerical study of flow recirculation in the ridged channel, the intensity of recirculation depends on the ratio of the external forces imposed on the fluid. The amplitude of the electric signal should be adjusted such that in the recirculation phase, the resulting dimensionless parameter, K , is in the range where significant flow recirculation is obtained.

Sufficient recirculation time. The length of the recirculation phase ought to be long enough to ensure a fully development of the flow recirculation in the ridged channel and a

subsequent fully mixing by the recirculation. The time scale for the development of the flow recirculation is approximated by L^2/ν . To meet the criteria, the time period τ must satisfy $\tau > L^2/\nu$, or $Re \cdot St < 1$. Hence the temporal term can be removed from the momentum equation in Equation 5-2. Physically, this implies the transition from one phase to another is so quick that the flow is treated as a quasi-static flow, and the time only enters as a parameter to determine the phase.

No overfeeding. The amount of fluid pumped in feeding phase has to be carefully controlled that there is no overfed of fluid into the mixer. In the feeding phase of each cycle, unmixed fluids are fed into the mixer and an equal amount of mixed fluid are pushed out of mixer during the same period of time. It's desired to have the traveling distance of the incoming fluid in the feeding phase less than the length of the mixer. Given the hydraulic diameter of the ridged channel, D , and the average pressure gradient, P_0/L , the average velocity in the channel is approximated by $P_0 D^2 / 32 \rho \nu L$. Hence the time period has to satisfy $\tau < 32 \rho \nu L l / P D^2$, where l is streamwise length of the ridged channel where recirculation takes place.

5.4 Simulation of Pulsed Recirculation Mixer

Pulsed recirculation mixer utilizing recirculation in ridged channel is investigated numerically in this section. The micro mixer, called pulsed recirculation mixer, consists of a segment of ridged channel as shown in Figure 2-10. CFD simulations is carried out to demonstrate the mixing mechanism by flow recirculation and to evaluate its mixing performance. A mixer model, containing 10 consecutive ridge structures, is created using CFD-MICROMESH (Figure 5-11). The ridges have same geometry as the one used in the investigation of flow recirculation. The ridged channel has spatial period of 108 micron, and the

hydraulic diameter is 56 micron. A time varying electric field is imposed by applying a square wave electric potential at the outlet of the mixer and keeping the two inlets grounded.

The mixing process of two segregated streams is simulated. The incoming streams, deionized water and a 0.1 mM Rhodamine-B solution are pumped by an average pressure drop of 375 Pa/cm. The diffusion coefficient of Rhodamine-B is set as $3.6 \times 10^{-10} \text{ m}^2/\text{s}$. An electric field of mean strength of 272 V/cm is applied. Based on the definition of K in Equation 4-32, the corresponding parameter K is 9.1, roughly in the range where significant flow recirculation would be obtained. The electric field is alternating at the frequency of 1 Hz, and the duty cycle is 50%. Therefore in each cycle the duration for recirculation and feeding phases are 0.5 second each. The fluid density is set as 997 kg/m^3 , and the fluid kinetic viscosity is $1 \times 10^{-6} \text{ m}^2/\text{s}$ in the simulation. With the simulation configuration, the criteria for optimal mixing in Section 5.2 are all satisfied.

The initial state of simulation is set to be a steady flow where zero electric field is applied. At zero second, the pulsed signal is applied. The fluid flow in the PRM is calculated every 0.1 second by the CFD software, and the simulation stops at 6 seconds, the end of the 6th period. Simulation shows that flow recirculation occurs in the PRM at a frequency of 1 Hz, and the unsteady flow quickly settles at an oscillating pattern as the transient effect decays and becomes negligible.

Figure 5-12 shows the typical evolution of the distribution of Rhodamine-B at a cross section over one period. The cross section is located at $\sim 1 \text{ mm}$ after the merging of two streams, between the 4th and 5th ridge structures (section II in Figure 5-11). Contour lines of Rhodamine-B concentration are calculated and plotted at the cross section views for each frame. Also shown in Figure 5-12/ is the contour lines in a flow at the cross section of a regular channel (without

ridge structures). As expected, the contour lines are vertical in Figure 5-12I, indicating no flow stretching or folding, and hence the Rhodamine-B concentration has a large variation. While in ridged channel, the bending and rotating of the contour lines are clearly seen, implying twisting and recirculation inside the flow. Compared to the variance at the same location, PRM yields more homogenized solution, as less number of contour lines is present at the cross sectional views.

As the flow in the PRM settles at a stable pattern (Figure 5-13A), the time-averaged variance of Rhodamine-B concentration over one period is used in evaluating the mixing effectiveness of the PRM. The time-averaged concentration variation is calculated and plotted as a function of travel distance in the mixer (Figure 5-13B). Comparing the time-averaged variation in the PRM with the variation in a pressure driven flow in the same ridged channel, one may find the Rhodamine-B is evidently better mixed by the PRM due to the periodic occurrence of the recirculation.

Similar to the amplification of mixing defined in the study of fluid mixing in ridged channel, the amplification of mixing in PRM is defined as

amplification of mixing = $\delta_{reg} / \delta_{PRM}$,

where δ_{PRM} is the variation of concentration at the exit of the PRM and δ_{reg} is the variation at the exit of segment of regular channel of same length. Based on the simulation results, the PRM (with $K=9.1$) delivers a roughly 10-fold mixing amplification to the flow at $Pe=412$. While a segment of ridged channel of same length yields an amplification of mixing about 4. Clearly PRM improved fluid mixing better due to the periodic occurrence of recirculation. With optimized parameter settings, better mixing performance is possible from the PRM.

5.5 Experiment Validation of Pulsed Recirculation Mixer

5.5.1 Experiment Setup

A prototype PRM is connected to syringe pumps and placed on an invert microscope. A 0.1 mM Rhodamine-B solution and deionized water are pumped into the mixer at the same flow rate. A UV lamp is equipped to the microscope to illuminate the fluid flow. A high speed CCD camera (Hamamatsu, Japan) is used to acquire the fluorescent emission from the Rhodamine-B in the fluid. The intensity of fluorescence emission is proportional to the concentration of Rhodamine-B in the mixer. Hence one may evaluate the distribution of Rhodamine-B in the fluid in the mixer by examining the fluorescent images.

The pulse signal in the mixer is generated by an in-house LabView program and a high-voltage amplifier. The high-voltage is imposed to the fluid in the mixer via two electric wires that are glued to the printed carbonate ink electrodes.

The whole experiment setup, including the microscope and the fluid flow systems, are enclosed in a house-made opaque box, so that minimal environment light is present during image acquisition. The experiment setup is illustrated in Figure 5-14.

5.5.2 Experiment Results and Analysis

As predicted by the CFD simulation, the mixing performance of a pulsed recirculation mixer is significantly dependent on the applied electric field, namely, its frequency, duty cycle, and amplitude. Among the three operation parameters, the electric field amplitude plays the most critical role in determining the performance, and it is related to K , a dimensionless parameter defined as the ratio of the electric force to the pressure force on the fluid in the mixer. In this section, mixing experiments are conducted to verify the mixing performance by the pulsed recirculation mixer.

Figure 5-15a shows the PRM that is used in the experiment. 0.1 mM Rhodamine-B solution and deionized water are pumped into the mixer at a preset flow rate of 13 nL/s. An electric field is applied to the portion of mixer between the two carbonate electrodes. The average electric field strength is 1000 V/cm in the ridged channel, the duty cycle is 50%, and the frequency is 5 Hz. The resulting K is about 20. Figure 5-15b shows the top view of fluid flow in the ridged channel without application of the electric field, while Figure 5-15c shows the top view of the same mixer with the application of the pulsed electric field. The fluorescent images are taken at the end of recirculation phase. Comparing the two sets of top views, one may find a significant improvement on fluid mixing with the presence of flow recirculation in the ridged channel area.

Figure 5-16 shows the temporal evolution of Rhodamine-B distribution in the ridged channel in a period. The mixer is operated with the following operation parameters: $K=20$, 50% duty cycle and 1 Hz oscillation frequency. Consecutive fluorescent images are taken at the fifth ridge structure and the time lapse between two adjacent acquisitions is 0.2 second. The temporal variation of the Rhodamine-B concentration distribution in the mixer validates that recirculation is the mixing mechanism in the PRM. In each cycle the fluid is more mixed during the recirculation phase as the fluid appears more uniform; while it's less mixed during the feeding phase as unmixed fluid is driven into the mixer. For comparison purpose, the steady view of same mixer without the application of electric field is presented in Figure 5-16f. Comparing the uniformity of the fluid, it is evidential that the addition of a pulsed flow recirculation helps to enhance the fluid mixing in the ridged channel.

Intensity histogram profile is computed from the sequential images in Figure 5-16. To generate a histogram profile, intensities from an enclosed region in the fluorescent images of the

ridged channel are counted. The region contains a total of 21838 pixels, as indicated in Figure 5-16f. Figure 5-17 shows the temporal evolution of intensity histogram profile in the ridge channel in one cycle. One may observe the same trend that has been recognized in Figure 5-16. Without the presence of the recirculation, the histogram profiles possess two large separated peaks, representing the two distinct streams in the flow. During the recirculation phase when the mixer is active, the two peaks move toward each other while their heights grow higher, implying the two streams are better mixed. In the feeding phase when the mixer is inactive, the two peaks move back further apart and the heights go down, implying less mixing in the fluid.

The effect of K on the mixing performance of PRM is illustrated by Figure 5-18. By fixing the pressure drop and varying the amplitude of the pulsed electric field, the K varies from 60 to 12. As expected, the closer K approximates to the optimal value ($K=4.5$) that determined from the CFD simulation, the stronger the flow recirculation occurs in the ridged channel, and the better the mixing performance is. This observation qualitatively agrees with the CFD simulation results of the pulsed recirculation mixer reported previously.

5.6 Summary

Flow recirculation is observed in ridged channels. It's induced when an electric field of opposite direction to the pressure drop is imposed to the flow. Commercial CFD simulation software is used to characterize recirculation with respect to the external forces. It's found that recirculation becomes significant only when the external forces (the pressure forces and the electrokinetic force) are comparable. With current ridged channel configuration, significant recirculation is induced in ridged channels when K is in the range from 1.8 to 20, and strongest recirculation occurs when K approximates 4.5.

A micromixer that utilizes recirculation to improve fluid mixing is presented. Since a pulsed electric field is required during operation, the novel mixer is referred as pulsed

recirculation mixer. CFD simulation of the PRM shows that it yields excellent mixing result due to the periodic occurrence of recirculation. For example, it delivers a roughly 10-fold mixing amplification to flows at $Pe = 412$, when $K = 9.1$.

The experiment of mixing Rhodamine-B solution with DI water in a prototype PRM validates the superior performance of the PRM. Further experiments suggests the mixing performance of PRM correlates with the intensity of recirculation, as better mixing is achieved by PRM when K approaches 4.5.

The mixing of the PRM is related to the electric field strength, the frequency, the duty cycle, even the ridged channel geometries. It's noted that the mixing results presented here are not from the mixer at an optimized conditions, and better mixing performance can be achieved if an optimal working condition is applied to the PRM.

Table 5-1. Summary of boundary conditions for CFD simulation.

| Case No. | P (Pa) | V (Volt) | K | Flow rate (nL/s) | Related figures |
|----------|--------|----------|----------|------------------|-----------------|
| 1 | 75 | 0 | ∞ | -9.97 | Figure 5-7a |
| 2 | 100 | 20 | 30.9 | -10.07 | Figure 5-8a |
| 3 | 90 | 20 | 27.8 | -8.89 | |
| 4 | 80 | 20 | 24.7 | -7.71 | |
| 5 | 70 | 20 | 21.6 | -6.53 | Figure 5-8b |
| 6 | 60 | 20 | 18.5 | -5.35 | |
| 7 | 50 | 20 | 15.4 | -4.18 | |
| 8 | 40 | 20 | 12.3 | -3.00 | Figure 5-8c |
| 9 | 30 | 20 | 9.3 | -1.8 | |
| 10 | 25 | 20 | 7.7 | -1.23 | |
| 11 | 20 | 20 | 6.2 | -0.64 | Figure 5-8d |
| 12* | 15 | 20 | 4.6 | -0.05 | Figure 5-8e |
| 13 | 10 | 20 | 3.1 | 0.53 | Figure 5-8f |
| 14 | 5 | 20 | 1.5 | 1.11 | |
| 15 | 6 | 20 | 1.9 | 1.00 | Figure 5-8g |
| 16 | 7 | 20 | 2.2 | 0.88 | |
| 17 | 8 | 20 | 2.5 | 0.77 | |
| 18 | 0 | 20 | 0 | 1.69 | Figure 5-7b |

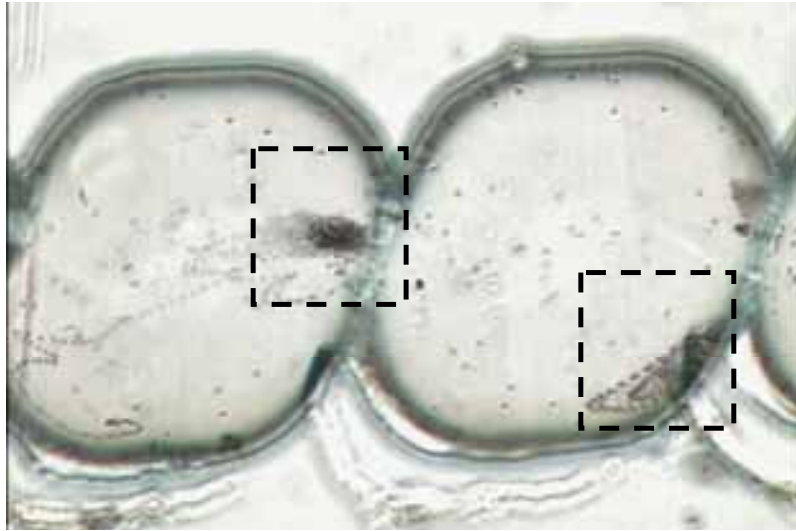


Figure 5-1. Microscopic image of microbead traces in a flow in ridged channels. The beads circulating around the ridges are the evidence of flow recirculation in ridged channels. The ridged channel has depth of 40 micron and width of 110 micron.

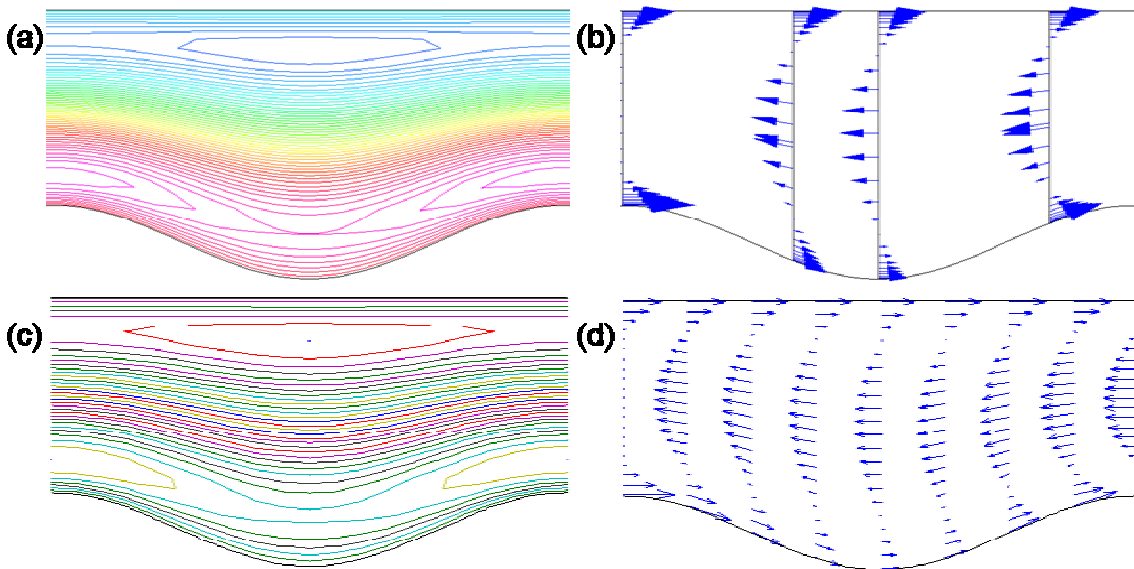


Figure 5-2. Plot of streamline and velocity profile of flows in the wavy channel calculated by CFD-ACE+ simulation and the analytical solution. Flow recirculation is observed from (a) the simulated streamline by CFD-ACE+ (a) and from (c) the streamline plot by the analytical solution developed in Chapter 4. Back flow is also observed in the velocity profiles of flow by CFD-ACE+ simulation (c) and the analytical solution (d). The two sets of results agree very well. The wavy channel has wavelength of 76.4 μm , wave amplitude of 5.5 μm , and width of 29 μm . External pressure and electric field are applied at the boundary such that $K=2$.

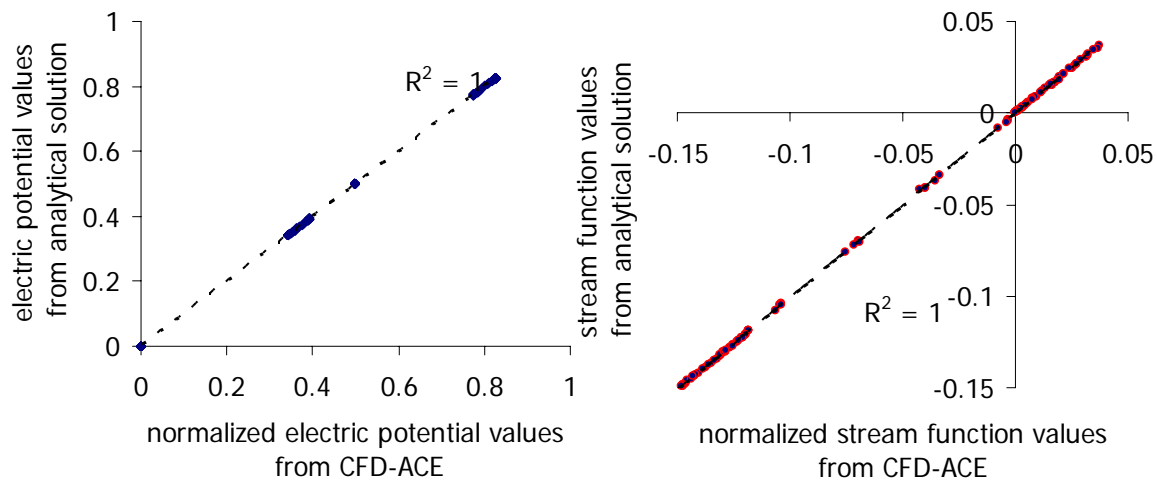


Figure 5-3. Comparison of electric potential and stream function data in flows in the way channel obtained by CFD-ACE+ simulation and the analytical solution.

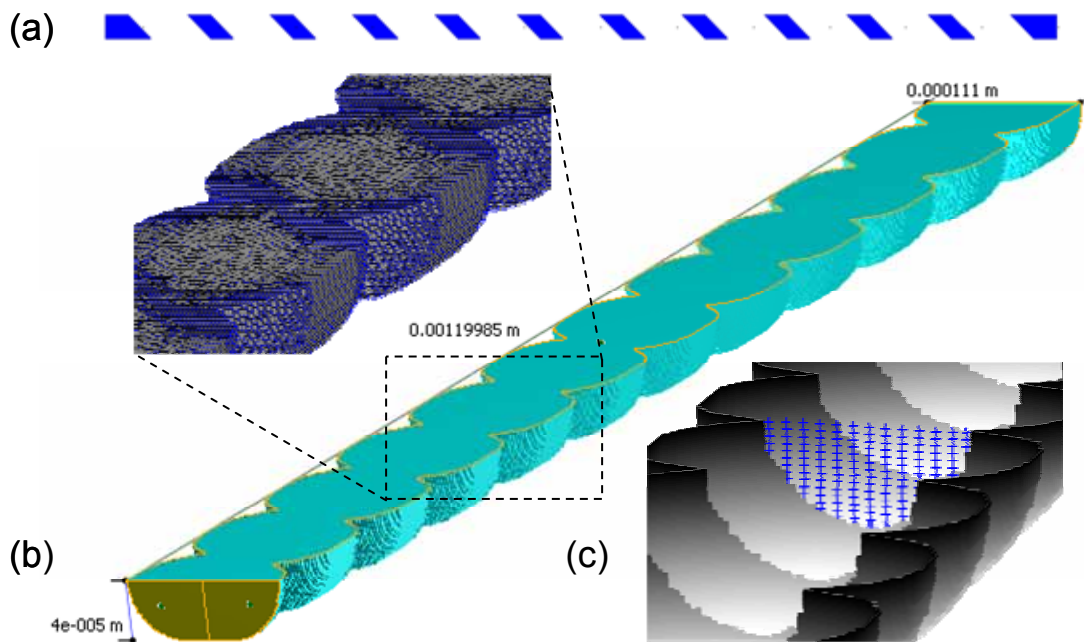


Figure 5-4. Simulation model used for simulating flows in ridged channel. Layout of mask (a), a series of parallelograms, is used in generating simulation models (b). The model contains 11 ridge structures resulting from 40-micron isotropic etching process. The length of mixer is 1200 micron, and the hydraulic diameter is 56 micron. The inset shows the detailed view of mesh structures in the model. A total of 141 points, labeled by cross signs, are defined around ridge structures in the model (c) and serves as the origins of streaklines in Figures 5-7 and 5-8.

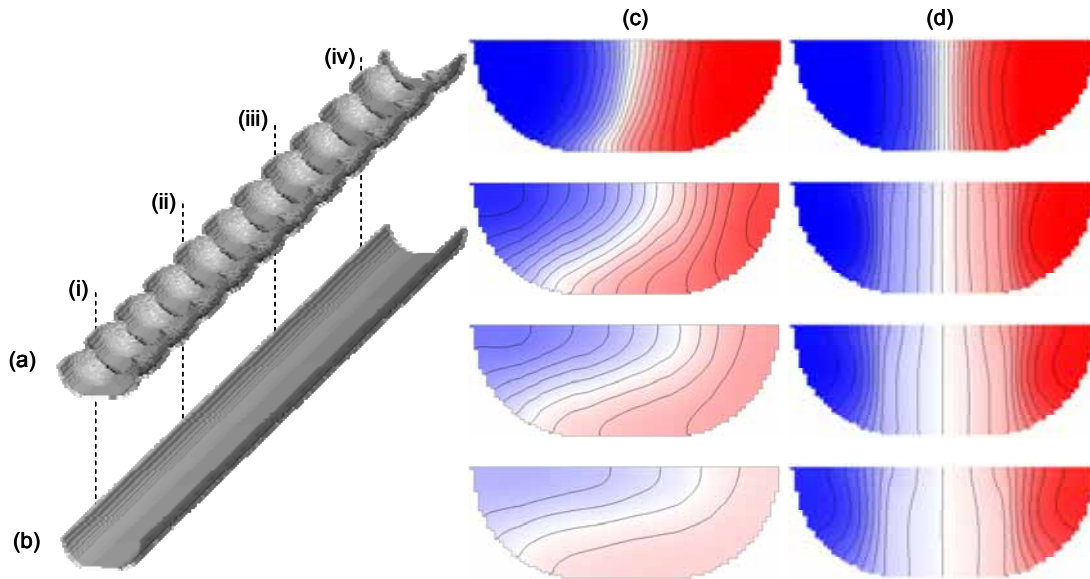


Figure 5-5. Simulation of fluid mixing in a ridged channel by CFD-ACE+. Two streams, solution of 0.1 mM specimen and water, are introduced into the ridged channel (a) at a preset flow rate. The cross sectional views with contour lines for specimen concentration in the ridged channel are shown in (c). The locations of the cross sections (top to bottom) are labeled in (a) as (i) to (iv). In this case, the flow rate is set at 5 nL/s. The Peclet number of the flow is 450, and the Reynolds number is 0.15. Also shown is a segment of regular channel (b) of same length and same etching depth but with no ridge structures. With same incoming streams, the cross sectional views of the regular channel are displayed in (d). Blue stream is water and red stream is specimen solution. The increment of the contour levels is 5 nM.

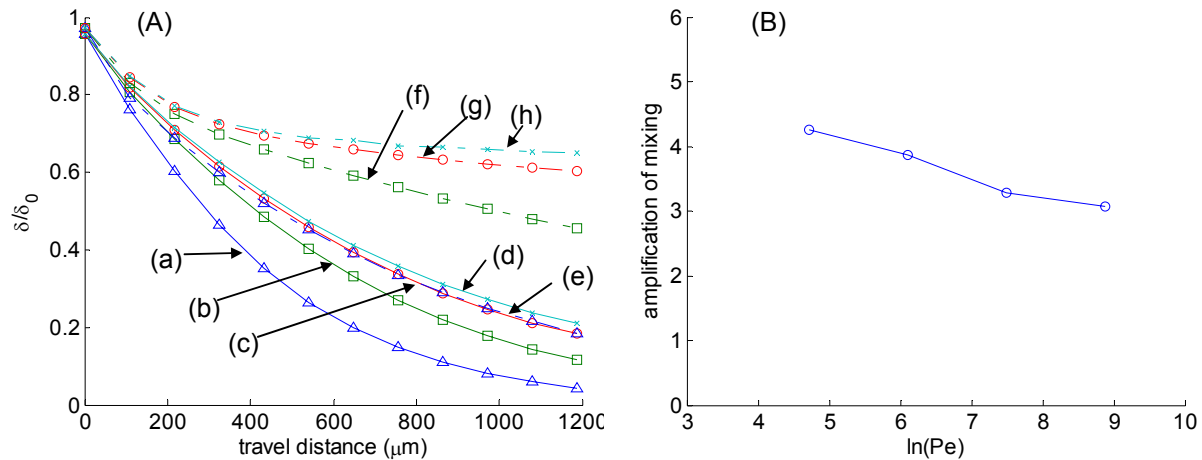


Figure 5-6. Simulated mixing performance of the PRM. (A) Plot of specimen concentration variation at different cross sections of ridged channel mixer. $\delta_0=0.05 \text{ mM}$, is the variance at the entrance of the channels. The continuous lines (a-d) represent the mixing coefficient in the ridged channel; while the dashed lines (e-h) are for the segment of regular channel. Data points marked as ‘ Δ ’ (a and e) are measured in flow with flow rate of 1.25 nL/s. As a result, the flow has Reynolds number of 0.04 and Peclet number of 113. Data with mark ‘ \square ’, ‘ o ’, and ‘ x ’ are from flows of $\text{Pe}=450$ (b and f), $\text{Pe}=1800$ (c and g), and $\text{Pe}=7200$ (d and h), respectively. (B) Plot of mixing amplification by the ridged channel as a function of $\ln(\text{Pe})$.

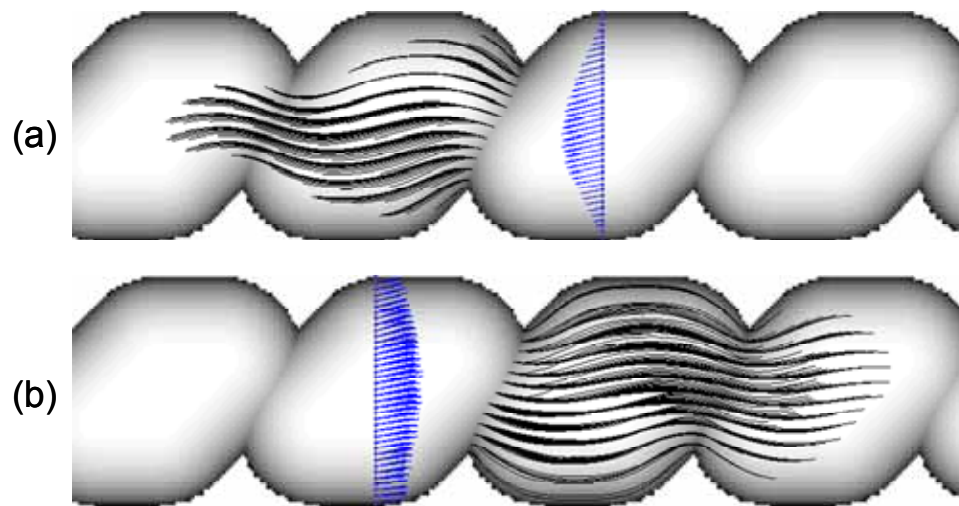


Figure 5-7. Top views of streaklines of massless particles convected by flows in ridged channels. The Poiseuille flow (a) and electroosmotic flow (b) in ridged channels simulated by CFD-ACE+ . Also presented are the velocity profiles in the flow. A 0.2 second duration is used in generating streaklines in pressure driven flow to ensure they fit in the figure.

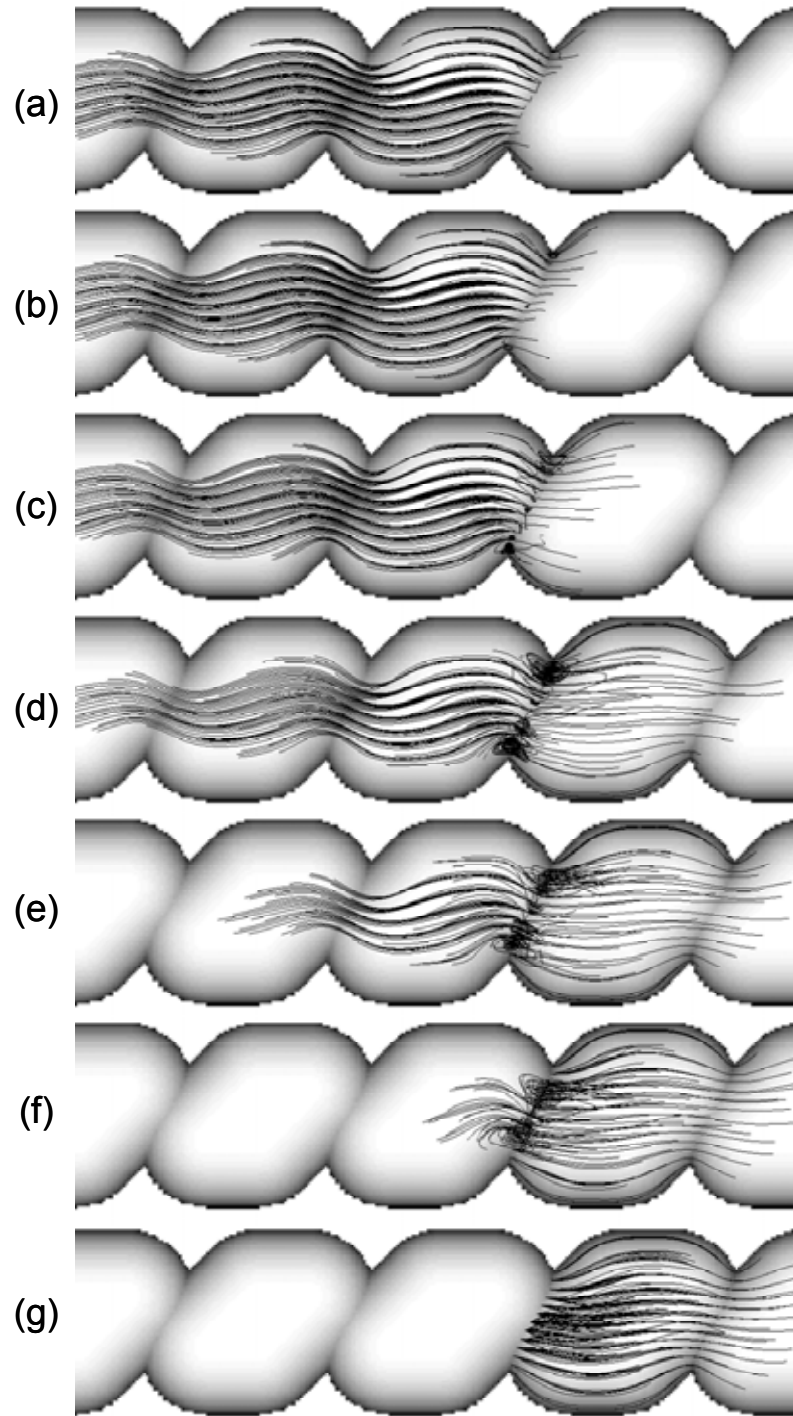


Figure 5-8. Streaklines of massless particles convected by flow in ridged channels at different K . The K in each case is (a) 30.9, (b) 21.6, (c) 12.3, (d) 6.2, (e) 4.6, (f) 3.1, and (g) 1.9, respectively.

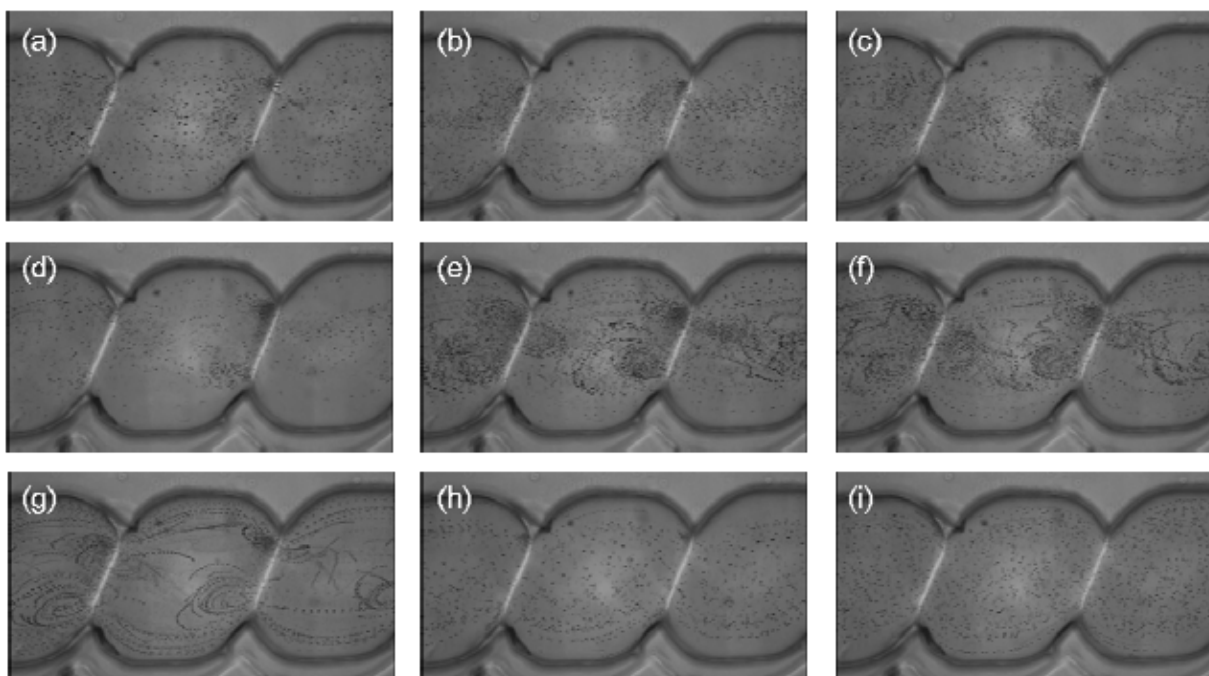


Figure 5-9. Flow patterns in a ridged channel made on plastic substrates. The ridged channel has a periodic length of 108.7 microns, width of 110 microns, depth of 40 microns, and ridge heights of 12 microns. The pressure remains constant in the experiment, while the electric field varies. The corresponding dimensionless parameter K in each case is (a) 3.16, (b) 3.48, (c) 3.87, (d) 4.35, (e) 5.81, (f) 6.97, (g) 11.6, (h) 17.4, and (i) 34.8.

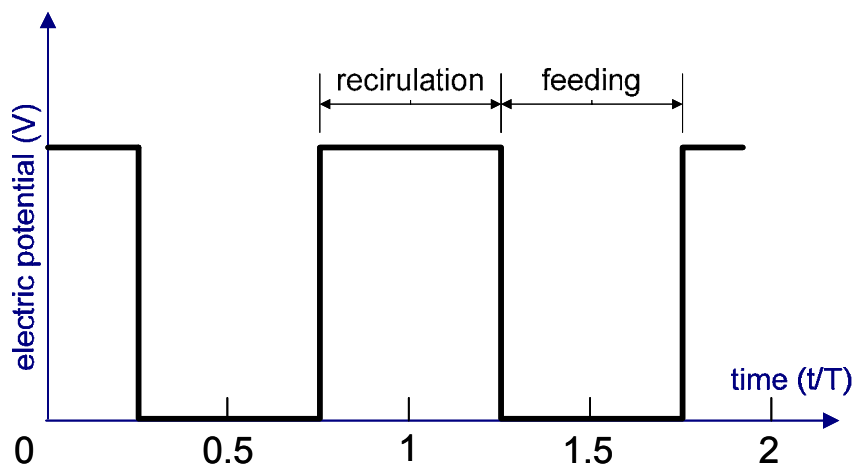


Figure 5-10. Pulsed electric signal applied in PRM for production of periodic recirculation. The example signal has period of T and duty cycle of 50%.

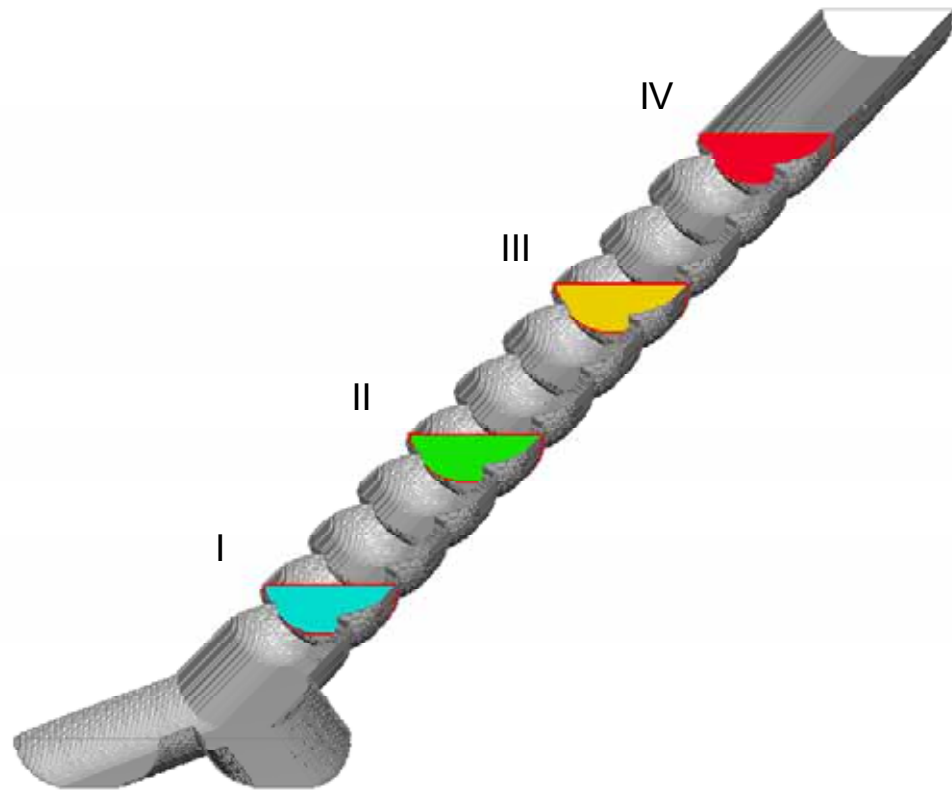


Figure 5-11. Simulation model for pulse recirculation mixer. The mixer consists of two inlets, one outlet and ten ridge structures. Labels I, II, III and IV, indicate the cross sections behind the 1st, 4th, 7th, and 10th ridge structures, respectively.

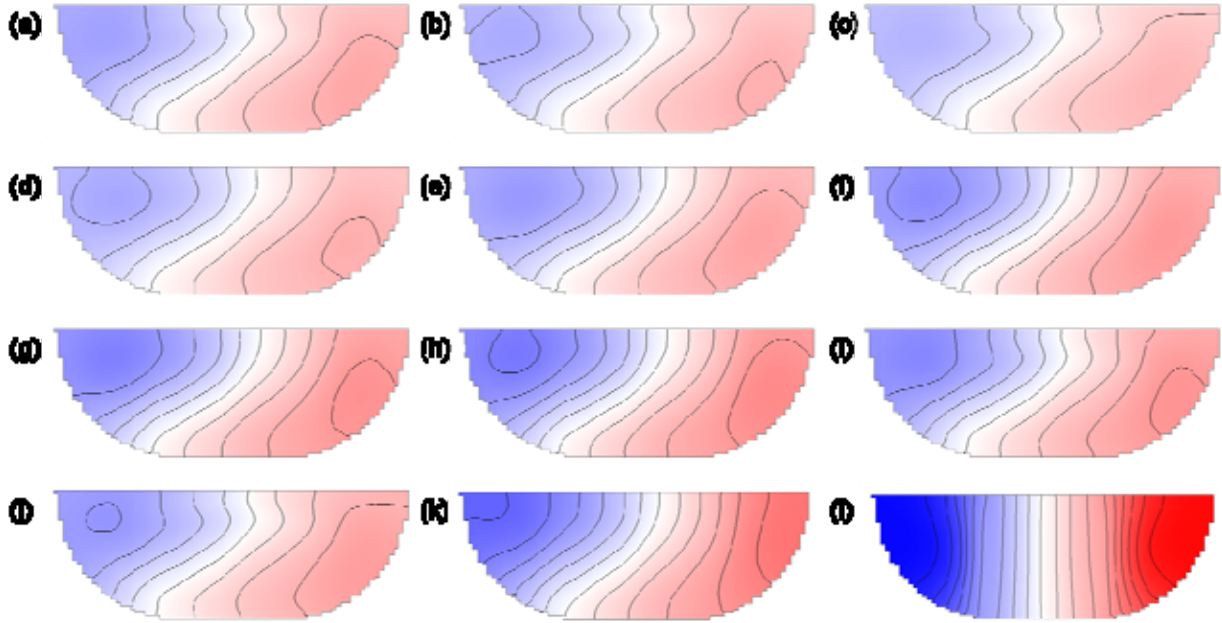


Figure 5-12. Temporal variation of Rhodamine-B distribution at a cross section of the periodic recirculation mixer over one period. (a-j) are Rhodamine-B distribution at cross section (II in Figure 5-11) at the interval of 0.1 second. Also shown are the Rhodamine-B distribution when a constant electric field applied (k) and the Rhodamine-B distribution at cross section of a regular channel without any ridge structures (l).

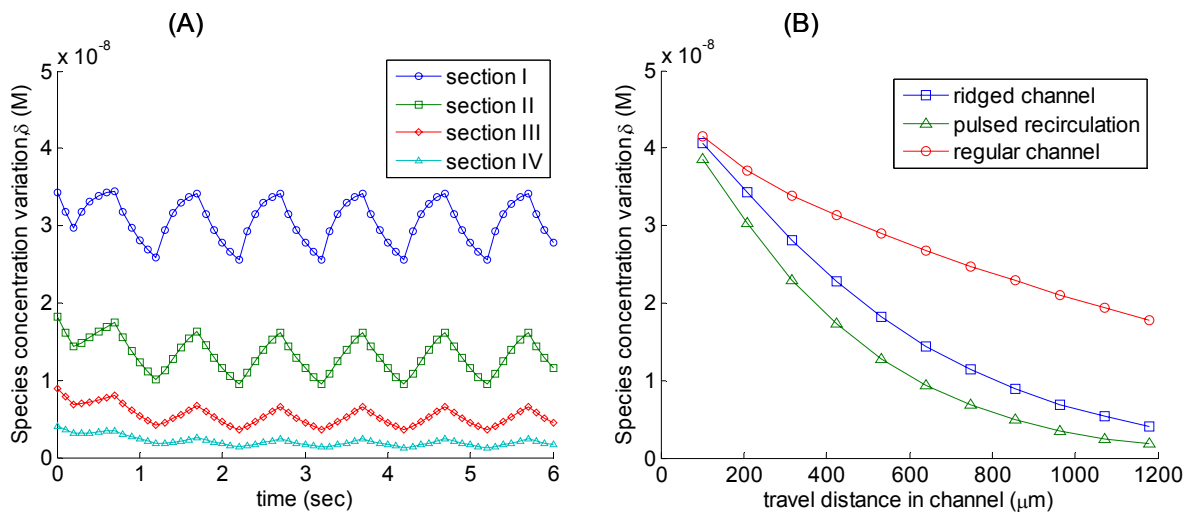


Figure 5-13. Evolution of the Rhodamine-B concentration variation in the fluid in a PRM. (A) The evolution of Rhodamine-B concentration variation at cross sections of pulsed recirculation mixer (I, II, III, and IV in Figure 5-11). The time-averaged variation during one cycle is plotted against traveling distance in (B). Also plotted in (B) are the Rhodamine-B concentration variations in the same ridged channel but without the application of electric field, as well as the variations in a segment of regular channel.

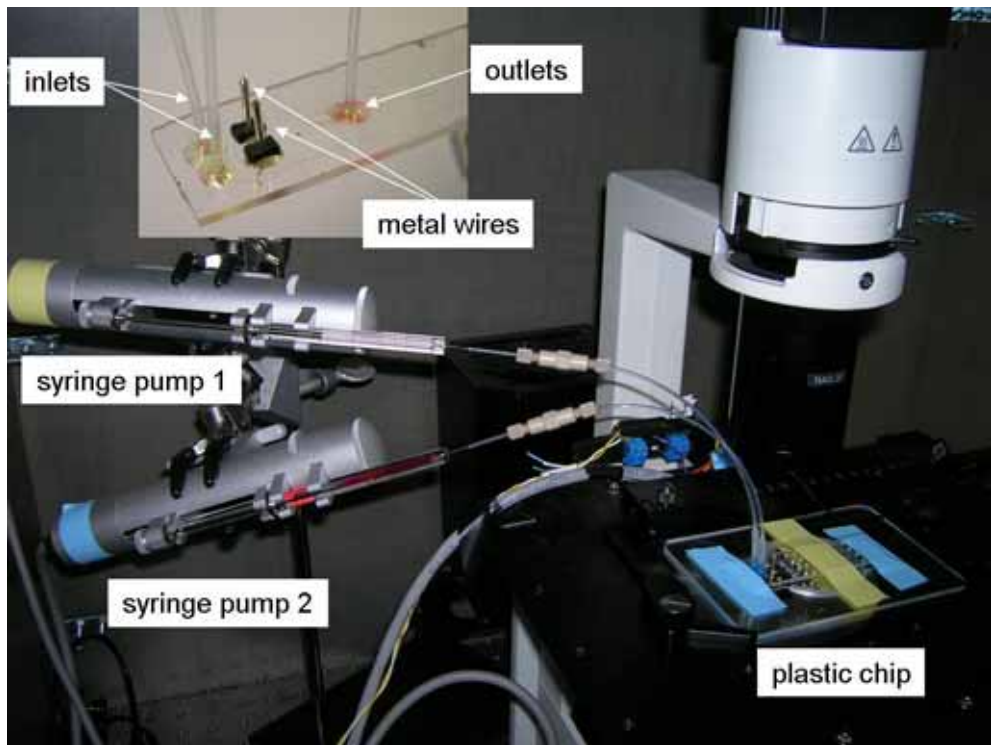


Figure 5-14. Experiment setup for the fluid mixing of Rhodamine-B solution and DI water in a prototype PRM. The two incoming fluids are pumped into PRM by two sets of syringe pumps that are connected to the inlets. External electric field is imposed via the two metal wire glued on the mixer. A detailed view of PRM is shown in the inset.

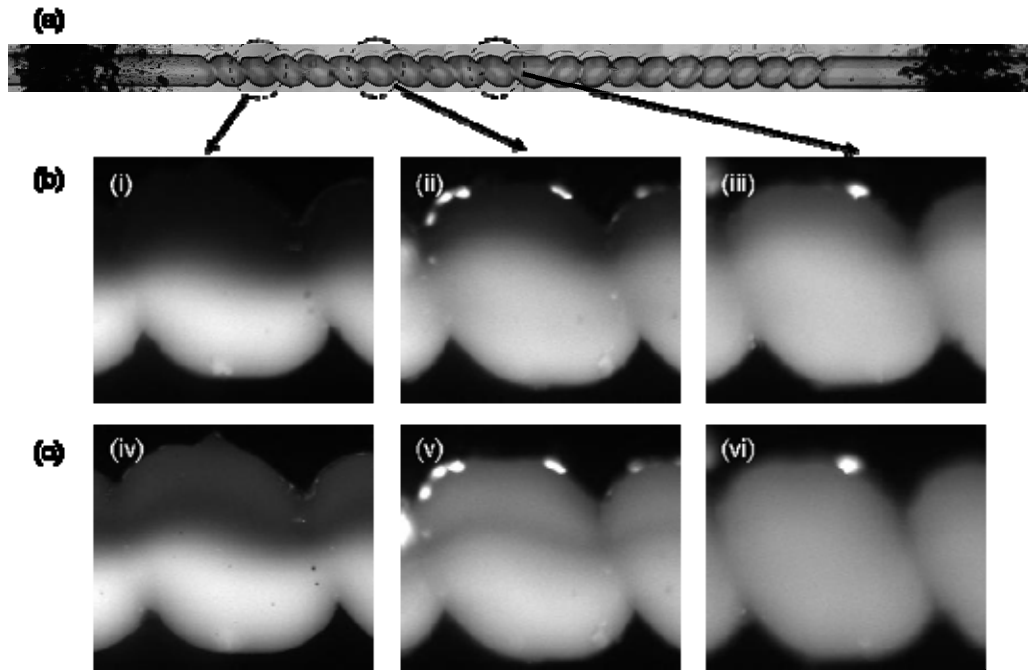


Figure 5-15. Comparison between the flow in the inactive mixer and the flow in the active mixer. (a) A top view of the ridged channel portion between the two electrodes. (b) Without the application of electric field, the top views (i, ii, iii) of fluid flows in the channel, at 1st, 5th and 9th ridge structures. The incoming streams are 0.1mM RB solution and DI water, both are pumped at flow rate of 13 nL/s. (c) With the application of a pulsed electric field, the top views (iv, v, vi) of fluid flows in the channel, at the same locations. The flow rate is set at 13 nL/s, and the average electric field is about 1000 V/cm, the oscillation frequency is 5 Hz, and the duty cycle is 50%. The resulting K is about 20.

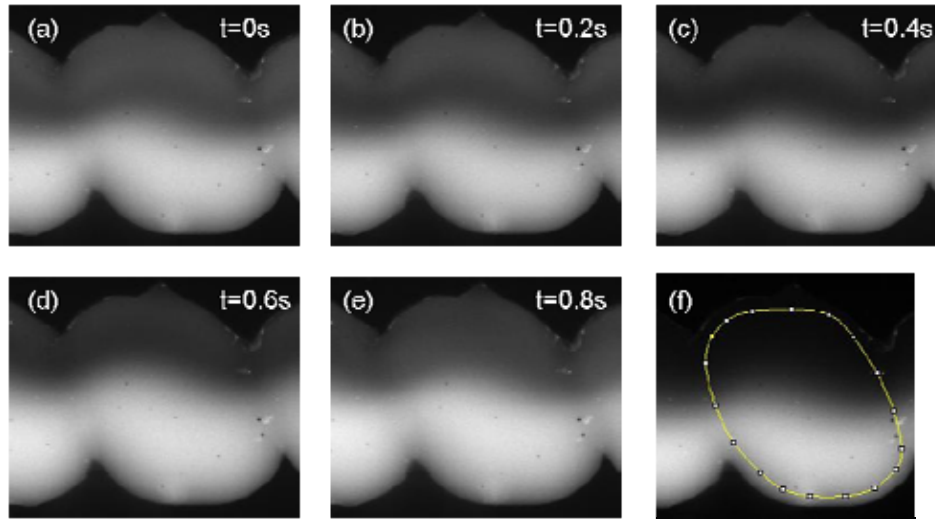


Figure 5-16. Temporal variation of fluid mixing in PRM during one cycle. The pulsed electric field has frequency of 1 Hz and duty cycle of 50%. The operation parameter K used in this mixing test is 20. Images are taken at the first ridge structure at 0.2 second interval. Without the application of the pulsed electric field, the fluid appears steady and the top view is shown in (f). The yellow line encloses area that used to generate the intensity histogram profile.

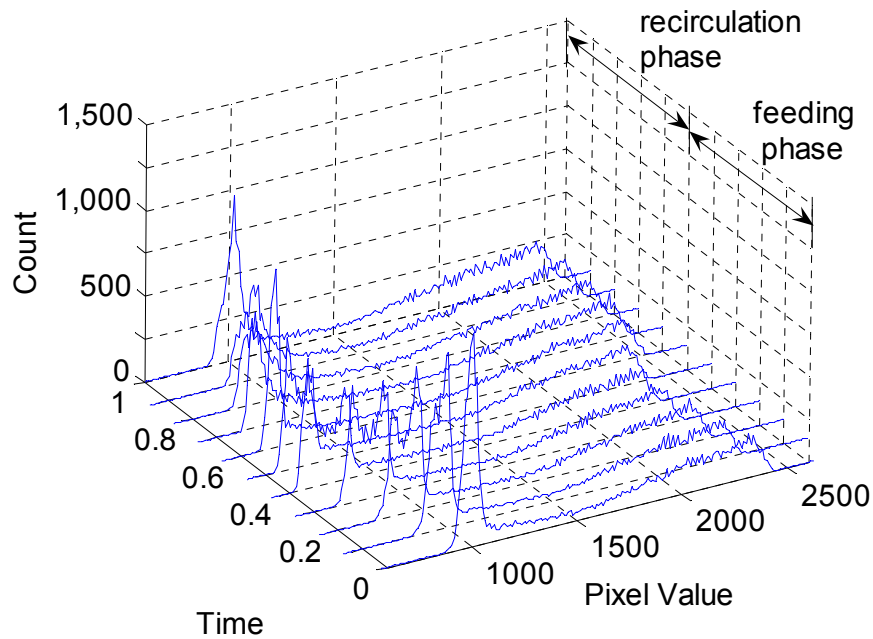


Figure 5-17. Temporal evolution of intensity histogram profile in the ridge channel in one cycle. The pulsed electric field has frequency of 1 Hz and duty cycle of 50%. The operation parameter K used in this mixing example is 20.

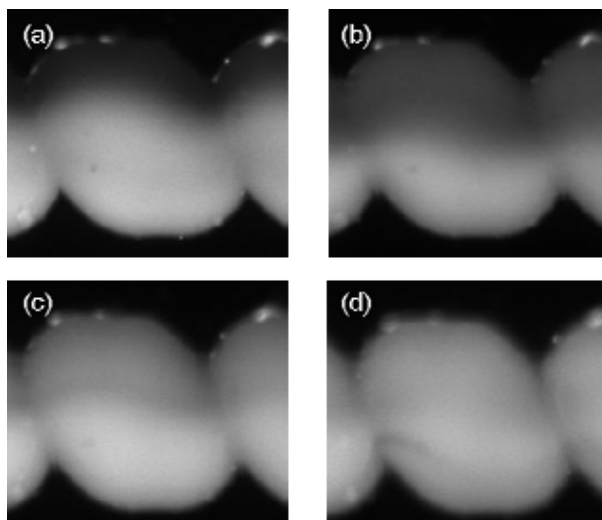


Figure 5-18. Effect of parameter K on mixing performance of pulsed recirculation mixer. Images are taken at the 5th ridge. The electric field is 0, 666, 1000, and 1333 V/cm, respectively; and the operation parameter K is (a) inf, (b) 30, (c) 20, and (d) 15. The ratio of standard deviation of intensity to mean is 0.34, 0.32, 0.19 and 0.12, respectively.

CHAPTER 6 CONCLUSIONS AND FUTURE DIRECTIONS

6.1 Conclusions

The main objective in this research work is to design an effective and efficient microfluidic mixer for lab-on-chip devices. To achieve this, a novel structure, called micro ridges is developed via judicious design in isotropic etching. Flow twisting is observed as fluid is pumped through ridged channels. Deconvolution microscopy is explored and used in validating the flow twisting and evaluation of fluid mixing by the twisting effect.

Flow recirculation is observed in a pressure fluid flow in microchannels of varying cross section area, when an electric field of opposite direction is imposed. It's first observed in the ridged channel and then studied in a wavy channel for its simple channel geometry. An analytic solution to flow in a wavy channel is developed in this research using complex function formulation and boundary integral formulation. The onset conditions for recirculation in a wavy channel are found dependent on one dimensionless parameter related to external forces and two dimensionless parameters related to the channel geometry. The theoretical prediction agrees well with experimental observation of a seeded flow in wavy channels created on PDMS substrate.

Following the study of recirculation in the 2D wavy channel, recirculation in the 3D ridged channels is studied, both theoretically and experimentally. The conclusion drawn from the 2D geometries is used as guidelines in investigating recirculation in the more complex 3D counterpart. A commercial computational fluid dynamic package, CFD-ACE+, is used to model the fluid flow in the ridged channel. Similar trends are observed in the onset and size of the flow recirculation in the ridged channels.

A microfluidic mixer, called pulsed recirculation mixer, is designed and fabricated on plastic substrates. Faster and effective mixing is achieved by the prototype PRM as predicted by the numerical simulation. The mixing results, as a result of the flow recirculation, significantly depend on a dimensionless parameter related to the external forces. Fluid mixing experiments are conducted on a prototype PRM, and the results confirm the numerical predictions. The major objective of the research is achieved: pulsed recirculation mixer is an effective and efficient mixer for microfluidic systems.

To recapitulate the research work on the pulsed recirculation mixer design, a road map is presented in Figure 6.1 to illustrate the work flow. The research work starts from the observation of recirculation in ridged channel (Figure 6.1a). By simplifying such recirculation to flow in the wavy channel (Figure 6.1b and 6.1c), an analytical solution is developed so that a parametric study on the recirculation is possible (Figure 6.1d). The systematic investigation of flow recirculation in the wavy channel helps study the flow recirculation in the ridged channel both numerically and experimentally (Figure 6.1e). A full cycle of research work has been accomplished, and the results are eventually applied in design and optimization of a microfluidic mixer based on flow recirculation (Figure 6.1f).

6.2 Future Directions

6.2.1 Deconvolution Algorithm

As pointed in Chapter 3, commercial deconvolution software is used in deconvolution microscopy, and the results are sometimes imperfect. To improve the quality of reconstructed image, new deconvolution algorithm can be developed for specific application of visualizing microfluidic flows. The new algorithm should be based on the blind MLE deconvolution algorithm, since it yields the best results among all tested deconvolution algorithms. Additional constraints should be applied to penalize any non-zero value at pixels outside the channel

geometry in the iteration process. Fast and better reconstruction is expected from deconvolution microscopy coupled with this new deconvolution algorithm.

6.2.2 Optical Sectioning for Periodic Flow

The deconvolution microscopy technique developed in Chapter 2 is limited to visualizing steady flows in microchannels. This is due to the difficulty in optical sectioning of unsteady fluid flow. Optical sectioning requires adjust of optical focal plane and subsequent image acquisition in steps, therefore the operation takes considerable length of time. Steady flow doesn't change during the process of optical sectioning, and the images taken at each step can be assumed of flow of same instant. However for unsteady flow, this assumption becomes invalid.

One of future work is to improve it for visualizing a periodic, as it is desired in evaluating mixing efficiency by pulsed recirculation mixer in which fluid flow is time-periodic. The preliminary experiments in this dissertation work only confirm that a PRM delivers better mixing results than a ridged channel mixer. This is proved by the experimental observation from the top view of the fluid flow in the mixer. However, this top view only represents the mixing of fluid at the focal plane. To obtain an adequate performance of fluid mixing by PRM, one needs to have a cross sectional view of the fluid flow in the channel. Deconvolution microscopy is not suitable to evaluate the mixing performance of a PRM, for its flow is unsteady.

However, for periodic flow, optical sectioning can be achieved by phase locking the image acquisition with the periodicity of the flow, so that the acquired images are from the periodic flow at different instant but of same phase in a period. Hence the images can be regarded from same instant. As of visualizing flow in the PRM, it can be achieved by synchronizing the CCD camera exposure and the application of electric field. In practice, one can use a function generator to output two waveforms of same frequency but with a fixed phase shift. One signal

will be used to control a relay for the pulsed electric field in the mixer, and the other will be connected to a CCD camera for triggering the exposure at each step of optical sectioning.

Another issue in deconvolution microscopy for unsteady flow is the insufficient exposure in image acquisition. For visualizing steady flow, the exposure time of CCD camera can be set long enough so that the collected signal is stronger than the thermal noise. However for periodic flow of short period, shorter exposure is required and the resulting signal may be overshadowed by the electric noises in the CCD camera. Therefore multiple exposures may be taken at each step of the optical sectioning, and the average, with better signal to noise ratio, can be used in deconvolution.

6.2.3 Optimization of Pulsed Recirculation Mixer

Once an accurate evaluation of fluid mixing in PRM becomes possible, the complete experimental characterization of PRM can be performed. In the CFD simulation of PRM, there are three parameters that will affect the performance of the mixer. They are K , the ratio of the external forces, the oscillation frequency of the repulsed electric field, and its duty cycle. In current work, only K is studied, as it's the major factor in determining the intensity of flow recirculation in ridged channel. In the future work, a parametric study may be carried out to characterize the mixer, and search for the optimal working condition.

6.2.4 Analytical Solution of EOF in Irregular Channel

Another possible direction is to further develop the analytical method used in solving EOF in wavy channel and apply it in solving EOF in other 2D periodic geometries as shown in Figure 6-2. Demonstrated by the micro particles seeded in the fluid, the flows in these periodic channels also have recirculation inside the channel, but the shape of recirculation region appears different from the one in wavy channel. Further research work can start from the current

solution to EOF in wavy channel and develop a general analytical method to solve flow in channels of any periodic geometry.

As pointed previously, the current method is capable of solving a Stokes flow, which is governed by a linear ordinary differential equation and prescribed by boundary conditions defined on sinusoidal walls. And it is well known that any periodic geometry can be composed by multiple sinusoidal according to Fourier theorem. Hence the solution to the flow in channel of periodic shape could be obtained by solving flow with each sinusoidal boundary and superposing all the individual solution together.

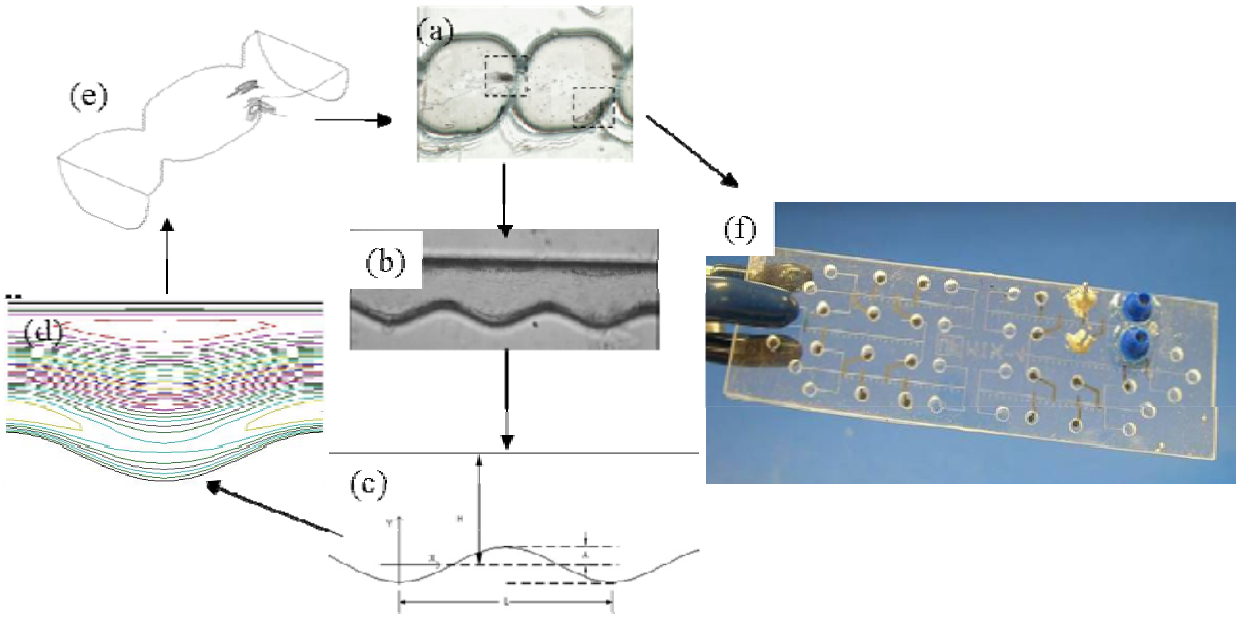


Figure 6-1. Roadmap of research work on the development of the pulsed recirculation mixer. Flow recirculation is observed (a) and investigated in the wavy channel (b-d) and in the ridged channel (e), before applied in the design and optimization of the pulsed recirculation mixer (f).

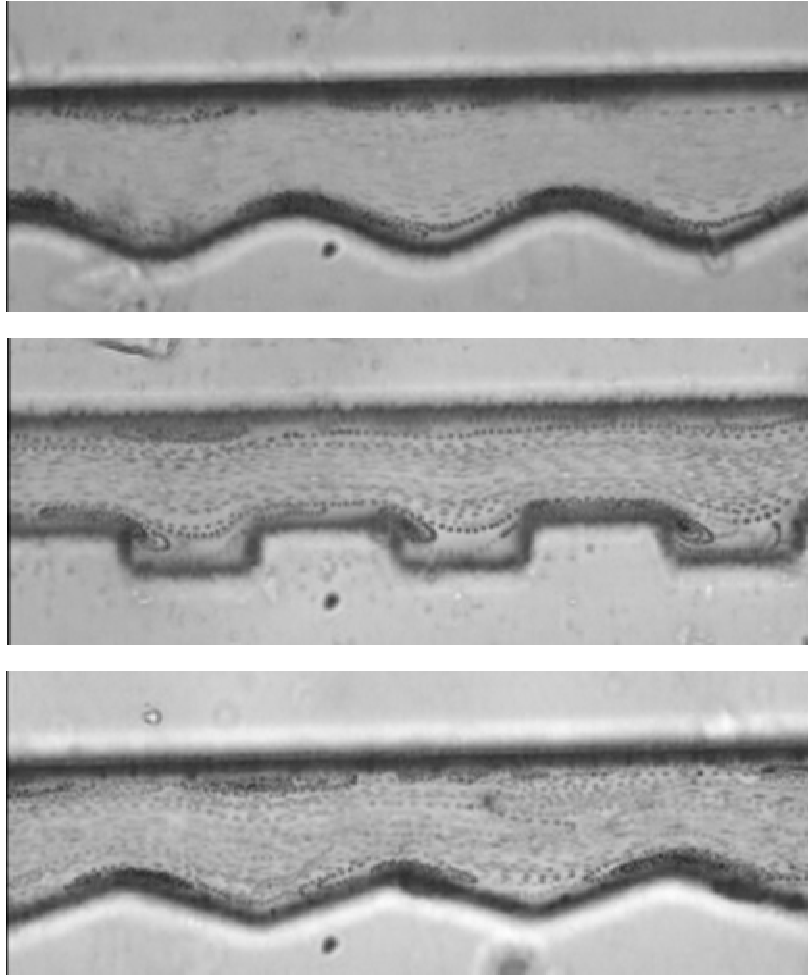


Figure 6-2. Microscopic images of fluid flow in periodic channels of different profiles (sinusoidal, square-wavy, and triangle-wave). The fluid is seeded with microbead of 0.75 micron in diameter. Pathlines of beads is obtained by overlapping 60 consecutive images. EOF is in the opposite direction of the pressure gradient. The recirculation flow regions are indicated by denser bead population (more dark spots).

APPENDIX A POINT SPREAD FUNCTION

Point Spread Function (PSF) is a spatial function of light intensity describing the output of the imaging system (the microscope) for an input point source. As the most fundamental characteristic of an imaging system, PSF is viewed as the impulse response function of a microscope in spatial domain.¹⁰⁶

For a shift-invariant, ideally corrected and aberrant free microscope, the PSF, axisymmetric along the optical axis and symmetric about conjugate image plane, is given by,¹⁰⁶

$$h(x, y, z) = \left[C \int_0^1 J_0(v\rho) \exp\left(\frac{i\mu\rho^2}{2}\right) \rho d\rho \right]^2 \quad (\text{A-1})$$

In Equation A-1, (x, y, z) are coordinates from the conjugate point; J_0 is the zeroth-order Bessel function of the first kind; ρ , μ , and ν are dimensionless numbers defined as $\rho = \frac{\sqrt{x^2 + y^2}}{a}$,

$\mu = \frac{2\pi}{\lambda} \frac{a^2}{f(f+z)} z$, and $\nu = \frac{2\pi}{\lambda} \frac{a}{f} \sqrt{x^2 + y^2}$, where a is the radius of objective aperture, f is

the focal length, and λ is the wavelength of emission light; and C is a constant. The expression given above is only one approximation for the three dimensional point spread function. Many alternative forms of 3D PSF have been reported based on scalar diffraction theory.^{9-11, 61}

The plot of PSF from Equation A-1 is a 3D diffraction pattern, centered on the conjugate image of the point source located in the image plane, as shown in Figure A-1.

On the image plane where $z = 0$, the PSF is simplified to $h(x, y) = \left[C \int_0^1 J_0(v\rho) \rho d\rho \right]^2$,

which represents a series of concentric spheres known as airy disk (Figure A-2). The radius of airy disk (distance between the central maximum and the first minimum) is related to the numerical aperture (NA) of the objective lens,

$$r_{lateral} = \frac{0.61\lambda}{NA}. \quad (\text{A-2})$$

In the axial direction, the intensity profile (Figure A-3) is similar to that on lateral direction, and the distance between the maximum intensity of the central bright region to the first point of minimum intensity along optical axis is given by

$$r_{axial} = \frac{2\lambda n}{NA^2}. \quad (\text{A-3})$$

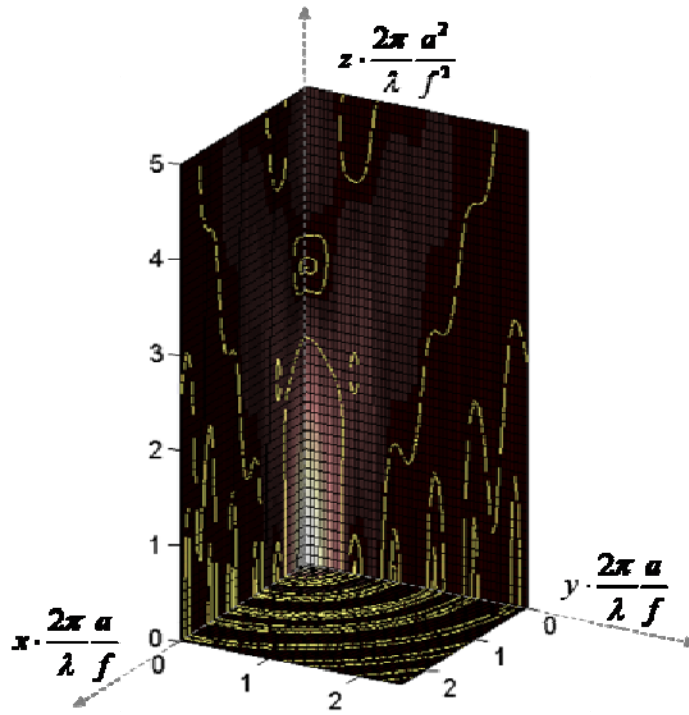


Figure A-1. Plot of point spread function in an octant of 3D space.

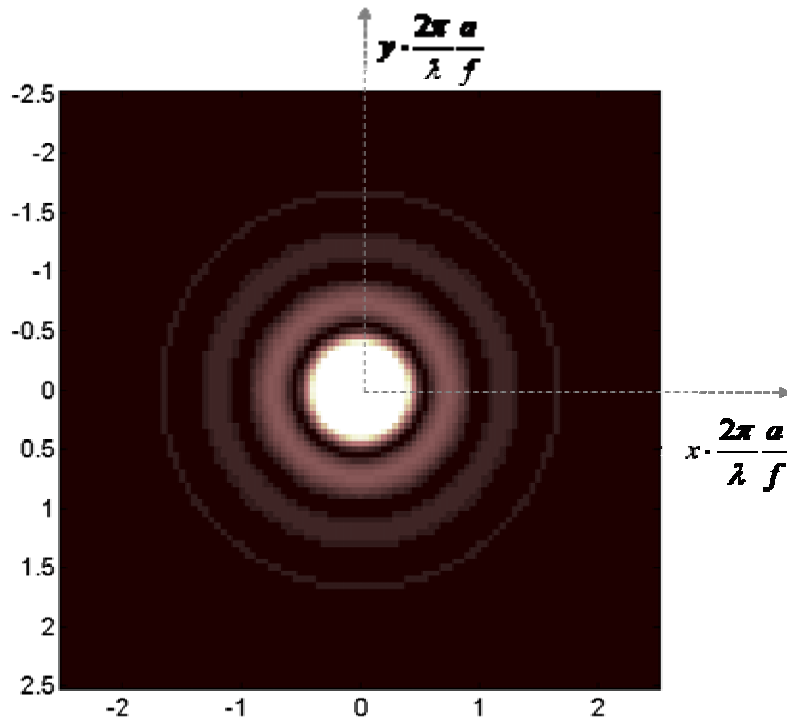


Figure A-2. Airy disk, plot of PFS at the plane of $z = 0$.

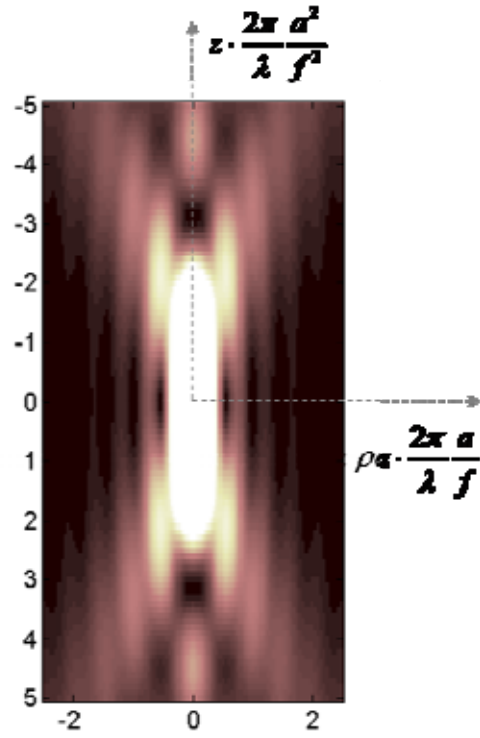


Figure A-3. Plot of PSF on a 2D plane along z axis.

APPENDIX B DECONVOLUTION ALGORITHMS*

Mathematically, the general relationship between image $i(x, y, z)$, object $o(x, y, z)$ and point spread function $h(x, y, z)$ is expressed as a spatial convolution, i.e. a triple integration over space,

$$i(x, y, z) = \iiint h(x - \xi, y - \eta, z - \zeta) o(\xi, \eta, \zeta) d\xi d\eta d\zeta + n(x, y, z), \quad (\text{B-1})$$

where $n(x, y, z)$ is additive random noise. By denoting convolution operation as \otimes , the above equation is abbreviated as $i = h \otimes o + n$. This relationship indicates that the images taken from the microscope deviate from their real counterparts, commonly referred to as optical blur.

Deconvolution is the mathematical operation to invert the convolution process, so that images are reconstructed by reducing the noise and correcting for the optical blur. Once the images are reconstructed, they are stacked to form a 3D data set, with each component representing the fluorescence intensity at the corresponding point in object space. A variety of deconvolution algorithms has been developed and they are summarized here.

B.1 Inverse Filter

An inverse filter algorithm such as a Wiener filter⁶⁵ transforms the stack of raw images $i(x, y, z)$ in the spatial domain into $I(u, v, w)$ in the Fourier domain. Since a convolution in the spatial domain is equivalent to a point-by-point multiplication in the Fourier domain, i.e.,

$$FFT[h(x, y, z) \otimes o(x, y, z)] = FFT[h(x, y, z)] \cdot FFT[o(x, y, z)], \quad (\text{B-2})$$

the image formation in Fourier domain is expressed as

$$I(u, v, w) = H(u, v, w) \cdot O(u, v, w) + N(u, v, w), \quad (\text{B-3})$$

where $I(u, v, w)$, $O(u, v, w)$, $H(u, v, w)$ and $N(u, v, w)$ are the respective counterparts of i , o , h and n in the Fourier domain.

When noise is negligible compared to the coherent signal, the object is easily obtained by dividing by H on both sides of Equation B-3,

$$\hat{O}(u, v, w) = \frac{I(u, v, w)}{H(u, v, w)}, \quad (\text{B-4})$$

where “^” indicates an estimation. In cases when noise cannot be neglected, a Wiener inverse filter is used to minimize degradation from noise. Assuming the ratio of the power spectrum of the noise to the object is b , the estimate of the object becomes

$$\hat{O}(u, v, w) = \frac{H^*(u, v, w)}{|H(u, v, w)|^2 + b} I(u, v, w), \quad (\text{B-5})$$

where “*” indicates the complex conjugate. Once the reconstructed object is found in Fourier domain, it may be applied the inverse Fourier transform, and the object is obtained in spatial domain as,

$$\hat{o}(x, y, z) = IFFT[\hat{O}(u, v, w)]. \quad (\text{B-6})$$

B.2 Constrained Iterative Deconvolution

Many popular deconvolution algorithms, such as the Jansson Van-Cittert algorithm,⁶⁶ the Gold algorithm,⁶⁷ and the Richardson Lucy (also known as Maximum Likelihood Estimation or

* Part of this chapter has been published in “Deconvolution Microscopy for Flow Visualization in Microchannels”, *Analytical Chemistry*, 2007, **79**(6): p. 2576-2582.

MLE) algorithm^{68, 69} are classified as constrained iterative algorithms. The object estimation is achieved in a iterative process by imposing various constraints. The positive constraint, a primary and primitive one, ensures the estimate of the object, $\hat{o}(x, y, z)$, is always positive. In each iteration, a new estimate of object $\hat{O}^{k+1}(u, v, w)$ is calculated using $I(u, v, w)$, $H(u, v, w)$, and $\hat{O}^k(u, v, w)$ from the last iteration. When the object converges or other criteria reach a preset threshold, such as the maximum number of iterations is reached, the iteration process stops, and the current $\hat{O}(u, v, w)$ is inverse Fourier transformed to the spatial domain. In practice, $\hat{O}(u, v, w)$ from the inverse filter deconvolution algorithm is often used as an approximation in the first iteration. The Jansson Van-Cittert, Gold, and MLE algorithms are different in the new object that are generated in each iteration; and they are expressed as

$$\hat{O}^{(k+1)}(u, v, w) = K \left\{ \hat{O}^{(k)}(u, v, w) + W \left[I(u, v, w) - \hat{H}^{(k)}(u, v, w) \cdot \hat{O}^{(k)}(u, v, w) \right] \right\}, \quad (\text{B-7})$$

$$\hat{O}^{(k+1)}(u, v, w) = K \hat{O}^{(k)}(u, v, w) \frac{I(u, v, w)}{\hat{H}^{(k)}(u, v, w) \cdot \hat{O}^{(k)}(u, v, w)}, \quad (\text{B-8})$$

and,

$$\hat{o}^{(k+1)}(x, y, z) = K \hat{o}^{(k)}(x, y, z) \left\{ \hat{h}^{(k)}(x, y, z) \otimes \left[\frac{i(x, y, z)}{\hat{h}^{(k)}(x, y, z) \otimes \hat{o}^{(k)}(x, y, z)} \right] \right\}. \quad (\text{B-9})$$

Here K is a normalized constant, and W is a weight function. In all of these algorithms, the PSF ($\hat{H}^{(k)}$ or $\hat{h}^{(k)}$) remains the same in each iteration.

B.3 Blind Deconvolution

Blind deconvolution algorithms⁷⁰ use the same principle as constrained iteration algorithms, except that they also update the PSF in each iteration. This family of algorithms excels when the PSF is unknown or is perhaps not accurately measured. In each iteration Equations B-10, B-11, and B-12 below are paired with Equations B-7, B-8, and B-9, respectively, to compute the PSF and the object. In the first iteration, the initial guess of the object is usually set as the acquired image, and the initial guess of the PSF is simply set as the one from a theoretical model or unity.

$$\hat{H}^{(k+1)}(u, v, w) = K' \left\{ \hat{H}^{(k)}(u, v, w) + W' \left[I(u, v, w) - \hat{H}^{(k)}(u, v, w) \cdot \hat{O}^{(k)}(u, v, w) \right] \right\} \quad (\text{B-10})$$

$$\hat{H}^{(k+1)}(u, v, w) = K' \hat{H}^{(k)}(u, v, w) \frac{I(u, v, w)}{\hat{H}^{(k)}(u, v, w) \cdot \hat{O}^{(k)}(u, v, w)} \quad (\text{B-11})$$

$$\hat{h}^{(k+1)}(x, y, z) = K' \hat{h}^{(k)}(x, y, z) \left\{ \hat{o}^{(k)}(x, y, z) \otimes \left[\frac{i(x, y, z)}{\hat{h}^{(k)}(x, y, z) \otimes \hat{o}^{(k)}(x, y, z)} \right] \right\} \quad (\text{B-12})$$

APPENDIX C
SOLUTION TO ELECTRIC POTENTIAL AND STREAM FUNCTION*

This appendix describes the details in solving the periodic functions $G^\varphi(x)$, $G^\beta(x)$, $R^\varphi(x)$, $R^\beta(x)$, $Q^\varphi(x)$, and $Q^\beta(x)$ that are used for calculating $G(\zeta)$, $R(\zeta)$ and $Q(\zeta)$. The symmetry of the channel geometry ensures that for Stokes flow $\overline{\Theta(x)} = \Theta(-x)$ so that $\Re[\Theta(x)] = \frac{\Theta(x) + \Theta(-x)}{2}$ and $\Im[\Theta(x)] = \frac{\Theta(x) - \Theta(-x)}{2i}$.

C.1 Electric Potential Solution

Equation 4-22 and Equation 4-23 in Chapter 4 can be reduced to

$$m(g_m^\varphi + g_{-m}^\varphi) = 0 \quad (C-1)$$

and

$$m(g_m^\beta + g_{-m}^\beta) = \frac{\alpha}{4\pi}(\delta_{m,1} - \delta_{m,-1}). \quad (C-2)$$

Similarly, Equation 4-26 becomes

$$\exp(nh)g_n^\varphi - \sum_{m=-\infty}^{+\infty} g_m^\beta E_{m,n} = 0, \quad (C-3)$$

where $E_{m,n} = \begin{cases} \delta_{m,0} - \frac{\alpha}{2}(\delta_{m,1} - \delta_{m,-1}) & , n = 0 \\ \frac{m}{n} I_{n-m}(-n\alpha) & , n \neq 0 \end{cases}$, δ is Kronecker delta, and $I_n(z)$ is the n^{th} order

modified Bessel function of first kind, $I_n(z) = \frac{1}{2\pi} \int_{\theta=-\pi}^{\pi} \exp(z \cos \theta) \cos n\theta d\theta$. Equations C-1, C-

2, and C-3 form a complete set for solving coefficients $\{g_m^\varphi\}$ and $\{g_m^\beta\}$, $m \in \{\mathbb{Z} \setminus \{0\}\}$.

Since the electric field is $\bar{E} = -\nabla \phi$, as a result, the tangential electric field strength along the walls (Equation 4-27 and Equation 4-28) can be evaluated using:

$$E_t^\varphi(x) = \sum_{m=-\infty}^{+\infty} 2mg_m^\varphi \exp(-imx) - \frac{1}{2\pi} \quad (C-4)$$

and

$$E_t^\beta(x) = \frac{\sum_{m=-\infty}^{+\infty} [m(g_m^\beta - g_{-m}^\beta)] \exp(-imx) - \frac{1}{2\pi}}{\sqrt{1 + \alpha^2 \sin^2(x)}}. \quad (C-5)$$

C.2 Stream Function Solution

For the stream function, Equations 4-39 to 4-42 give

$$m(r_m^\varphi + r_{-m}^\varphi) + mh(q_m^\varphi + q_{-m}^\varphi) = 0, \quad (C-6)$$

$$2h\delta_{m,0}B - m(r_m^\varphi - r_{-m}^\varphi) + (q_m^\varphi + q_{-m}^\varphi) - mh(q_m^\varphi - q_{-m}^\varphi)$$

$$= \frac{Kh^2}{4\pi} \delta_{m,0} + m(\mathbf{g}_m^\varphi - \mathbf{g}_{-m}^\varphi) - \frac{1}{2\pi} \delta_{m,0}, \quad (\text{C-7})$$

$$\begin{aligned} & \frac{\alpha^2}{4} (2\delta_{m,0} + \delta_{m,2} + \delta_{m,-2}) B + (r_m^\beta + r_{-m}^\beta) - \frac{\alpha}{2} (q_{m+1}^\beta + q_{m-1}^\beta + q_{-m+1}^\beta + q_{-m-1}^\beta) \\ & = -\frac{K\alpha^3}{96\pi} (3\delta_{m,1} + 3\delta_{m,-1} + \delta_{m,3} + \delta_{m,-3}), \end{aligned} \quad (\text{C-8})$$

and

$$\begin{aligned} & -\alpha(\delta_{m,1} + \delta_{m,-1}) B - m(r_m^\beta - r_{-m}^\beta) + (q_m^\beta + q_{-m}^\beta) + \frac{\alpha}{2} [(m+1)(q_{m+1}^\beta - q_{-m-1}^\beta) + (m-1)(q_{m-1}^\beta - q_{-m+1}^\beta)] \\ & = \frac{K\alpha^2}{16\pi} (2\delta_{m,0} + \delta_{m,2} + \delta_{m,-2}) + m(\mathbf{g}_m^\beta - \mathbf{g}_{-m}^\beta) - \frac{1}{2\pi} \delta_{m,0}. \end{aligned} \quad (\text{C-9})$$

From Equation 4-43 and Equation 4-34, we obtain

$$\exp(nh)r_n^\varphi - \sum_{m=-\infty}^{+\infty} r_m^\beta E_{m,n} = 0 \quad (\text{C-10})$$

and

$$\exp(nh)q_n^\varphi - \sum_{m=-\infty}^{+\infty} q_m^\beta E_{m,n} = 0. \quad (\text{C-11})$$

Those six equations (Equations C-6 to C-11) can be further simplified by eliminating $\{r_m^\varphi\}$ and $\{q_m^\varphi\}$ from equation set. We take index n as a positive integer only in the analysis.

Rewrite Equation C-11 as

$$q_n^\varphi = \frac{1}{n} \exp(-nh) \sum_{m=-\infty}^{+\infty} m I_{n-m}^- q_m^\beta, \quad (\text{C-12})$$

and take the negative indices,

$$q_{-n}^\varphi = -\frac{1}{n} \exp(nh) \sum_{m=-\infty}^{+\infty} m I_{n+m}^+ q_m^\beta. \quad (\text{C-13})$$

where the $(n-m)^{th}$ order modified Bessel function of first kind for argument $-n\alpha$, $I_{n-m}(-n\alpha)$, has been written as I_{n-m}^- for simplification purpose. Similarly, I_{n+m}^+ denotes the $(n+m)^{th}$ order modified Bessel function of first kind for argument $n\alpha$, $I_{n+m}(n\alpha)$. The same format is used from this point forward in this appendix. Equation C-10 is rewritten as

$$r_n^\varphi = \frac{1}{n} \exp(-nh) \sum_{m=-\infty}^{+\infty} m I_{n-m}^- r_m^\beta \quad (\text{C-14})$$

and

$$r_{-n}^\varphi = -\frac{1}{n} \exp(nh) \sum_{m=-\infty}^{+\infty} m I_{n+m}^+ r_m^\beta. \quad (\text{C-15})$$

Change the dummy variable in Equation C-6 and Equation C-7 from m to n , and use the expressions in Equations C-12 to C-15 to eliminate r_n^φ , r_{-n}^φ , q_n^φ and q_{-n}^φ , then we obtain

$$\sum_{m=-\infty}^{+\infty} m \left[\frac{I_{n-m}^-}{\exp(2nh)} - I_{n+m}^+ \right] r_m^\beta + \sum_{m=-\infty}^{+\infty} mh \left[\frac{I_{n-m}^-}{\exp(2nh)} - I_{n+m}^+ \right] q_m^\beta = 0 \quad (\text{C-16})$$

and

$$\begin{aligned} & \sum_{m=-\infty}^{+\infty} m \left[\frac{I_{n-m}^-}{\exp(2nh)} + I_{n+m}^+ \right] r_m^\beta - \sum_{m=-\infty}^{+\infty} m \left[\left(\frac{1}{n} - h \right) \frac{I_{n-m}^-}{\exp(2nh)} - \left(\frac{1}{n} + h \right) I_{n+m}^+ \right] q_m^\beta \\ & = - \frac{n \left[g_n^\varphi - g_{-n}^\varphi \right]}{\exp(nh)}. \end{aligned} \quad (\text{C-17})$$

Next, we multiply $I_{n-m}(-n\alpha)$ on both sides of Equation C-8, and take summation from $m = -\infty$ to $m = +\infty$. It yields

$$\begin{aligned} & \frac{\alpha^2}{4} \left[2I_n^- + I_{n+2}^- + I_{n-2}^- \right] B + \sum_{m=-\infty}^{+\infty} \left[I_{n-m}^- + I_{n+m}^- \right] r_m^\beta - \sum_{m=-\infty}^{+\infty} \frac{\alpha}{2} \left[I_{n+m-1}^- + I_{n+m+1}^- + I_{n-m-1}^- + I_{n-m+1}^- \right] q_m^\beta \\ & = - \frac{K\alpha^3}{96\pi} \left[I_{n-3}^- + I_{n+3}^- + 3I_{n-1}^- + 3I_{n+1}^- \right]. \end{aligned} \quad (\text{C-18})$$

A similar manipulation is applied to Equation C-9, we have

$$\begin{aligned} & -\alpha \left[I_{n-1}^- + I_{n+1}^- \right] B - \sum_{m=-\infty}^{+\infty} m \left(I_{n-m}^- + I_{n+m}^- \right) r_m^\beta + \sum_{m=-\infty}^{+\infty} \left[\left(I_{n-m}^- + I_{n+m}^- \right) + \frac{\alpha}{2} m \left(I_{n-m-1}^- + I_{n-m+1}^- + I_{n+m-1}^- + I_{n+m+1}^- \right) \right] q_m^\beta \\ & = \frac{K\alpha^2}{16\pi} \left[2I_n^- + I_{n-2}^- + I_{n+2}^- \right] + \sum_{m=-\infty}^{\infty} m \left[I_{n-m}^- + I_{n+m}^- \right] g_m^\beta - \frac{1}{2\pi} I_n^-. \end{aligned} \quad (\text{C-19})$$

Taking the zeroth order of Equations C-7, C-8, C-9 and C-11, we obtain

$$q_0^\varphi + Bh = \frac{Kh^2}{8\pi} - \frac{1}{4\pi}, \quad (\text{C-20})$$

$$r_0^\beta - \frac{\alpha}{2} (q_1^\beta + q_{-1}^\beta) + \frac{\alpha^2}{4} B = 0, \quad (\text{C-21})$$

$$q_0^\beta + \frac{\alpha}{2} (q_1^\beta - q_{-1}^\beta) = \frac{K\alpha^2}{16\pi} - \frac{1}{4\pi}, \quad (\text{C-22})$$

and

$$q_0^\varphi = q_0^\beta - \frac{\alpha}{2} (q_1^\beta - q_{-1}^\beta). \quad (\text{C-23})$$

Equations C-16 to C-19, supplemented by Equations C-20 to C-23, are sufficient to solve the Fourier coefficient sets $\{r_m^\beta\}$ and $\{q_m^\beta\}$. Once they are solved, q_n^φ and r_n^φ are determined from Equation C-12 and Equation C-14; q_{-n}^φ and r_{-n}^φ are solved from Equation C-6 and Equation C-7, as

$$q_{-n}^\varphi = (2nh-1)q_n^\varphi + 2nr_n^\varphi + n(g_n^\varphi - g_{-n}^\varphi), \quad (\text{C-24})$$

and

$$r_{-n}^\varphi = -h(q_n^\varphi + q_{-n}^\varphi) - r_n^\varphi. \quad (\text{C-25})$$

The zeroth term of $\{r_m^\varphi\}$ and $\{q_m^\varphi\}$ are obtained from Equation C-10 and Equation C-11 at $n = 0$, namely, Equation C-23 and

$$r_0^\varphi = r_0^\beta - \frac{\alpha}{2} (r_1^\beta - r_{-1}^\beta). \quad (\text{C-26})$$

In practical calculation, the infinite series in Equations C-16 to C-19 are truncated to only N terms. Together with Equations C-20 to C-23, there are a total of $4N + 4$ equations to solve for B , q_0^φ , $\{r_m^\beta\}$ and $\{q_m^\beta\}$, $m \in [-N, N]$. Subsequently, $\{r_m^\varphi\}$ and $\{q_m^\varphi\}$ are solved from Equations C-12, C-14, and C-23 to C-26. Finally, $\{r_m^\beta\}$, $\{r_m^\varphi\}$, $\{q_m^\varphi\}$ and $\{q_m^\beta\}$ are used to construct $R(\zeta)$ and $Q(\zeta)$ in Equation 4-37 and Equation 4-38, and they are used to solve for $\psi(x, y)$ in Equation 4-29.

LIST OF REFERENCES

1. R. P. Feynman, *Microelectromechanical Systems, Journal of*, 1992, **1**, 60-66.
2. M. Gad-el-Hak, *The MEMS Handbook*, CRC Press, 2001.
3. P. S. Dittrich, K. Tachikawa and A. Manz, Editon edn., 2006, vol. 78, pp. 3887-3908.
4. S. A. Vittorio, *MicroElectroMechanical Systems (MEMS)*, <http://www.csa.com/discoveryguides/mems/overview.php>.
5. M. J. Madou, *Fundamentals of microfabrication: the science of miniaturization*, 2nd ed. edn., CRC Press LLC, Boca Raton, 2002.
6. W. Trimmer, *A Tutorial on Micromechanics and MEMS*, <http://home.earthlink.net/~trimmerw/mems/tutorials.html>, Accessed 12/12, 2006.
7. R. Chan, *MEMS market to double in five years, Databeans says*, http://www.digitimes.com/bits_chips/a20061102PR204.html, Accessed 12/12, 2006.
8. A. McWilliams, *Microelectromechanical Systems (MEMS) Technology: Current And Future Markets*, <http://www.electronics.ca/reports/mems/technology.html>.
9. M. Born and E. Wolf, *Principles of optics : electromagnetic theory of propagation, interference and diffraction of light* 7th edn., Cambridge University Press, New York, 1999.
10. D. A. Agard, Y. Hiraoka, P. Shaw and J. W. Sedat, *Method Cell Biol*, 1989, **30**, 353-377.
11. D. A. Agard and J. W. Sedat, *Nature*, 1983, **302**, 676-681.
12. H. A. Stone and S. Kim, *Aiche Journal*, 2001, **47**, 1250-1254.
13. H. A. Stone, A. D. Stroock and A. Ajdari, *Annu Rev Fluid Mech*, 2004, **36**, 381-411.
14. R. F. Probstein, *Physicochemical hydrodynamics : an introduction*, 2nd edn., Wiley-Interscience, Hoboken, N.J., 2003.
15. E. W. Weisstein, *Maxwell Distribution*, <http://mathworld.wolfram.com/MaxwellDistribution.html>
16. D. A. Skoog, D. M. West and F. J. Holler, *Fundamentals of analytical chemistry*, 5th ed edn., Saunders College Pub, New York, 1988.
17. C. H. Amon, A. M. Guzman and B. Morel, *Phys Fluids*, 1996, **8**, 1192-1206.
18. I. Glasgow and N. Aubry, *Lab on a Chip*, 2003, **3**, 114-120.

19. A. D. Stroock, S. K. W. Dertinger, A. Ajdari, I. Mezic, H. A. Stone and G. M. Whitesides, *Science*, 2002, **295**, 647-651.
20. T. J. Johnson, D. Ross and L. E. Locascio, *Anal Chem*, 2002, **74**, 45-51.
21. M. Grumann, A. Geipel, L. Riegger, R. Zengerle and J. Ducree, *Lab on a Chip*, 2005, **5**, 560-565.
22. C. H. Lin, L. M. Fu and Y. S. Chien, *Anal Chem*, 2004, **76**, 5265-5272.
23. G. G. Yaralioglu, I. O. Wygant, T. C. Marentis and B. T. Khuri-Yakub, *Anal Chem*, 2004, **76**, 3694-3698.
24. J. B. Knight, A. Vishwanath, J. P. Brody and R. H. Austin, *Physics Review Letter*, 1998, **30**, 3863- 3866.
25. T. Rohr, C. Yu, M. H. Davey, F. Svec and J. M. J. Frechet, *Electrophoresis*, 2001, **22**, 3959-3967.
26. T. Burghlea, E. Segre, I. Bar-Joseph, A. Groisman and V. Steinberg, *Physical Review E*, 2004, **69**, -.
27. R. H. Liu, M. A. Stremler, K. V. Sharp, M. G. Olsen, J. G. Santiago, R. J. Adrian, H. Aref and D. J. Beebe, *Journal of Microelectromechanical Systems*, 2000, **9**, 190-197.
28. F. Schonfeld, V. Hessel and C. Hofmann, *Lab on a Chip*, 2004, **4**, 65-69.
29. Y. C. Chung, Y. L. Hsu, C. P. Jen, M. C. Lu and Y. C. Lin, *Lab on a Chip*, 2004, **4**, 70-77.
30. A. O. El Moctar, N. Aubry and J. Batton, *Lab on a Chip*, 2003, **3**, 273-280.
31. H. H. Bau, J. H. Zhong and M. Q. Yi, *Sensors and Actuators B-Chemical*, 2001, **79**, 207-215.
32. H. Suzuki, C. M. Ho and N. Kasagi, *Journal of Microelectromechanical Systems*, 2004, **13**, 779-790.
33. A. P. Sudarsan and V. M. Ugaz, *Lab on a Chip*, 2006, **6**, 74-82.
34. O. Kuksenok, J. M. Yeomans and A. C. Balazs, *Physical Review E*, 2002, **65**, -.
35. E. Biddiss, D. Erickson and D. Li, *Anal Chem*, 2004, **76**, 3208-3213.
36. L. F. Greer and A. A. Szalay, *Luminescence*, 2002, **17**, 43-74.
37. T. J. Johnson and L. E. Locascio, *Lab Chip*, 2002, **2**, 135-140.
38. R. J. Adrian, *Experiments in Fluids*, 2005, **39**, 159-169.

39. D. Sinton, *Microfluidics and Nanofluidics*, 2004, **1**, 2-21.
40. Y. N. Xia and G. M. Whitesides, *Annual Review of Materials Science*, 1998, **28**, 153-184.
41. D. C. Duffy, J. C. McDonald, O. J. A. Schueller and G. M. Whitesides, *Anal Chem*, 1998, **70**, 4974-4984.
42. C. E. Walker, Z. Xia, Z. S. Foster, B. J. Lutz and Z. H. Fan, *Electroanalysis*, 2008, **20**, 663-670.
43. *TOPAS COC - A clearly extraordinary polymer*, http://www.topas.com/products-topas_coc.
44. J. G. Santiago, S. T. Wereley, C. D. Meinhart, D. J. Beebe and R. J. Adrian, *Experiments in Fluids*, 1998, **25**, 316-319.
45. S. Devasenathipathy, J. G. Santiago, S. T. Wereley, C. D. Meinhart and K. Takehara, *Experiments in Fluids*, 2003, **34**, 504-514.
46. I. Glasgow, S. Lieber and N. Aubry, *Anal Chem*, 2004, **76**, 4825-4832.
47. C. H. Chen, H. Lin, S. K. Lele and J. G. Santiago, *J Fluid Mech*, 2005, **524**, 263-303.
48. B. He, B. J. Burke, X. Zhang, R. Zhang and F. E. Regnier, *Anal Chem*, 2001, **73**, 1942-1947.
49. S. K. Yoon, M. Mitchell, E. R. Choban and P. J. Kenis, *Lab Chip*, 2005, **5**, 1259-1263.
50. R. F. Ismagilov, A. D. Stroock, P. J. A. Kenis, G. Whitesides and H. A. Stone, *Appl Phys Lett*, 2000, **76**, 2376-2378.
51. J. I. Molho, A. E. Herr, B. P. Mosier, J. G. Santiago, T. W. Kenny, R. A. Brennen, G. B. Gordon and B. Mohammadi, *Anal Chem*, 2001, **73**, 1350-1360.
52. Y. Wang, Q. Lin and T. Mukherjee, *Lab Chip*, 2004, **4**, 453-463.
53. S. V. Ermakov, S. C. Jacobson and J. M. Ramsey, *Anal Chem*, 1998, **70**, 4494-4504.
54. L. L. Shultz-Lockyear, C. L. Colyer, Z. H. Fan, K. I. Roy and D. J. Harrison, *Electrophoresis*, 1999, **20**, 529-538.
55. M. S. Munson and P. Yager, *Anal Chim Acta*, 2004, **507**, 63-71.
56. D. S. Kim, S. H. Lee, T. H. Kwon and C. H. Ahn, *Lab Chip*, 2005, **5**, 739-747.
57. C. Neils, Z. Tyree, B. Finlayson and A. Folch, *Lab on a Chip*, 2004, **4**, 342-350.
58. D. Therriault, S. R. White and J. A. Lewis, *Nat Mater*, 2003, **2**, 265-271.

59. J. G. McNally, T. Karpova, J. Cooper and J. A. Conchello, *Methods*, 1999, **19**, 373-385.
60. J. B. Sibarita, *Adv Biochem Eng Biot*, 2005, **95**, 201-243.
61. S. F. Gibson and F. Lanni, *Journal of Optical Society of America*, 1991, **8**, 1601-1613.
62. A. V. Oppenheim and R. W. Schaffer, *Digital signal processing*, Prentice-Hall, Englewood Cliffs, N.J., 1975.
63. R. S. Figliola and D. E. Beasley, *Theory and Design for Mechanical Measurements*, 3rd edn., John Wiley & Sons, New York, 2000.
64. J. D. Ingle and S. R. Crouch, *Spectrochemical analysis*, Prentice Hall, Englewood Cliffs, N.J., 1988.
65. C. R. Chatwin and R. K. Wang, *Frequency Domain Filtering Strategies for Hybrid Optical Information Processing*, John Wiley & Sons, New York, 1996.
66. P. A. Jansson, R. H. Hunt and E. K. Plyler, *J Opt Soc Am*, 1970, **60**, 596-&.
67. R. Gold, *An iterative unfolding method for matrices ANL6984*, Argonne National Laboratory, Argonne, Ill, 1964.
68. W. H. Richardson, *J Opt Soc Am*, 1972, **62**, 55-59.
69. L. B. Lucy, *Astron J*, 1974, **79**, 745-754.
70. T. J. Holmes, *Journal of the Optical Society of America A*, 1992, **9**, 1052-1061.
71. D. J. Harrison, A. Manz, Z. H. Fan, H. Ludi and H. M. Widmer, *Anal Chem*, 1992, **64**, 1926-1932.
72. F. M. White, *Viscous Fluid Flow*, 2nd edn., McGraw-Hill, 1991.
73. N. A. Patankar and H. H. Hu, *Anal Chem*, 1998, **70**, 1870-1881.
74. F. Bianchi, A. Ferrigno and H. H. Girault, *Anal Chem*, 2000, **72**, 1987-1993.
75. S. Bhattacharyya, Z. Zheng and A. T. Conlisk, *J Fluid Mech*, 2005, **540**, 247-267.
76. X. C. Xuan and D. Q. Li, *Journal of Colloid and Interface Science*, 2005, **289**, 291-303.
77. A. Ajdari, *Physical Review Letters*, 1995, **75**, 755-758.
78. S. Ghosal, *J Fluid Mech*, 2002, **459**, 103-128.
79. R. Qiao and N. R. Aluru, *J Micromech Microeng*, 2002, **12**, 625-635.

80. E. B. Cummings, S. K. Griffiths, R. H. Nilson and P. H. Paul, *Anal Chem*, 2000, **72**, 2526-2532.
81. S. K. Griffiths and R. H. Nilson, *Anal Chem*, 2000, **72**, 4767-4777.
82. H. SalimiMoosavi, T. Tang and D. J. Harrison, *Journal of the American Chemical Society*, 1997, **119**, 8716-8717.
83. S. C. Jacobson, R. Hergenroder, L. B. Koutny, R. J. Warmack and J. M. Ramsey, *Anal Chem*, 1994, **66**, 1107-1113.
84. J. C. Burns and T. Parkes, *J Fluid Mech*, 1967, **29**, 731-743.
85. J. C. F. Chow and K. Soda, *Phys Fluids*, 1972, **15**, 1700-&.
86. C. Y. Wang, *Phys Fluids*, 1978, **21**, 697-698.
87. C. Y. Wang, *Phys Fluids*, 2003, **15**, 1114-1121.
88. I. J. Sobey, *J Fluid Mech*, 1980, **96**, 1-26.
89. K. D. Stephanoff, I. J. Sobey and B. J. Bellhouse, *J Fluid Mech*, 1980, **96**, 27-&.
90. S. Tsangaris and E. Leiter, *Journal of Engineering Mathematics*, 1984, **18**, 89-103.
91. C. Pozrikidis, *J Fluid Mech*, 1987, **180**, 495-514.
92. C. Pozrikidis, *J Fluid Mech*, 1988, **188**, 275-300.
93. H. Luo and C. Pozrikidis, *J Fluid Mech*, 2006, **556**, 167-188.
94. M. Hemmat and A. Borhan, *Phys Fluids*, 1995, **7**, 2111-2121.
95. G. Leneweit and D. Auerbach, *J Fluid Mech*, 1999, **387**, 129-150.
96. M. Scholle, *Arch Appl Mech*, 2004, **73**, 823-840.
97. A. E. Malevich, V. V. Mityushev and P. M. Adler, *Acta Mech*, 2006, **182**, 151-182.
98. H. H. Wei, S. L. Waters, S. Q. Liu and J. B. Grotberg, *J Fluid Mech*, 2003, **492**, 23-45.
99. H. Zhou, R. J. Martinuzzi, R. E. Khayat, A. G. Straatman and E. Abu-Ramadan, *Phys Fluids*, 2003, **15**, 3114-3133.
100. J. G. Santiago, *Anal Chem*, 2001, **73**, 2353-2365.
101. E. Lauga, A. D. Stroock and H. A. Stone, *Phys Fluids*, 2004, **16**, 3051-3062.

102. A. D. Polianin, *Handbook of linear partial differential equations for engineers and scientists*, Chapman & Hall/CRC, Boca Raton, 2002.
103. B. P. Palka, *An introduction to complex function theory*, Springer-Verlag, New York 1991.
104. H. K. Moffatt, *J Fluid Mech*, 1964, **18**, 1-18.
105. S. Y. Park, C. J. Russo, D. Branton and H. A. Stone, *Journal of Colloid and Interface Science*, 2006, **297**, 832-839.
106. M. Gu, *Advanced Optical Imaging Theory*, Springer, Berlin, 1999.

BIOGRAPHICAL SKETCH

Zheng Xia was born in 1978 in Luoyang, China. He spent his childhood with his family in this ancient city in China, until he moved to Beijing to embark on his college life in 1996.

After 4 years' study, Zheng Xia earned his B.E. degree in mechanical engineering from Tsinghua University, the most prestigious university in China. He then came to the United States to continue his graduate study at the University of Central Florida (UCF) in Orlando, Florida. Shortly after he received the M.Sc. degree in mechanical engineering from UCF in 2003, he attended graduate school at the University of Florida. While taking classes, he worked as a Research Assistant at the BioMEMS and Microfluidics lab of the UF for Dr. Z. Hugh Fan. He quite enjoyed the time spent in clean room, fabricating microfluidic devices on silicon, glass and plastic substrates. His research has been focused on micro scale fluid mechanics, microfluidic design and fabrication, and BioMEMS.

In 2004, his first year of PhD study at the University of Florida, he met Xinyi Wang, a PhD student of the College of Medicine who later became his wife in 2007. The couple welcomed the birth of their first son, Chase, in May 2008. Upon completion of his PhD program, Zheng Xia works shortly for Invitrogen Corp, a biotech company at Carlsbad, California, participating in a research project on micro-meso fluidic integration.